Advanced Diagnostic Techniques to Study the Electrochemical and Mechanical Properties of Polymer Electrolyte Fuel Cells

Thomas James Mason

A thesis for the degree of Doctor of Philosophy at University College London

Department of Chemical Engineering

University College London (UCL)

Torrington Place, London, WC1E 7JE, United Kingdom

I Thomas James Mason, confirm that the work presented in the thesis is my own. Where information has been derived from other sources, I confirm that this has been indicated in the thesis.

_____

Signature

_____

Date

I. Acknowledgements

Firstly I would like to thank Dr. Dan Brett. I started out on this journey with a supervisor and have ended up with a great friend. Your tireless work ethic, huge knowledge and most importantly your enthusiasm has driven me throughout. I hope that over the past few years I have begun to pay back the trust you've shown in me and I look forward to an amazing future working with you.

Thank you to Ahmad El-kharouf and Prof. Bruno Pollet for the collaboration work and encouragement. Thanks to Dr. Paul Shearing for his help and advice. I would also like to thank the entire Supergen fuel cells group, working with such an eminent group of academics has been an amazing opportunity and a challenge that I have enjoyed.

To Jay and Toby, for all the help and insight you have given me with my project I am truly grateful and for two greater friends I could not wish! I am grateful to Mike and Simon for their help throughout my research. To every member of the CO_2 Centre I would like to thank you all for your contributions. To Mae, Agata, Pattie and Anna thank you for the admin support and always smiling.

I would like to say a big thank you to my Dad, Anthony, George and Malcolm for their help with my work and everything else they do for me. Thank you to my Mum for encouraging me to achieve my best and always being there for me.

I would like to thank Katie for all her love and support. I could not do what I do without you.

II. Abstract

Polymer electrolyte fuel cells (PEFCs) are a key technology as the world strives for a low carbon future. The main obstacles facing mass-market uptake are the high cost and the longevity of the units; as such, research is needed to enhance performance and understand the degradation mechanisms. In this study, dynamic compression is applied using a cell compression unit (CCU) to study the effect on performance of a membrane electrode assembly (MEA) and its individual components with dimension change. Electrochemical impedance spectroscopy (EIS) is used to delineate the effect of compression on contact resistance, membrane resistance and mass transfer losses.

Derived parameters such as the 'displacement factor' are used to characterise a representative range of commercial gas diffusion layers (GDLs). Increasing compaction pressure leads to a non-linear decrease in resistance for all GDLs. Different GDLs have different intrinsic resistance; however, all GDLs of the same class share a common compaction profile (change in resistance with pressure). Cyclic compression of Toray GDL leads to progressive improvement in resistance and reduction in thickness that stabilises after ~10 cycles.

During initial hydration of Nafion membranes there is a direct relationship between membrane conductivity and dimensional change (swelling) of MEAs. Electrode flooding is found to result in membrane hydration and an increase in stress or strain, depending on the compression mode of the fuel cell. Results suggest that hydration cycles and flooding events can lead to cell degradation due to the stresses imposed.

With increasing compression, a significant reduction in net performance is observed, with the most significant differences occurring in the mass transport regions of the performance curves. As the compression increases, the high-frequency resistance reduces with the improvement in contact resistance between the GDL and bipolar plate material, concurrently the low frequency resistance increases with increasing compression.

III. Publications and Presentations

Primary Research Papers

- T.J. Mason, J. Millichamp, T.P. Neville, A. El-kharouf, B.G. Pollet, D.J.L. Brett**, Effect of clamping pressure on ohmic resistance and compression of gas diffusion layers for polymer electrolyte fuel cells**, Journal of Power Sources, 219 (2012) 52-59

- A. El-kharouf, T.J. Mason, D.J.L. Brett, B.G. Pollet, **Ex-situ Characterisation of Gas Diffusion Layers for Proton Exchange Membrane Fuel Cells**, Journal of Power Sources, 218 (2012) 393-404.

- T.J. Mason, J. Millichamp, T.P. Neville, P.R. Shearing, S. Simons, D.J.L. Brett, **A Study of the Effect of Water Management and Electrode Flooding on the Dimensional Change of Polymer Electrolyte Fuel Cells**, Journal of Power Sources (Submitted).

- T.J. Mason, J. Millichamp, D.J.L Brett, **A Study of the Effect of Compression on the Performance of Polymer Electrolyte Fuel Cells using Electrochemical Impedance Spectroscopy and Dimensional Change Analysis,** International Journal of Hydrogen Energy (Available Online).

Other Research Papers

- J. Millichamp, N.P. Brandon, R.J.C. Brown, R.C. Maher, G. Manos, T.J Mason, T.P. Neville, D.J.L. Brett**, A Study of Carbon Deposition on Solid Oxide Fuel Cell Anodes using Electrochemical Impedance Spectroscopy in Combination with a High Temperature Crystal Microbalance**, Journal of Power Sources (Available Online)

Presentations

- Zing Hydrogen and Fuel Cells Conference, **Effects of compression on ohmic resistance of gas diffusion layers in polymer electrolyte fuel cells**, Mexico, December 2011

IV. Contents

V. List of Figures

VI. List of Tables

VII. List of Equations

1. Literature Review

1.1. Introduction

Fuel cells are a key technology for the production of power in the transition from a carbon intensive economy to a sustainable low carbon future. Polymer electrolyte fuel cells (PEFCs) have a major role to play on a micro scale, particularly the automotive industry. The major advantages centre on the relatively high power density, zero carbon emissions (depending upon fuel source) and low temperature operation. The limitations of PEFCs are dominated by high catalyst costs, sensitivity to impurities within the fuel and perhaps more importantly significant gaps in the understanding of key internal processes such as water management (e.g. the hydration of the electrolyte).

Many *ex-situ* imaging techniques have been used to interrogate system components, which have then been related back to an operating system to make improvements in performance; but this is complex due to the dynamic nature of an operating fuel cell with many interacting mechanisms in concurrent operation. During standard operation of a fuel cell certain dimensional changes occur due, primarily, to the hydration and dehydration of the electrolyte. These changes are an issue due to the fixed nature of the typical fuel cell construction meaning that the net result of a membrane swelling is a crushing of the gas diffusion layer (GDL). This mechanical cycling is thought to be a mechanism of the degradation of the fuel cell components. By using a linear displacement sensor and a cell compression unit (CCU) combined with electrochemical impedance spectroscopy (EIS) techniques, an insight into the

significant (dimensional) changes that occur within the operating fuel cell will be demonstrated.

This thesis will begin with an introduction to the way PEFCs work, the important system components, the key issues that affect their performance and degradation and a look at the techniques that have been used to study the various mechanisms and material characteristics.

A novel experimental technique to utilise a number of different apparatus is outlined with a particular focus upon test rig development for making robust measurements including the development of a highly accurate and repeatable humidification system. In the work presented here, a high level of compression force control is achieved using a 'floating piston' fuel cell, combined with a linear displacement sensor that can monitor the change in thickness of the MEA with a resolution of 1 μm. The linear displacement sensor allows the extent of compression to be accurately measured. This new technique is utilised to investigate the effects of water flooding on operating PEFCs by looking at the resistance of the membrane and its thickness change in real time. In addition to polarisation analysis, EIS is used to deconvolute the losses associated with contact resistance and mass transfer limitation as a function of the compression of the cell.

The key goal for this study is to develop *in-situ* techniques to give added insight into the mechanisms that affect the performance and degradation of operating PEFCs. In particular the target is to analyse the effect of water management and the role of cell compression during common and extreme operating practices.

1.2. PE Fuel Cells

Polymer electrolyte (PE) fuel cells are an important part of fuel cell technologies due to their relatively low temperature operation, quick start-up time and portability compared to other types of fuel cell. A comparison of different types of fuel cells can be seen in Table 1 [1].

Table 1: Comparison of various types of fuel cells [1]

Fuel Cell	Temp. Range (°C)	Applications	Advantages	Disadvantages
Alkaline (Polymer), AFC	90 – 100	Space Military	High performance	Removal of CO_2 from air & fuel
Phosphoric Acid, PAFC	175 – 200	Electric Utility Transportation	High efficiency Impure fuel	Low power Large size
Molten Carbonate, MCFC	600 – 700	Electric Utility	High Efficiency Range of fuels	High temp enhances corrosion
Solid Oxide, SOFC	600 – 1000	Electric Utility Auxiliary Power	High efficiency Range of fuels	High temp enhances corrosion
Proton Exchange Membrane, PEMFC	60 – 100	Electric Utility Portable Power Transportation	Low temperature Quick start-up	Expensive catalyst Sensitive to impurities

A PE fuel cell is made up of several components and each are important areas of research. The membrane electrode assembly (MEA) is the main functional element of PE fuel cells and includes the proton exchange membrane, the anode and cathode catalytic layers, with each of the catalyst layers in contact with GDL. The main

functional components of a PE fuel cell can be seen in Figure 1 (a) with a picture of an in-house produced MEA in Figure 1 (b).

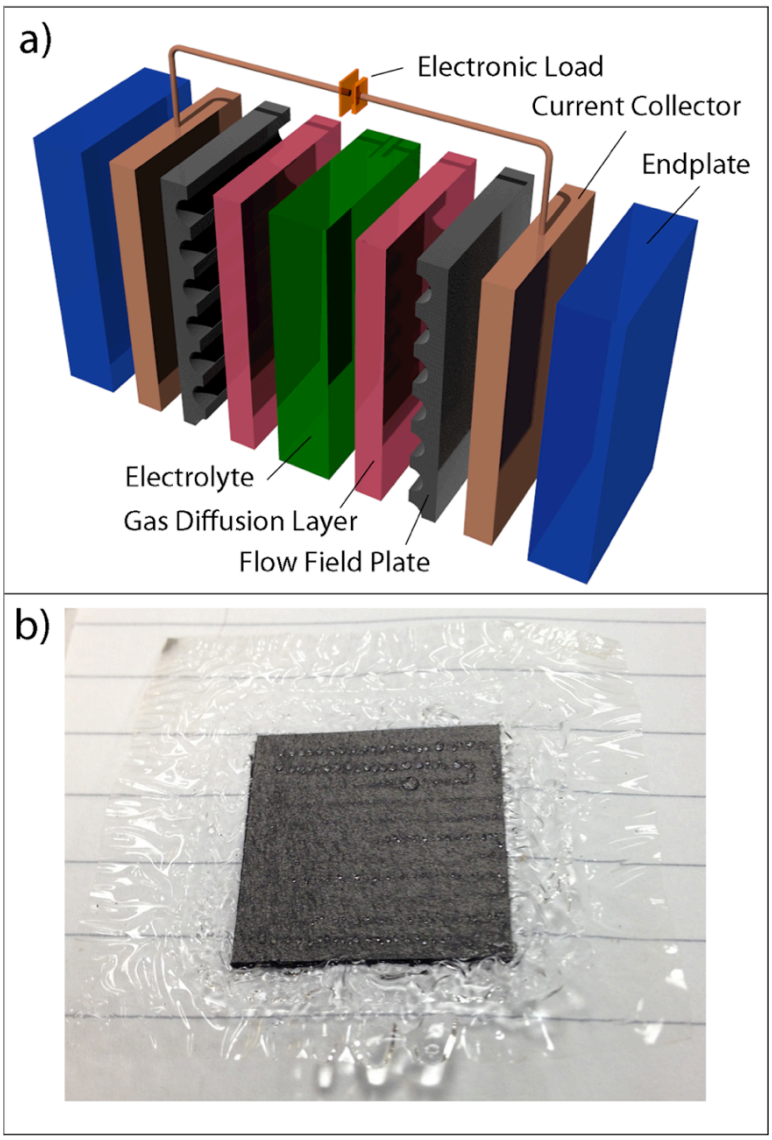

Figure 1 a): Diagram of the main elements of a PEFC. b): Picture of an in-house produced MEA after removal from the cell enclosure showing the water collection following the flow field pattern.

The MEAs are encased within seals, flow channels, current collectors, endplates and other balance-of-stack (BoS) hardware. In addition, balance-of-plant (BoP) equipment

consists of components such as flow controllers, humidifiers, valves, electronic loads and system controls that are essential in enabling the cell to function correctly. Each of the BoS components / BoP components are areas of important research aiming to reduce costs and improve performance and efficiency, Table 2 describes the key functions of the BoS / BoP.

Table 2: Key functions of the fuel cell BoS / BoP components

Component	Function
Seals	Provide adequate isolation of each component in the system while being able to cope with the fuel cell environment
Flow channels	Provide appropriate distribution of reactants and removal of products
Current collectors	Enable the currents generated by the cells to be connected to the load system
Endplates	Provide mechanical compression and strength to the system
Flow controllers	Provide dynamic reactant control to adapt to the specific requirements of the cell loading
Humidifiers	Provide variable levels of humidification to ensure maximum operating efficiency
Isolation valves	Safety feature to isolate the system and shut down gas feeds (particularly hydrogen)
Electronic load and control system	Provide loading to the fuel cell with required feedback to enable the system to react to change required to keep the cells operating at maximum efficiency
Hydrogen storage	Store hydrogen safely at a realistic quantity to enable the cell to function in the real world

1.3. MEAs

Proton exchange membrane (PEM) fuel cells achieve conversion of hydrogen and oxygen by the hydrogen oxidation reaction (HOR) and oxygen reduction reaction (ORR). The by-products of the reactions are heat, electrical power and water. The reactions are summarised thus:

Equation 1: HOR $$H_2 \rightarrow 2H^+ + 2e^-$$

Equation 2: ORR $$^1/_2\, O_2 + 2H^+ + 2e^- \rightarrow H_2O$$

Equation 3: Overall reaction $$H_2 + {}^1/_2\, O_2 \rightarrow H_2O$$

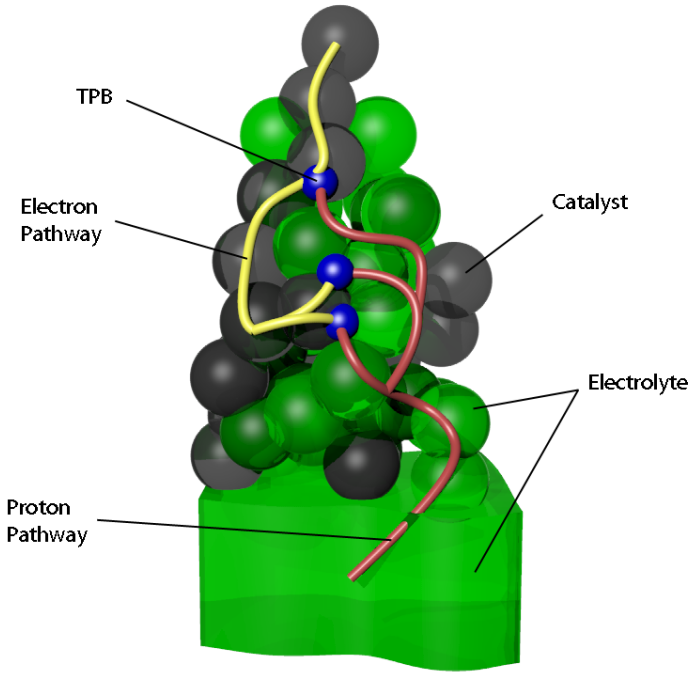

Figure 2: Illustration showing the generic description of a three-phase boundary (TPB) in the anode of a fuel cell. In PEFCs the electrolyte tends to cover the catalyst agglomerates and reactant diffuses through the electrolyte to the catalyst surface.

The HOR and ORR occur at the catalyst layers of the anode and cathode respectively at a reaction site known as the three-phase boundary (TPB, see Figure 2). The TPB consists of the points in the electrodes that are connected to both ionic and electron pathways, a catalyst reaction site and where the reactant gasses can access. The catalyst material is potentially the most significant individual part of the fuel cell and is a significant area of research focussing on the creation of a novel high performance catalyst and the reduction of the loading precious metals (e.g. Pt.).

The catalyst layer in the electrode assembly is typically made up of a carbon support that has a dispersion of catalyst on its surface; this electrode material is typically made up as a catalyst ink (including some solution of electrolyte material), which is then deposited upon the electrolyte or GDL surface. The GDL-electrode-electrolyte assembly is then hot pressed together to enable the interfaces to be correctly formed and the MEA to become a single structure. The hot-pressing procedure involves the MEA being compressed between two heated plates at specific temperature and pressure for a defined length of time, this process allows the electrolyte material to 'flow' in the system and create the required bonds and connections.

The electrolyte membrane is the other critical component in the MEA. The membrane's primary purpose is to conduct protons from the anode to the cathode to complete the electrochemical circuit while having other key features such as being highly electrically insulating, mechanically strong and corrosion resistant. By far the most common material used as a membrane is DuPont's Nafion material. Nafion is classed as a sulphonated fluropolymer and is based upon the polytetrafluroethylene

(PTFE) backbone with a specific quantity of sulphonate groups acting as the functional element. Nafion has many properties that make it a very good material to make a membrane from. Some of these advantages come from the basic PTFE backbone of the material but other characteristics come from the side groups specific to the Nafion ionomer. The material properties are summarised in Table 3.

Table 3: Summary of Nafion Properties

Characteristic	Reference	Property
PTFE Backbone	[2, 3]	• PTFE is hydrophobic by nature while the sulphonate groups are hydrophilic • PTFE is resistant to chemical attack which is advantageous due to the acidic nature of the catalyst layers • PTFE has a high mechanical strength
Nafion Specific Properties	[2]	• Under standard operating conditions of a proton exchange membrane cell only metallic alkali metals attack Nafion • In terms of polymers, Nafion has a high working temperature and can cope with typical PEM temperatures (circa. 90 °C) • Nafion is highly ion-conductive • Due to the hydrophilic nature of the sulphonate groups, Nafion is highly efficient at absorbing water and permeable to water

While Nafion is the most appropriate electrolyte membrane material currently commercially available, there are some significant issues in the way the material performs. The most critical function of an electrolyte is its ionic conductivity and with Nafion this is highly dependent upon the water content. As such, a complex dynamic system exists under operating conditions, which is discussed further in section 1.5.

1.4. Gas diffusion layer and its characterisation

The GDL plays a crucial role in the operation of PEFCs. The GDL enables gas to diffuse to and from the electrode surfaces, removes water from the electrode, provides electrical conduction between the current collector (bipolar plate) and the catalyst layer and provides a thermally conductive path to dissipate the heat produced at the catalyst. As such, the ideal properties for a GDL are for it to: be highly electrically and thermally conductive (note that some thermal resistance can be desirable for water management so that product water can move away from the electrode as a vapour); have a large porosity and low tortuosity to allow effective diffusion (yet maintain requisite mechanical properties); facilitate water removal from the electrodes by having the appropriate hydrophobic/hydrophilic properties. These properties are desirable for all the key layers in the MEA structure namely GDLs, micro-porous layers (MPLs) and catalyst layers (CLs).

The two main varieties of GDL are the 'paper' and 'cloth' types, each made of carbon fibres. Typically for GDLs, the carbon substrates are water proofed (with PTFE) to prevent the blockage of pores with water that can disrupt reactants diffusion to the catalyst layers during fuel cell operation [4]. A MPL made of carbon and a hydrophobic agent, is often added on the GDL surface between the catalyst layer and the GDL to enhance the water removal from the catalyst layer, minimizing the electrical contact resistance with the adjacent catalyst layer, and preventing the catalyst ink from leaking into the GDL, thereby increasing the catalyst utilization and reducing the tendency of electrode flooding [5]. Furthermore, it has been reported that the presence of MPL in PEM fuel cell electrodes improves their performances and enhances their durability [6]. A description of GDL fabrication, materials,

characteristics measurement methods and degradation processes has been recently reviewed by El-kharouf and Pollet [7] and GDL characteristics and fuel cell performance has been reviewed by Cindrella *et al*. [8].

A significant performance limitation for fuel cells is the ohmic losses associated with contact and bulk resistances. Of these ohmic losses, the contact resistance between the GDL and the land of the flow channels of the bipolar plate plays a significant part. Contact resistances are known to be greatly affected by the compaction force applied and the way the fuel cell is assembled. Studies have shown the importance of cell compression on the overall performance of an operating fuel cell [9, 10].

Despite the importance of compression regimes and the link between compression and electrochemical performance, relatively few studies have been reported in the literature and further research is required. Compression methods incorporating springs, integrated bladders and hydraulic or pneumatic presses have been described [11]. However, by far the most common method is the use of tie-rods of various numbers and positions, with controlled torque applied to the nuts at the end plates.

The pressure imposed to or exerted within a fuel cell can be measured in a number of ways. These include incorporating a pressure sensitive film into the cell (e.g. Pressurex) [12], or using a load cell located between the nut and the cell endplate [13]. Pressure sensitive film requires the cell to be dismantled and therefore does not permit information about how the pressure changes with time. Load cells provide ‘real time’ data but do not take into account the losses within the system (frictional losses between mating surfaces), so the pressure exerted within the stack, experienced

by the components, must be inferred. Of particular importance is an ordered assembly of the tie-rod type design as an even loading of the MEA is essential to prevent damage due to localised high compression during construction.

Piezoresistive thin film sensor arrays have been demonstrated and allow 'real time' distributed pressure monitoring within operational fuel cells [14]; the technique provides valuable information for optimizing compression, results obtained show that the type and design of seals / gaskets is vital in this process.

Other ways in which the ohmic losses can be affected include reactant gas pressure variations [15], flow-field geometry (ratio between land and channel) and dimensional changes in components such as the membrane material, which can change in thickness by a relatively large amount during hydration cycling and start-up / shutdown of the fuel cell [16].

The effect of compression force on fuel cell performance has been studied by Lee *et al.*, who showed that depending on the type of GDL material used, an optimum compression force exists [9]. However, this study used the bolt torque method of controlling force and as such is not particularly accurate or repeatable in terms of being transferable between cell designs. Other *in-situ* studies have used hydraulic presses [11] and screw arrangements [17] to try to improve the reproducibility of such testing. More fundamental studies such as those by Radhakrishnan *et al*. and Su *et al.* have examined the effects of compression on the GDL media *ex-situ,* and have attempted to model the compressive effects [18, 19]. Brett *et al.* employed a segmented current collector, made using printed circuit board technology, to capture

the spatial variation of contact resistance across a cell and found that the way a fuel cell is put into compression using tie bolts has a significant effect on the resistance distribution [20]. The findings of these studies show that as the compressive force increases there is a substantial decrease in contact resistance coupled with a decrease in the porosity of the GDL material. While the contact resistance reduction is desired, the decrease in porosity has the effect of limiting the pathways within the material, therefore reducing the effective diffusion coefficient and as such restricting the performance of the cell at high reactant utilizations (see Equation 14).

Table 4 summarises the range of materials and compression conditions previously reported in the literature. It can be seen that the nature of the GDL and the compaction range has a significant effect on the contact resistance measured. The bipolar plate (BPP) material is also known to affect the contact resistance [21].

Table 4: Comparison of compression ranges and resistances reported in the literature for different BPP and GDL materials

GDL Material	BPP Material	Compression Range (MPa)	Resistance (mΩ cm^2)	Ref.
TORAY H060	Plexiglas	0.48 → 2.41	N/A	[22]
Paper Type	Graphite	0.25 → 3.5	45 → 23	[13]
SGL-10	-	0.15 → 3	6 → 2	[23]
Toray H Series	-	0.45 → 3.6	160 → 0.06 *	[11]
ELAT	Stainless Steel	0.42 → 0.92	28 → 14	[15]
ELAT	Graphite	3	10	[24]
ELAT	Graphite	0.4	13	[24]
Carbel CL	Poco graphite	0.5 → 3	30 → 10	[25]

* = mΩ

1.5. Water management

Over the last few decades intensive research and development in the low temperature fuel cells area has focused on key issues such as catalyst development, low cost materials, performance and durability. A large section of research in the area of performance degradation has focused on water management, an area that has been extensively reviewed [26-28].

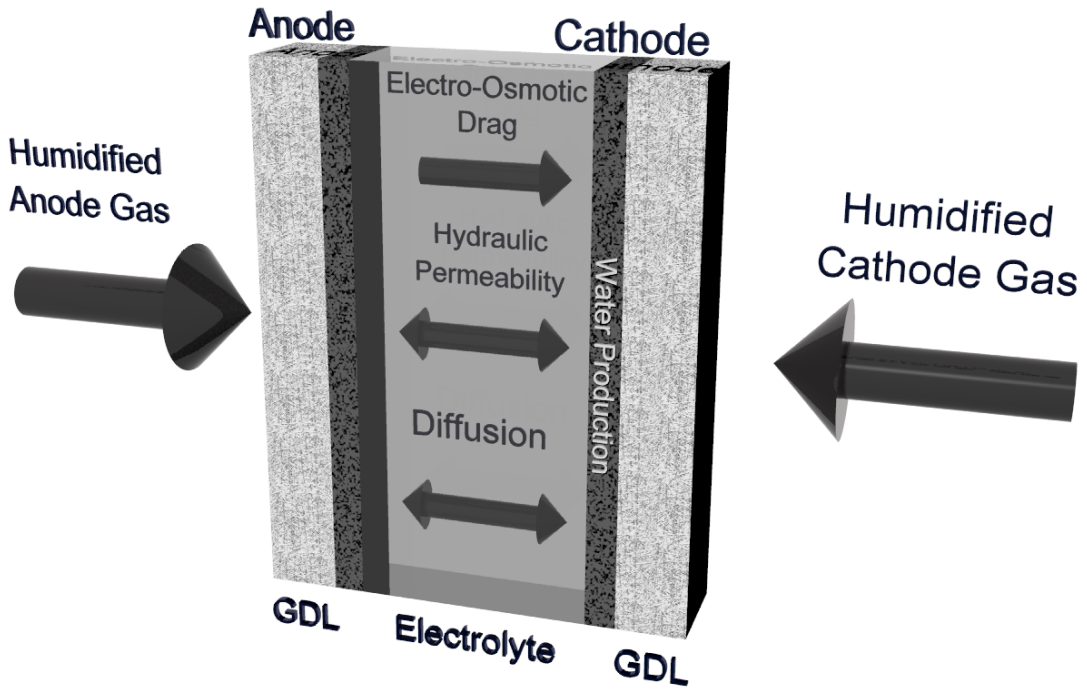

Figure 3: Depiction of the dynamic water balance of an operating PEMFC.

Water management inside a PEFC is a function of generation (reaction), various transport processes and the effect on the proton conductivity of the membrane (summarised in Figure 3). It has a significant impact on PEFC performance and is one of the major challenges facing the development of this technology [29]. Mechanisms of particular importance include electro-osmotic drag, which draws water from the

anode through the electrolyte to the cathode associated with the migration of protons [30]; back diffusion of water from the cathode to the anode due to hydraulic pressure difference; hydration of the membrane which effects the conductivity of the electrolyte [31] and the fact that water is produced at the cathode catalyst layer (CCL) by the oxygen reduction reaction (ORR). Accumulation of water limits the performance of the PEFC due to mass transport limitation of flooded electrodes [32]. Effective water management requires careful consideration of fuel cell component design, the materials used and the operating conditions imposed.

When water builds up at the cathode (CCL), the mechanisms for removing it include the hydrophobic nature of the elements of the GDL (PTFE content and distribution), the operating temperature of the fuel cell (removal as water vapour), and back-diffusion through the electrolyte. When the rate of water accumulation at the CCL exceeds the removal rate, the pores in the GDL, and ultimately the flow channel, get blocked (flooding, see Figure 4). When this occurs the catalyst is effectively starved of reactant and hence the performance of the cell decreases at a micro and macro scale.

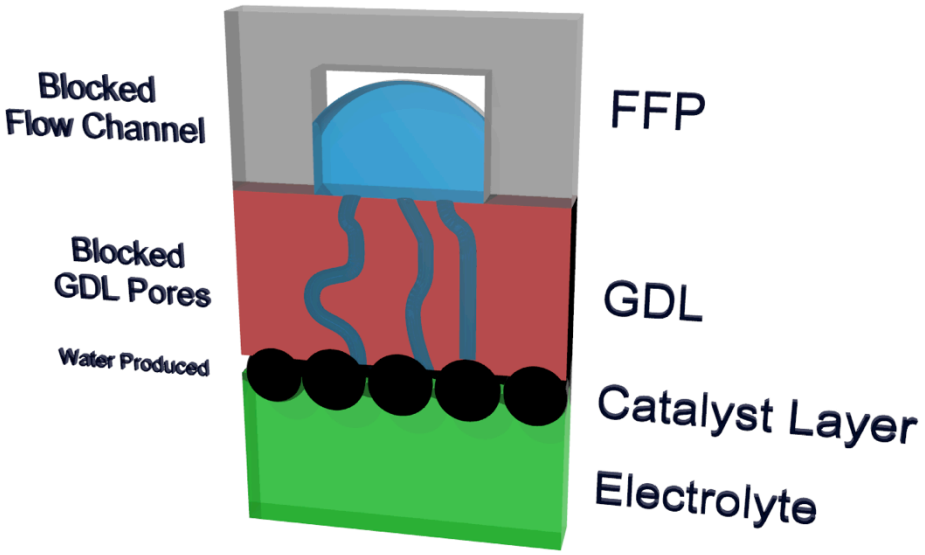

Figure 4: Representation of flooding occurring when the water produced at the cathode blocks the pores of the GDL and the flow channel above.

Extensive research has taken place into understanding water management and developing new materials and cell designs to mitigate flooding; this includes examining the effects of GDL material [33, 34], PTFE content [35, 36], micro-porous layers (MPL) [37, 38], porosity of the GDL / MPL structure [39, 40], flow field design [41, 42], CCL materials and microstructure [43, 44] and fuel cell operating conditions [45-47]. The GDL is a particularly important component for water management; an understanding of the various chemical and physical properties of which is particularly important for effective MEA design [48].

In order to study fuel cells and obtain a better understanding of their internal workings, a range of diagnostic techniques have been developed [20]; of these, several key techniques have been used to analyse *in-situ* effects of water management and flooding. An electrochemical impedance spectroscopy (EIS) technique was used

by Canut *et al*. to study membrane conductivity during drying and flooding [49]. Barbir *et al.* showed, again using EIS, a relationship between cell resistance and humidification level with pressure drop analysis used concurrently to show the onset of water flooding [50]. Membrane conductivity spatial mapping has been demonstrated by Brett *et al*. [51] and applied by Hakenjos *et al.* in conjunction with temperature distribution analysis to look at water flooding [52].

Experimental diagnostics of water management, and in particular water flooding, have been extensively researched with particular focus on imaging techniques such as optical visualisation [47, 53-55], X-ray imaging [56, 57], neutron imaging [58-60] and magnetic resonance imaging [61, 62].

The value for the thickness of the electrolyte membrane is difficult to quantify; however, some studies that have measured the difference in the membrane thickness between the 'as received' conditions and the fully hydrated thickness. A summary of selected published data on this can be seen in Table 5.

Table 5: Summary of electrolyte membrane thickness change data

Research	Nafion Membrane	'As received' thickness (µm)	Hydrated thickness (µm)	% Change
Gebel *et al*. [63]	117	175 ± 1	200 ± 1	14
Hinatsu *et al*. [64]	117	180 ± 4	210 ± 4	17
Slade *et al*. [16]	117	183 ± 3	208 ± 5	14
Satterfield *et al*. [17]	115	127 ± 4	158 ± 4	24
Slade *et al*. [65]	117	186 ± 4	223 ± 8	20

The method of producing the data in Table 5 is important. In these studies the thickness is measured *ex-situ*, which means that data can only be related to outside the fuel cell environment, and is not an accurate representation of how the Nafion changes in the fuel cell environment.

Due to the hydrophilic nature of the sulphonate groups the electrolyte membrane will absorb water when it comes into contact. A table of data from numerous studies of the thickness and conductivity of Nafion can be seen in Table 6, as measured *ex-situ* in a wide variety of environments. From Table 6 we can see that the value for conductivity is highly dependent upon the temperature, thickness and operating conditions. The range of conductivities from this table is between 0.050 – 0.231 S cm^{-1}, this range would appear to be accurate as when the conditions are similar the agreement is close. This can be seen by the studies of Sone *et al*. [66] and Edmonson *et al*. [67] where using similar conditions the conductivity was measured as 0.078 and 0.080 S cm^{-1} respectively. The range of conductivities is significant and has a relatively large impact on the performance of the fuel cells from a purely ohmic resistance point of view; however, some of the published environments are not realistic of an operational PEFC and as such are indicative only.

Table 6: Summary of Nafion conductivity and thickness data from various studies

Research	Nafion Type	Conditions	Temperature (°C)	Technique used	Thickness (μm)	Conductivity (S cm^{-1})
Rieke & Vanderborgh [68]	117	100% RH water vapour	25	EIS	175	**0.070**
Verbrugge & Hill [69]	117	Immersed in 1 M H_2SO_4	20	Current Pulse (DC)	231	**0.088**
Verbrugge *et al.* [70]	117	Immersed in 1 M H_2SO_4	80		231	**0.231**
Zawodzinski [71]	117	Immersed in Water	30	EIS	175	**0.100**
Zawodzinski [72]	117	Immersed in Water	90		175	**0.190**
Zawodzinski [73]	117	100% RH water vapour	30		175	**0.060**
Wilson *et al.* [74]	117	Immersed in 1 M H_2SO_4	25	Kelvin – Four point probe	200	**0.140**
Halim *et al.* [75]	117	Immersed in Water	25	EIS	200	**0.100**
	112	Immersed in Water	25		60	**0.100**
	117	Immersed in Water	20		175	**0.090**
Nouel & Fedkiw [76]	117	100% RH water vapour	25		210	**0.140**
	112	100% RH water vapour	65		52	**0.144**
Yoshida *et al.* [77]	117	Immersed in 1 M H_2SO_4	25		175	**0.076**
Anantaraman & Gardner [78]	117	100% RH water vapour	30		200	**0.068**
Sone *et al.* [66]	117	100% RH water vapour	20		200	**0.078**
Sumner *et al.* [79]	117	100% RH water vapour	20		175	**0.050**
Edmonson *et al.* [67]	117	100% RH water vapour	20		170	**0.080**
Wakizoe *et al.* [80]	115	*In-situ* humidified gases	95		125	**0.074**
Buchi *et al.* [81]	117	*In-situ* humidified gases	60	Current pulse (DC)	203	**0.105**
Alberti *et al.* [82]	117	100% RH water vapour	80	EIS	200	**0.097**
Yang *et al.* [83]	115	100% RH water vapour	80		210	**0.100**
Xie *et al.* [84]	117	Immersed in 2 M HCl	25	Current pulse (DC)	200	**0.066**

The diagnostic techniques applied to the study of water management and flooding have tended to concentrate on the effect of membrane conductivity and the mass transport limiting effect of water in the GDL and electrode. Extensive work has been dedicated to the understanding of Nafion in order to characterise the structure and distribution of water [85]; however, little has been done to examine the effect of dimensional change associated with changes in the hydration of the membrane and its impact on cell and stack performance.

1.6. Resistance, compression and performance

A key area of importance in determining overall performance of a fuel cell system is the balance-of-stack. The design of the stack must consider the method of putting the cells into compression, gas and liquid sealing, current collection and reactant delivery.

Figure 5 shows a schematic of a fuel cell (single plate and stack), it highlights the features typically encountered in a conventional design with non-porous planar flow plates and internal manifolds. The stack is composed of a number of flow-field plates (FFP) interspersed with cooling plates and held together with tie-rods, which connect at each end of the stack to end-plates. The number of flow-field plates per cooling plate varies depending on the design. The stack can be described by the number of flow-field plates used or by the number of 'repeat units' which is the smallest unit within a stack containing a membrane electrode assembly (MEA), flow-field plates and cooling component. Electrical connection to the stack can be made at each of the two end-plates or to bus-plates (or stack current collectors) situated between the end-plates and the first flow-plate at each end of the stack. For internally manifolded flow-

plates, the reactant and coolant fluid is introduced through the end-plates directly to the respective manifold. From the reactant manifolds, service to each MEA active area is provided by a flow network or single flow channel. Electrical current generated at the electrodes of the MEA is drawn away by the parts of the flow-field in contact with the electrode, these are commonly referred to as the 'lands'.

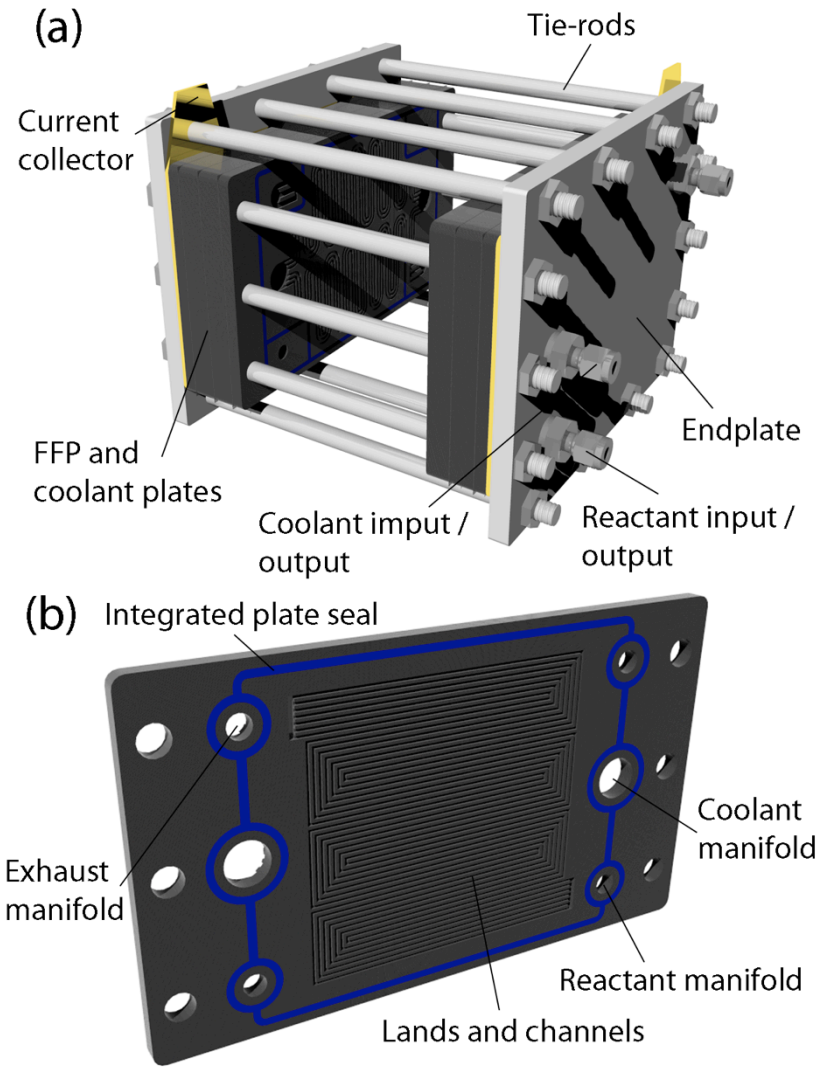

Figure 5 (a) Annotated schematic of a PEMFC stack exploded to show a coolant plate; (b) annotated FFP showing the various manifolds, integrated plate seal and active area lands and channels.

The role of the bipolar plate is many-fold, it must carry fuel and oxidant to the respective electrodes and disperse the fluid in an even and controlled manner; it must conduct electronic current from each electrode; it should provide mechanical support and strength to the MEA; it should remove excess product water from the reaction zone; it should act to control the temperature of the cell either by acting as a heat source (i.e. from embedded electrical heaters) or sink (i.e. by water cooling); it must act as a separator of reactant within a stack; The ideal properties of a FFP are that it should be an excellent electrical conductor in all planes and have a low contact resistance with the GDL; it should be a good thermal conductor with a coefficient of thermal expansion of the same order as its neighbouring components; it should be impermeable to reactant fluids; have high mechanical strength so as to be mechanically robust; be corrosion resistant under operation conditions; be as thin and light as possible be inexpensive and easy to manufacture [21].

1.6.1. Combination of GDL and FFP and the effect of compression

Most experimental studies focus on the performance and properties of the GDL / FFP in isolation, without considering the combined effect. For example, an optimal flow channel width may be determined which maximises the electrical conduction and reactant transport to the catalyst. However, if you change the GDL to one with a different hydrophobicity, conductivity, porosity etc. the optimal channel width will change also.

The properties of the GDL and FFP also have an effect on the macroscopic access of reactant to catalyst. Dohle *et al*. [86] analysed the interaction of the GDL and the

flow-field geometry by experimentally monitoring flow patterns and presenting a model to account for the findings. It was found that two types of flow are in operation, the extent of each determined by the permeability of the GDL. Two limiting cases are envisaged, one in which the permeability of the GDL is so low that transport is confined to the channel alone (primary flow only); this results in reasonable exposure to all corners of the plate but none to the interstices between the channels. The other is where the permeability is so high that the flow is exclusively through the GDL (secondary flow only); here the flow tends to take the most direct route between the inlet and outlet of the cell, leaving the other corners starved of reactant. In practice, the actual flow within the cell is a combination of the two and is determined by the permeability of the GDL and the length, width, shape, geometry and therefore backpressure of the channel and the rate and constitution of the flow. The experimental results showed that marked inhomogeneity can occur in the flow distribution if the permeability of the GDL and the backpressure in the channel are too high. It is therefore prudent to consider the flow geometry of the FFP combined with the properties and permeability of the GDL.

When a fuel cell is compressed, a significant change is observed in the structure of the GDL. As the compression increases, the GDL material beneath the land is crushed [19, 87], as illustrated in Figure 6. The crushing of the GDL at points of contact with the flow field plate effectively creates two systems: one below the lands and one below the channels. Below the lands the GDL fibres are crushed and the GDL is compressed, losing porosity and affecting the ability of reactant to access the catalyst under the land and the water produced to be removed. At the same time it reduces the contact resistance between the FFP and GDL by creating more contacts with the

surface as more fibres touch the interface. Under the open channel area the GDL remains largely uncompressed although towards the land interface a compression gradient exists which creates the 'tenting' observed. With the under channel GDL being uncompressed the reactant flow and water removal are largely unaffected creating a complex multi-region system that must be analysed in its constituent parts.

Since the GDL is composed of primarily laterally orientated fibres (depending upon material type), some of the compression exerted under the lands is transferred into the open channel area, leading to a certain amount of compression. However, excessive force can see the GDL protruding into the channel in a process known as 'tenting'. Under such conditions, shearing of the GDL fibres at the land/channel interface can lead to permanent damage and the tenting effect can cause an increased back pressure in the flow channel.

While the GDLs exhibit a structurally large change with compression (the focus of this work) the MPL and CL will also undergo changes due to compression variation, such as changes in their respective porosities and wettability [88].

There are therefore two competing processes, one relating to contact pressure that improves with increasing compaction pressure and one relating to mass transport under the channel layer that is expected to decrease performance with compaction pressure. Such a trade-off implies that there is an optimum compression to maximise fuel cell performance, it is expected that the trade-off will be complicated by the operating regime due to these two effects occurring at different points on the

performance curve. This indicates that a dynamic optimum compression is likely required.

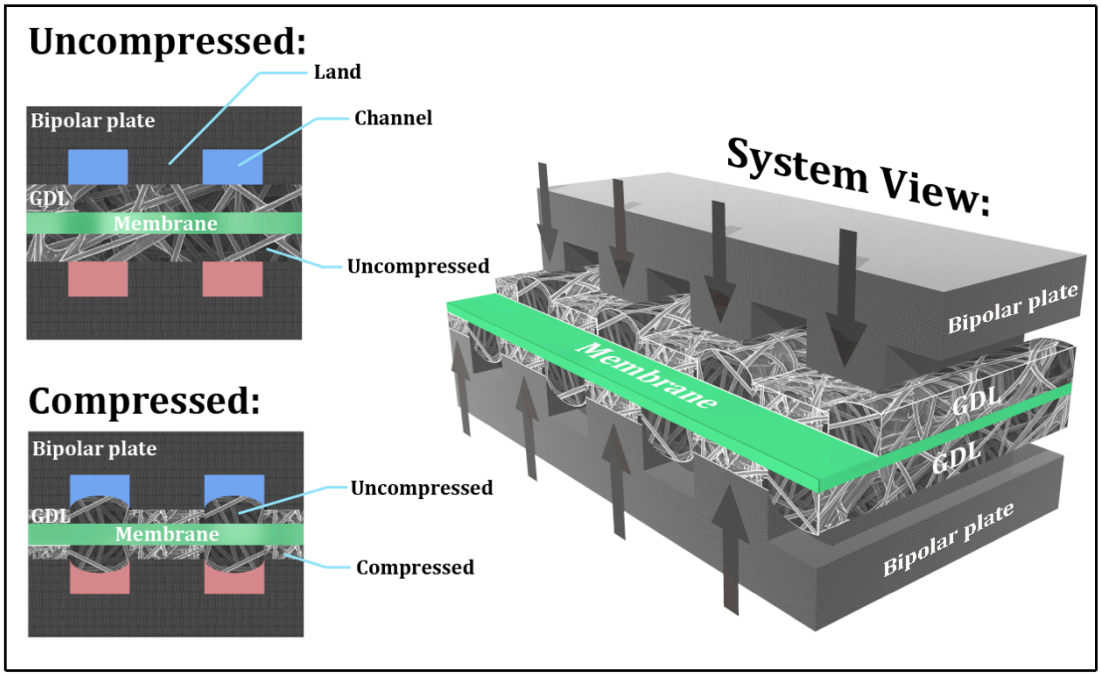

Figure 6: Image of the compression processes; as the fuel cell is compressed a loss in thickness occurs as the land compresses the GDL beneath it.

In order to study the internal workings of fuel cells a range of diagnostics have been developed [20]. A variety of *in-situ* diagnostic techniques are available which can probe a fuel cell without causing a perturbation of the system, of particular interest is EIS. EIS allows the electrochemical response of the system to be analysed and can give insight into individual processes that occur in the system.

Previous research based on the compression effect on performance has focussed on analysis of polarisation data and has been carried out using a combination of tie-rod and other mechanical compression systems [89]. These studies have shown that fuel cell performance has a strong dependence on compression, with generally a lower

performance observed at higher current densities and higher compressions. The trends observed are often dramatic and occur over a large range of compression exceeding the likely range of compression in commercial cells.

Fuel cell polarisation analysis reported by Ous and Arcoumanis showed that increasing compression significantly affected performance, with an improvement observed in the ohmic region and decrease in performance seen in the mass transport region [90]. Other works have shown similar trends [13, 19, 89, 91-93].

The level of robustness of compression also has to be addressed with some research focussing on compression in percentage terms or torques, which are hard to replicate and will be dependent upon specific cell designs [89, 91]. Also, the various losses in electrochemical performance are not adequately characterised, with most analysis based on polarisation curve data alone.

1.7. Electrochemical impedance spectroscopy (EIS)

Electrochemical impedance spectroscopy is an advanced diagnostic technique used in a variety of different fields to analyse various electrochemical processes in a system. EIS has been widely applied to fuel cell testing with a large volume of literature focused on its use in fuel cell research [94].

EIS in essence consists of applying a sinusoidal perturbation to the voltage or current of a system followed by measuring the effects on the current or voltage respectively. The measurements consist of both a phase shift (ϕ_{ps}) and amplitude (E and I) measurements, meaning each response can be treated as vector quantities (Ė and İ) with the following properties [95]:

Equation 4 $$\boldsymbol{e = E \times \sin(\omega t)}$$

And for the measured current response:

Equation 5 $$\boldsymbol{i = I \times \sin(\omega t + \phi_{ps})}$$

The ideal response from a pure resistor (R) and a pure capacitor (C) is shown in Figure 7 a) and b). For the pure resistor (Figure 7 (a)) no phase shift is present whereas a pure capacitor has a phase shift of -π/2 as shown in Figure 7 (b). In practice the systems studied with EIS (such as fuel cells) have components of both resistance and capacitance, Figure 7 (c) show the vector diagram for a series RC circuit. In this case complex notation is added to simplify the representation of the vectors into real (Z' or Z_{RE}) and imaginary (Z'' or Z_{IM}) components. Despite being treated as an imaginary component, Z'', is a measured property from the phase shift between the

current and voltage response and is only shown in this way for notation purposes. The general impedance equation is given by:

Equation 6 $$\boldsymbol{Z\,(\omega) = Z_{RE} - jZ_{IM}}$$

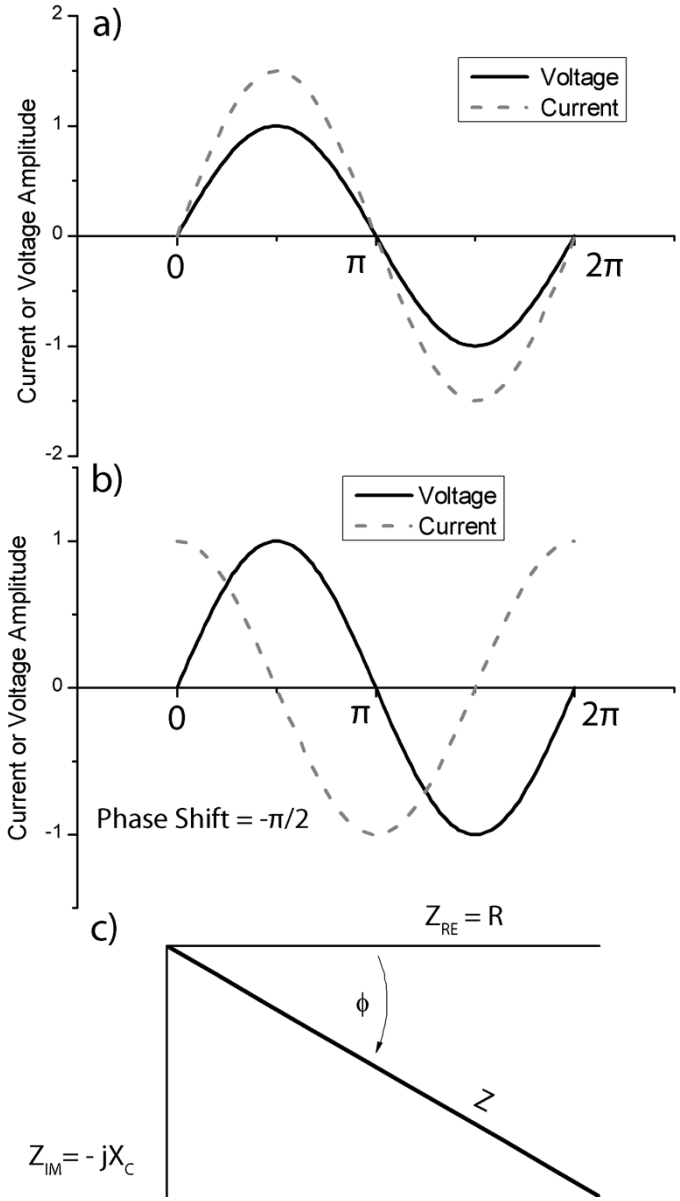

Figure 7: a) Depiction of the response to a sinusoidal voltage perturbation of the current of a pure resistor. b) Phase shift observed of a voltage perturbation on the current of a pure capacitor. c) Impedance vector diagram of resistor in series with a capacitor

Impedance data is typically displayed in a Nyquist plot (Figure 8) where the real (Z') and imaginary components (-Z'') are plotted on the x and y axis respectively. It is possible to take from a typical Nyquist plot either information about the whole system or individual components of that system. Figure 8 demonstrates the typical response for a fuel cell electrode (Randles cell) and where the individual components can be obtained, with the insert demonstrating the equivalent circuits for this response.

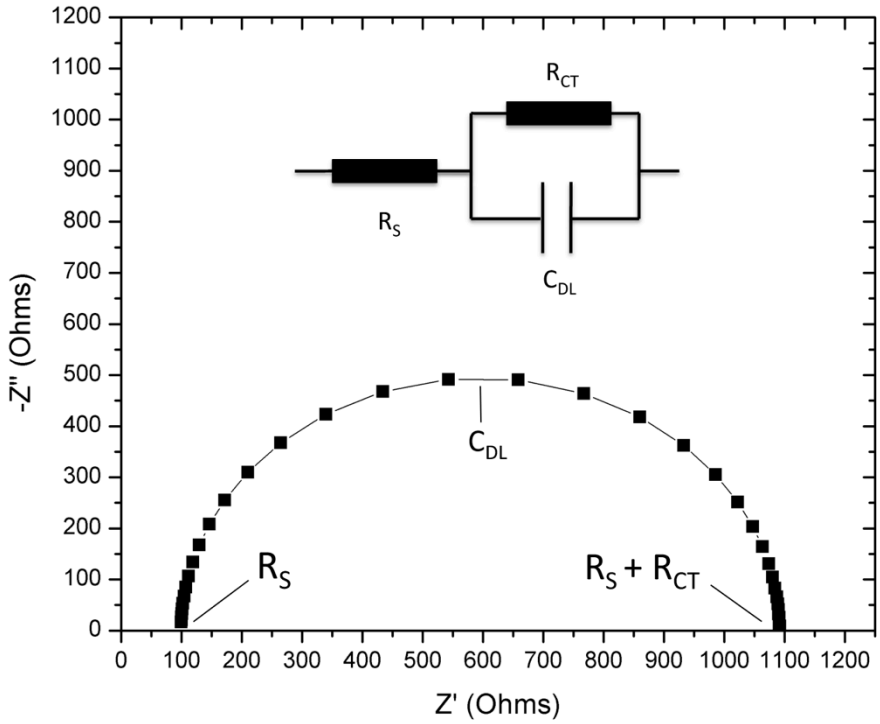

Figure 8: Nyquist plot of impedance data for a typical half-cell with insert of the equivalent circuit.

The limitation of EIS lies with the interpretation of the responses and the system must be operated in certain ways to gain insight into the specific processes that are dominant.

The high frequency intercept with the real axis (labelled R_s in Figure 8) is typically used to determine the total ohmic resistance in the system composed of contact resistances and electrolyte resistance. The low frequency resistance (shown in Figure 8 as $R_S + R_{CT}$) shows the total system resistance.

By far the most common use of EIS is where a range of frequencies is used to produce a full impedance arc (Nyquist plot). This technique is commonly used to compare systems in terms of arc diameter changes to view how an individual system changes under different operating conditions and assess how individual processes change over time periods and after specific operational changes.

1.8. Polarisation performance

The performance characteristics of the PEFCs are dominated by three key operational losses. A typical polarisation curve can be seen in Figure 9 with the three different regions shown in which different loss mechanisms dominate. The key performance losses are activation losses, ohmic losses and mass transport losses.

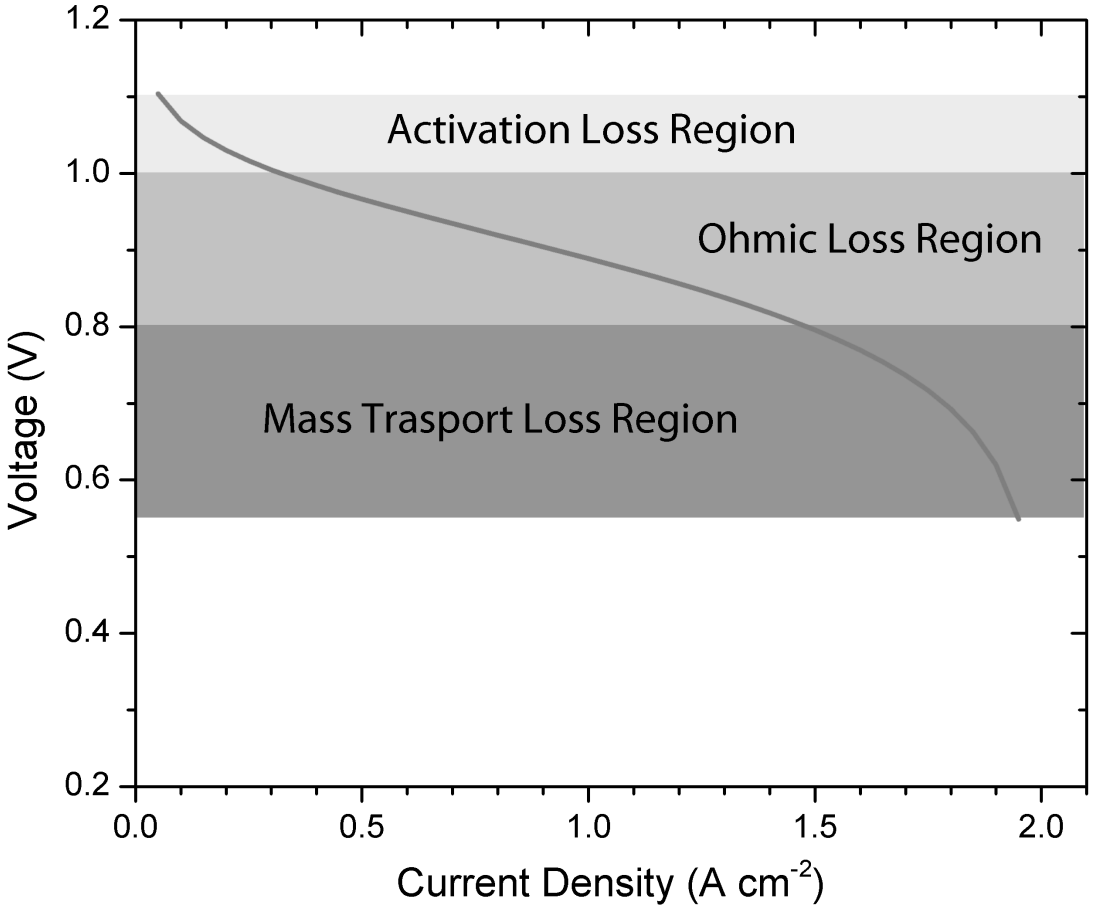

Figure 9: Example polarization curve showing approximately the three key regions of operational losses.

The well defined areas of the VI curve have been modelled extensively with a typical total VI curve model shown in Equation 7 [96].

Equation 7 $$V = E_{rev} - \eta_{act} - \eta_{ohmic} - \eta_{conc}$$

The following sections describe each of these terms.

1.8.1. Open circuit voltage (reversible cell potential)

The open circuit voltage of a PEFC can be modelled using the Nernst equation (Equation 8 [96]), which incorporates the free energy of reaction (E_0, Equation 9 [96]) and a thermodynamic term. The practical open circuit voltage (OCV) observed is usually lower still. The reduction from theoretical OCV is as a result of a number of processes within the cell including: reactant crossover through the membrane, contamination of the reactant gasses or system and electron 'leakage' through the membrane. These factors are mitigated to a certain extent by cell design such as using different membrane materials but using different material can have adverse effects on other parts of the polarization curve and as such a low OCV is not always the defining issue in overall performance.

Equation 8

$$E_{rev} = E_0 - \frac{RT}{nF} ln\left(\frac{P_{H_2O}}{P_{H_2} P_{O_2}^{0.5}}\right)$$

Equation 9

$$E_0 = \frac{\Delta H - T\Delta S}{nF}$$

From equations 8 and 9 the parameters have the following meaning; 'R' is the universal gas constant, 'T' is temperature, 'n' is mole equivalents, 'F' is Faradays constant, 'P' is partial pressure, 'H' is enthalpy and 'S' is entropy.

1.8.2. Activation losses

Activation losses dominate at low current density and are attributed to the voltage required to overcome the activation energy of the electrochemical reaction at the

electrodes. The activation potential loss is typically modelled using the Butler-Volmer (BV) equation and a common simplification of which is Equation 10 [96].

Equation 10

$$\eta_{act} = \frac{RT}{\alpha F} sinh^{-1}\left(\frac{i}{2i_0}\right)$$

The activation loss equation has two key parameters being the charge transfer coefficient (α) and the exchange current density (i_0). The sinh simplification of the BV equation is used, particularly with PEFCs, as the charge transfer coefficient (α) for the anode and cathode are often considered similar for a hydrogen/air system. The activation losses are affected by a number of factors including: catalyst layer morphology and type of catalyst used, operating parameter such as temperature and the degradation of the electrode.

1.8.3. Ohmic losses

The ohmic potential losses for PEFCs are the summation of the ionic and electronic resistances within the fuel cell. The voltage loss equation can be seen in Equation 11 where r_{comp} represents the various purely resistive components in the system [96].

Equation 11

$$\eta_{ohmic} = iA\left(\sum r_{comp}\right)$$

In this equation 'i' represents current density, 'A' the area of the component and 'r' the resistance. The ohmic losses are key to the operation of a PEFC as the typical operating region for a working fuel cell resides in the 'ohmic region' and hence

minimising the ohmic losses of the system is fundamental to good performance. The largest component of the ohmic loss is typically the ionic resistance of the membrane and electrode. Other important electrical resistances come from the contact resistances (particularly between the GDL and FFP) but also the resistances of the materials themselves.

Conductivities are commonly reported instead of resistance to describe the electrical properties of fuel cell components due to conductivities not being material geometry and test specific. In this thesis the measured property is resistance and this is related to resistivity (ρ) and conductivity (σ) thus:

Equation 12

$$\boldsymbol{\rho = R\,\frac{A}{l} = \frac{1}{\sigma}}$$

Where 'A' is the geometric area, 'l' is the thickness of the sample and 'R' the resistance of the component.

1.8.4. Mass transport losses

At relatively high current densities the performance of fuel cells become limited by the amount of reactant that can get to the surface of the electrode. This is a function not only of the supply (rate and pressure) of reactant gasses to the cell but also the level of cell compression. The equation for the concentration loss, is Equation 13 [96].

Equation 13

$$\boldsymbol{\eta_{conc} = \left[\frac{RT}{\alpha nF}\,ln\,\frac{i_l}{i_l - i}\right]_a + \left[\frac{RT}{\alpha nF}\,ln\,\frac{i_l}{i_l - i}\right]_c}$$

Equation 14

$$i_l = -nFD_{eff}\frac{C_\infty}{\delta} = -nFD\phi^{1.5}\frac{y_i P/RT}{\delta}$$

The limiting current equation (Equation 14 [96]) is the most commonly used approximation for the calculation of limiting current (i_l). The values calculated using this equation typically give limiting currents that are higher than in practice; this is potentially due to water management not being accounted for in the equation. Of particular interest in this equation is the inclusion of an effective diffusion coefficient (D_{eff}), as this is a function of the porosity and tortuosity of the diffusion medium; this will change when the compression of the cell is altered and varying level of crushing occurs. The effective diffusion equation is as follows.

Equation 15

$$D_{eff} = D\frac{\phi}{\tau} \cong D\phi^{1.5}$$

Where diffusivity (D), porosity (ϕ) and tortuosity (τ) make up the components of the effective diffusion coefficient (D_{eff}) and due to the complex nature of tortuosity measurement the common approximation (Bruggeman) used replaces tortuosity with a modified porosity value ($\phi^{1.5}$). The limitation of the Bruggeman approximation lies with the assumptions of the geometry of the system it is applied to, this is that the system is formed of spheres which is not the case for the fuel cell system. Of the alternative approximations the Bruggeman approximation is routinely used for PEM fuel cell modelling however there are alternatives that may approximate certain systems better [97].

2. Methodology

2.1. Experimental rig design

2.1.1. Testing rig and components

The process and instrumentation diagram for the fuel cell testing rig can be seen in Figure 10. Solid black lines represent the gas flow channels; long-dashed blue lines represent the automatic top-up system for the humidification bottles while the short-dashed red lines represent electrical connections.

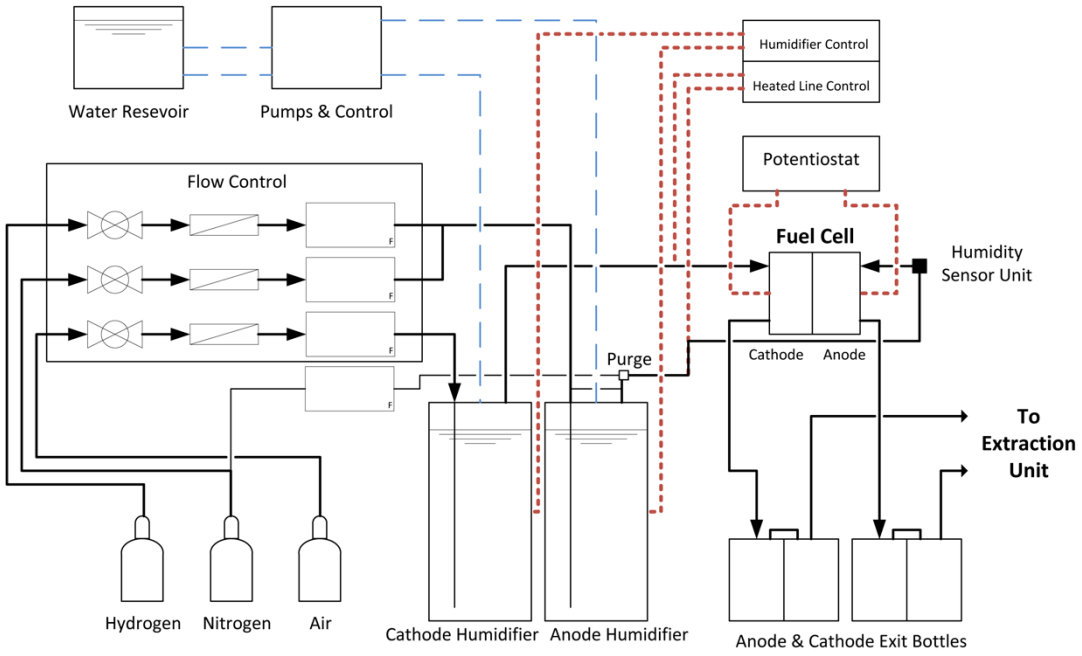

Figure 10: Process and instrumentation diagram for the fuel cell testing rig.

Gases were supplied by BOC (London, UK), zero grade gases are used with the following specifications; nitrogen (99.998% purity), air (99.998% purity) and hydrogen (99.995% purity). All gases are supplied in large size M bottles having a fill pressure of 220 barg. The regulators for the gas bottles (BOC plc., UK) have a 5 barg

maximum output and this is coupled with a flashback arrestor for the hydrogen gas cylinder.

Gas flow control was carried out using Bronkhorst EL-FLOW controllers (Bronkhorst, UK) designed for hydrogen, air and nitrogen at an inlet pressure of 3.5 barg and outlet pressure of 0.5 barg. Each flow controller was specified to deliver a maximum flow rate of 100 ml min^{-1}, a rate specified due to the size of fuel cells that testing was to be carried out upon. Control and data gathering was achieved through the control software.

The proportional integral derivative (PID) controllers used were supplied by Omega (Manchester, UK), the PID controllers (CNZ-7500 model) control the temperature of the water in the humidification bottles, the heaters for the heated lines and temperature of the heated humidity probe housing.

Aside from measurements taken from the PID controllers, the temperature measurements were interfaced to the computer using a datalogger, PICO TC-08USB (Farnell, UK). The thermocouples used were K- type thermocouples of 3 and 6 mm diameters and of lengths ranging from 70 mm to 150 mm.

The basic design of the rig, using Google Sketchup (Freeware, Version 7.0)(Figure 11 (a) and (b)), was constructed to utilise the space available. The rig has to fit between the bench mounted extraction units giving a total unit width of 1.45 m. A stainless steel (Orion Alloys Ltd., Essex) frame design was chosen for the strength, durability and flexibility of design. To cover the flat surfaces of the rig, Trespa Athalon panels

(Performance Panels Ltd., Halifax) were chosen due to their superior strength compared with traditional wooden type panels and also for their appearance. The completed rig allows the flexibility of being able to move it to anywhere in the lab complex (due to it being able to fit over any bench) where any extraction units are present. The design also utilises the space beneath the bench top, which would otherwise be dead space and increases the working area due to having a greater depth than the existing workbenches. A picture of the rig can be seen in Figure 11 (c).

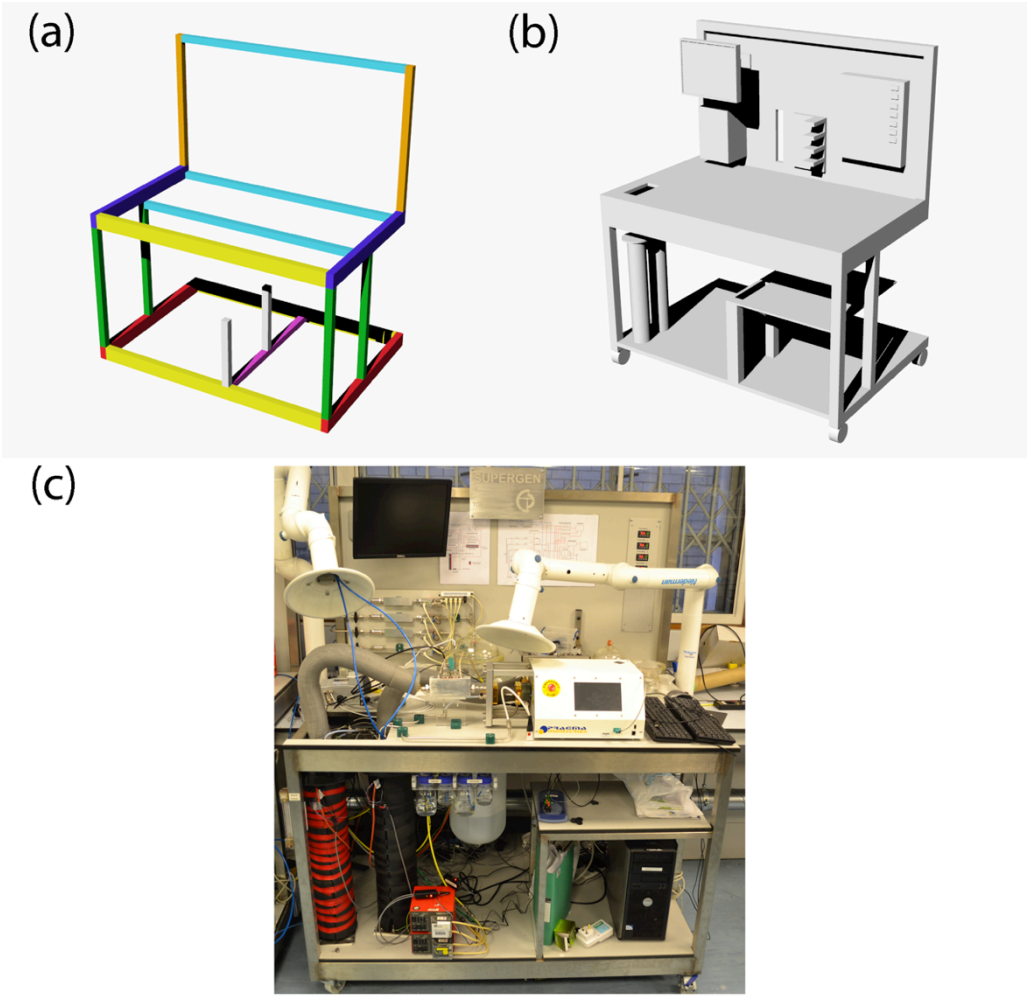

Figure 11: Fuel cell testing rig throughout the design and implementation phase from; (a) structural design; (b) initial concept and (c) completed operational testing rig.

2.1.2. Cell Compression Unit

Fuel cell operation was carried out using a commercially available cell compression unit (CCU) (Pragma Industries SAS, France), which allows controlled compression (resolution of 0.01 MPa) or displacement of the fuel cell with simultaneous relative real-time displacement measurement (resolution of 1 μm). The CCU features a 'floating piston' style fuel cell (Figure 12) that allows compression to be applied evenly onto the active area of the fuel cell to allow accurate measurement of the real compression applied to the active area of the MEA. The fuel cell used has an active area of 5 cm^2 using a single serpentine flow field design with land and channel widths of 1.2 mm and 1.1 mm respectively.

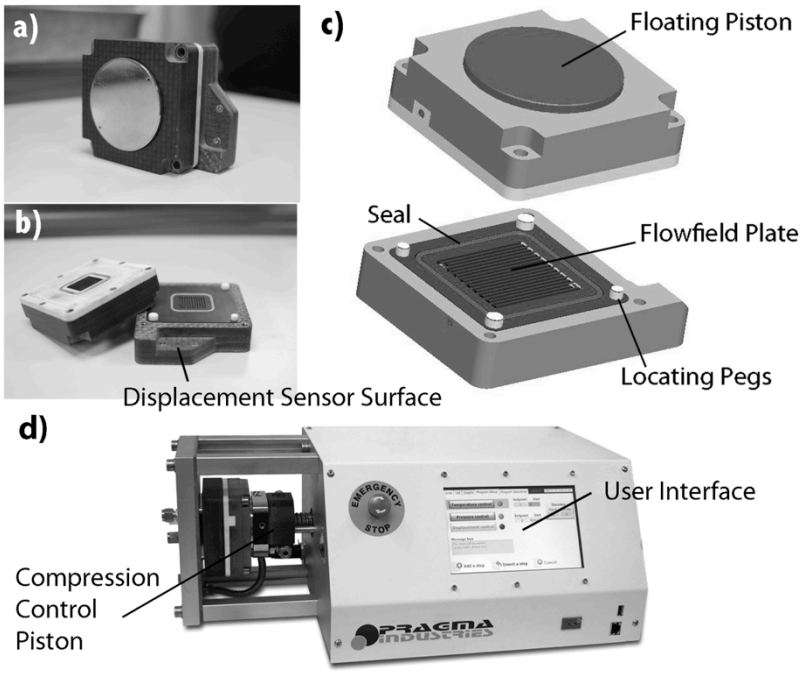

Figure 12: Key features of the cell compression unit (CCU) with: (a-c) 'floating piston cell' allowing compression of active area only; (d) compression unit with cell.

Temperature control, with an accuracy of ± <1 °C, was achieved with the CCU and all testing done at a fuel cell operating temperature of 80 °C. The measured effective thermal expansion coefficient of the CCU was determined to be 1.92 μm $°C^{-1}$ (see Figure 13), with the CCU able to maintain temperature to within ± 0.2 °C, meaning displacement variation during experiments due to temperature fluctuations was minimal (± <1 μm). When the CCU was operated in constant compression mode a setting of 0.2 MPa was used, this is the minimum compression for which no gas leaks occur.

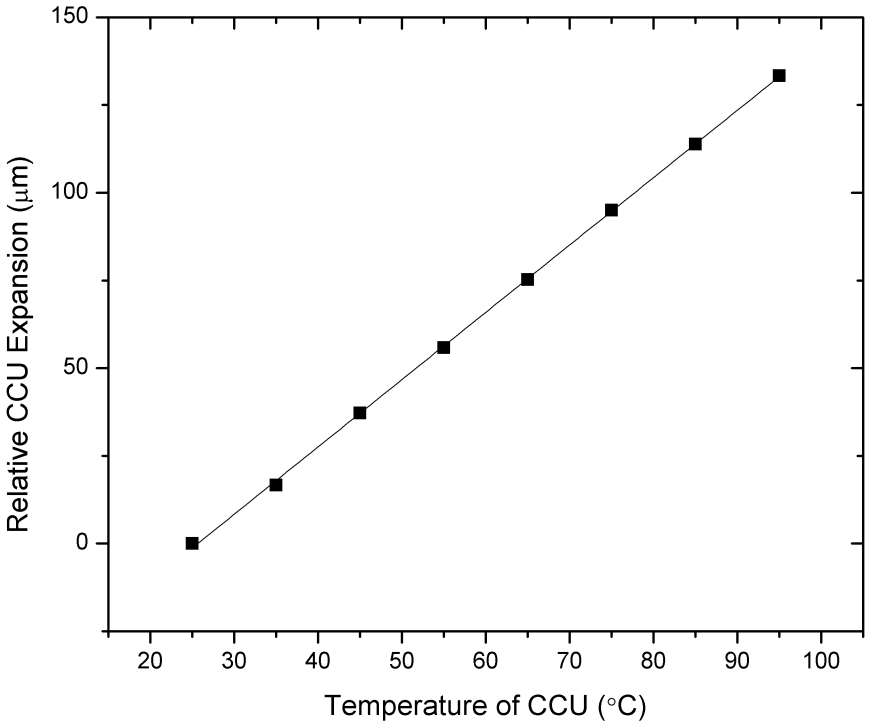

Figure 13: Calibration chart for the expansion of the CCU with change in temperature. The gradient of the curve gives a calibration factor (CCU temperature coefficient of expansion) of 1.92 μm $°C^{-1}$. The error in the CCU expansion measurement is ± 1 μm and the error in temperature measurement is ± 0.2 °C

With the cell empty (i.e. no GDL sample) and hence with only a BPP-BPP interface, the resistance value measured with EIS was 36 mΩ cm^2 at 1.5 MPa. In the presence of the GDL materials between the BPPs the measured resistance is typically < 20 mΩ cm^2, so attesting to the improvement in contact resistance achieved using a conformable material. The resistance values reported in this study are a summation of the BPP-GDL interface, fibre bulk resistance, GDL internal fibre connections and bulk system resistance.

The CCU can operate in two different modes to enable control and observation of the displacement and compression of the fuel cell. When control of the compression is desired the displacement is measured and vice versa, an expanding component is associated with a negative displacement response and an increasing force exerted by an expanding component denoted as a positive pressure change.

The different operating modes are depicted in Figure 14 using the analogy of a spring and piston for the GDL and electrolyte respectively. In controlled displacement mode (Figure 14 (b)), as the electrolyte hydrates (piston expands) the springs (GDLs) are compressed (crushed). In controlled compression mode (Figure 14 (c)), the piston expands and the thickness of the MEA increases, allowing the compression of the springs (GDLs) to remain constant.

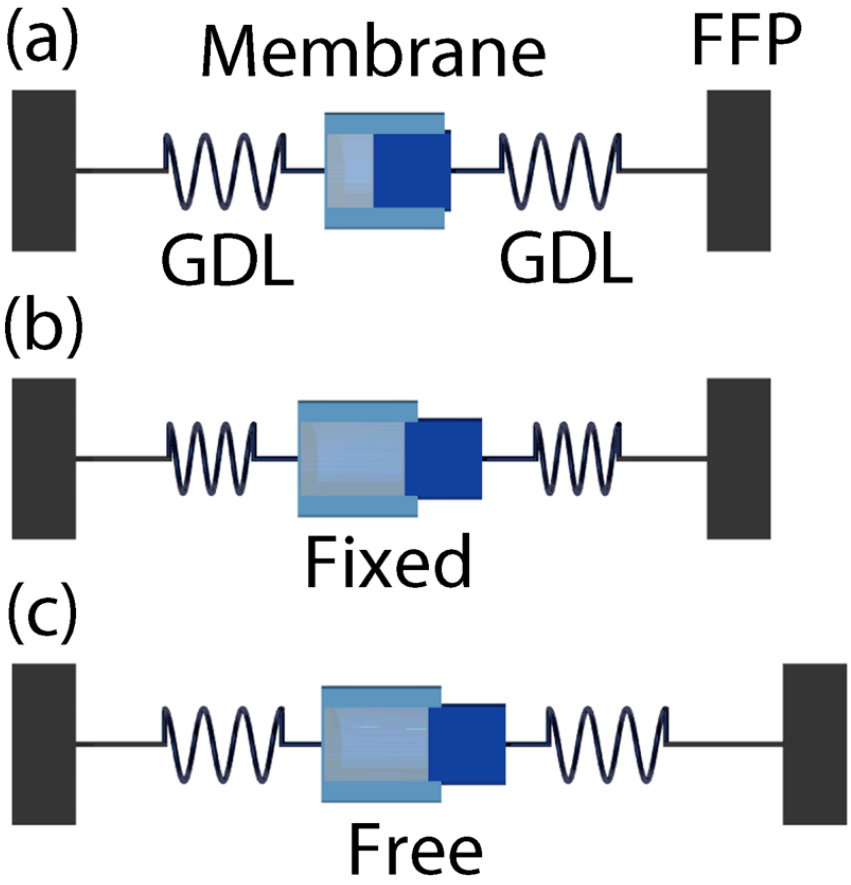

Figure 14: Illustration showing the differing operating modes of the CCU as an analogy between the MEA components and spring / piston mechanical connection. (a) MEA system within two flow field plates and the GDL and electrolyte shown as a spring and piston respectively; (b) Electrolyte membrane swelling in controlled displacement mode, the piston expands the springs are compressed; (c) controlled compression mode, the electrolyte expands and the compression remains constant leading to displacement of the flow field plates and no compression of the springs (GDLs).

2.1.3. Electrochemical control

Electrochemical control of the system was carried out using a combination of an Ivuimstat and an Iviumboost (Alvatek Ltd., UK) depending upon the specific experiment. For single component testing the Iviumstat alone was used, when any MEAs were being tested the Iviumboost was used to sink the current generated by the operating cell. An Iviumstat can cope with currents up to 5 A, but it was noticed that during fuel cell testing, current ranging issues occurred. The current ranging issues were fixed by using the Iviumboost, which can cope with currents up to 40 A.

When carrying out resistance measurements using EIS, a set frequency of 5 kHz and amplitude of 15 mV was used. This frequency was chosen after running a full impedance frequency sweep with the frequency closest to the high frequency intercept being chosen. When performing full impedance scans, a frequency range of 20 kHz to 0.5 Hz and amplitude of 15 mV was used with 10 frequencies per decade.

2.2. Humidification

The humidification system for the test rig involves “humidification bottles” which enable the gas stream to pass through a volume of water so that mass transfer can occur allowing the gas to be hydrated, then “heated lines” which provide a passage for the humidified gas enabling the water in the gas not to condense out so that fully humidified gases can enter the fuel cell. The nature of the experiments performed means that robust control of reactant humidification was necessary and extensive development work was undertaken to ensure this. This section explores the design methodology behind the system and it’s testing.

The humidification system is such an important process as the performance of the fuel cell system is highly dependent upon the water management properties. It is also important that the humidification system is reliable and repeatable so that the results obtained from experimentation can be relied upon. A process and instrumentation diagram (P&ID) of the humidification system can be seen in Figure 15.

The traditional method for providing basic humidification in the lab environment is the use of bubble bottles, which are placed in a water bath to provide the heating, required to the water. This method however does have some major drawbacks; the bottles cannot be topped up with water without stopping the flow of gasses so if the experiment runs over a long period of time the humidification level will drop with the water level, also the gas is unlikely to fully hydrate due to the short residence time of the bubble in the water and the large bubble size, meaning a relatively small surface area. The bespoke humidification system outlined in this section aims to eliminate the inherent problems with the traditional process.

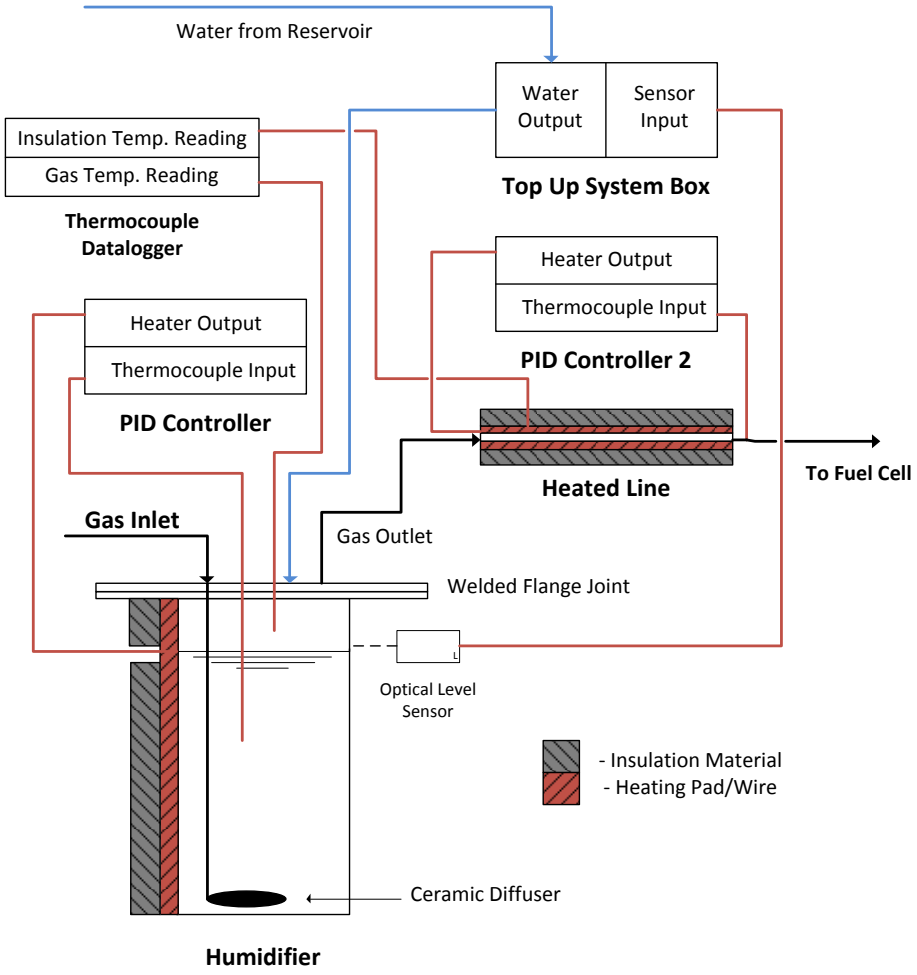

Figure 15: Process and instrumentation diagram (P&ID) for in-house humidification system

2.2.1. Humidification bottles

The design for the humidification bottles was done in such a way as to utilise the space that was available on the testing rig frame so as to have the maximum length of residence time of the gas in the water (so that the vapour pressure of water in the gas steam is fully equilibrated for the temperature of the liquid water selected). The initial design for the humidification units can be seen in Figure 16.

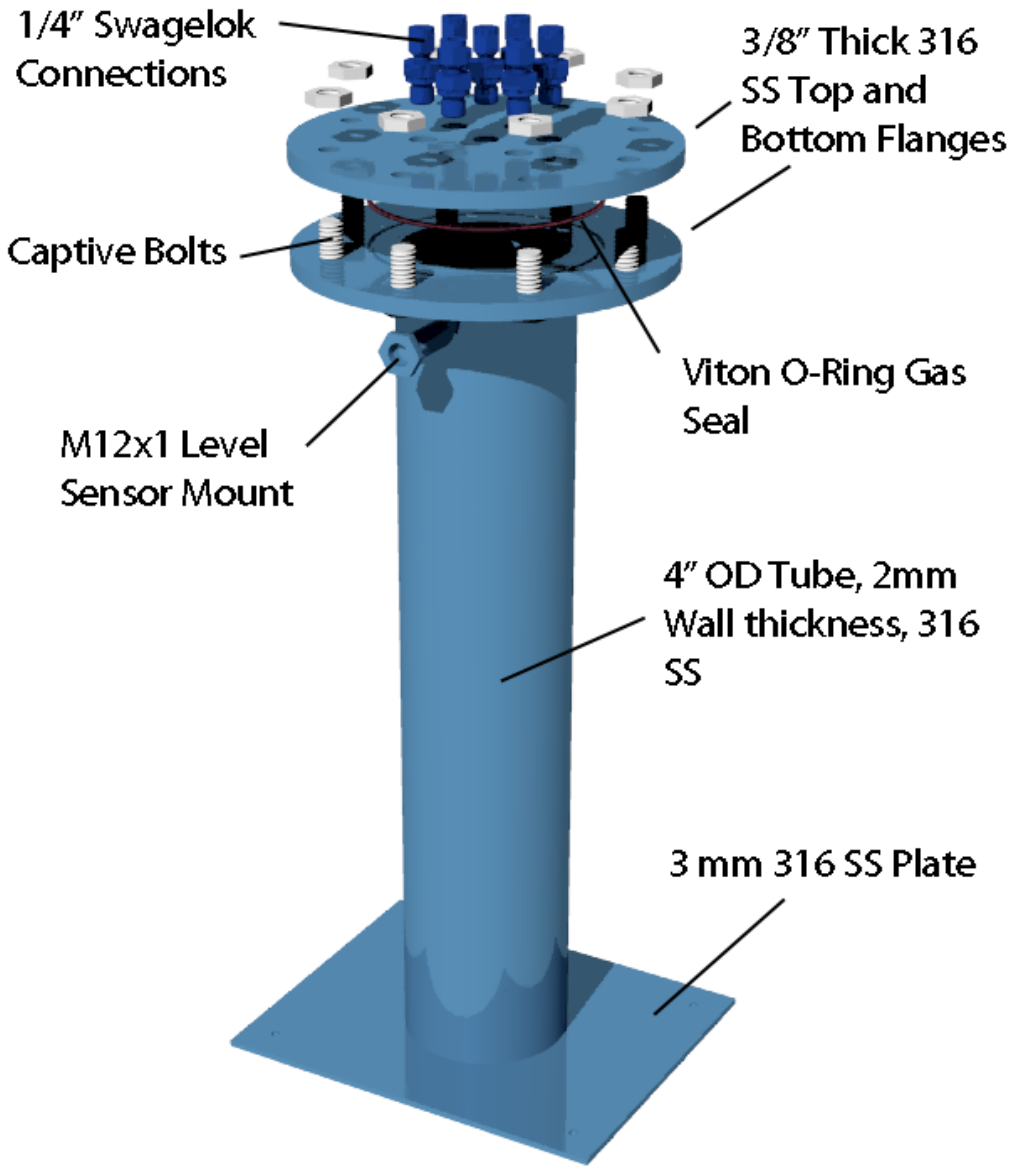

Figure 16: Initial design for in-house humidification units.

To maintain the water temperature in the bottles a method of heating was required that provides a reliable source that also produces a uniform water temperature. Of the methods available, including immersion heaters and clamp heaters, a flexible pad heater was chosen. These pads (Chromalox, UK) were wrapped around the outside of the bottles resulting in heat being evenly applied and creating a consistent water

temperature when it is maintained at the set point by a PID controller (CNZ7500, Omega, UK).

When the gas enters the humidification system it will only absorb the maximum amount of water through mass transfer if the gas is at its saturated vapour temperature. The solution to this is to have a long coiled stainless steel tube running down the inside of the bottle so the gas must pass though the tube before it enters the water. Due to the length of the tube and its material there will be heat transfer to bring the temperature of the gas stream nearer the temperature of the water. The alternative way of producing this would be to add a gas heater before the system, this was evaluated but due to the costs involved the coiled tube was chosen as a lower cost alternative.

A critical part of the mass transfer is the residence time of the gas bubble in the water, with smaller bubbles the surface area to volume ratio is greater and the bubbles will rise slower, increasing their residence time. A gas diffuser was added to the bottom of the coiled stainless steel tube to produce smaller bubbles.

As this project involves running degradation experiments, the system needed to be run for long periods of time. The humidification bottles need a system of topping up the water to avoid the water level dropping and potentially running dry. In addition, the water running low would cause there to be a high inventory of hydrogen inside the anode bottle which is not desirable from a safety point of view but also the performance of the bottles may reduce as the residence time in the water will be reduced if the water level drops. As mechanical systems are susceptible to failure over

long periods of time an electrical system was chosen that involves an optical sensor that switches on a pump that will pass water in to the top of the bottle topping up the reservoir.

From calculations, the largest amount of water that will be removed will be in the region of 3 g hr^{-1}. This means that the water level will likely drop by 0.00925 cm hr^{-1}. Due to this small number it is not necessary to have the top up system on continuously so the system will be turned on periodically, once a week, to top up the water. The reason this is required is that the optical sensor works intermittently because the gas bubbles rise, create turbulence at the water surface and interfere with the sensor. When the flow rate increases the sensor turns the pumps on intermittently, this is important, as the pumps are not on when the flow rate is zero.

On completion, the bottles were subjected to tests without the insulation to make sure that the insulation wouldn't be exposed to temperatures exceeding the operating range, to test this the heating pads had a silicone paper layer added to the outside of the bottles and a thermocouple added to measure the temperature. Figure 17 (A) shows the bottles without insulation and the thermocouples attached. Once these tests were successful the next stage was to fit the insulation to the bottle to prevent heat loss and to provide a more efficient system, which can be seen in Figure 17 (B).

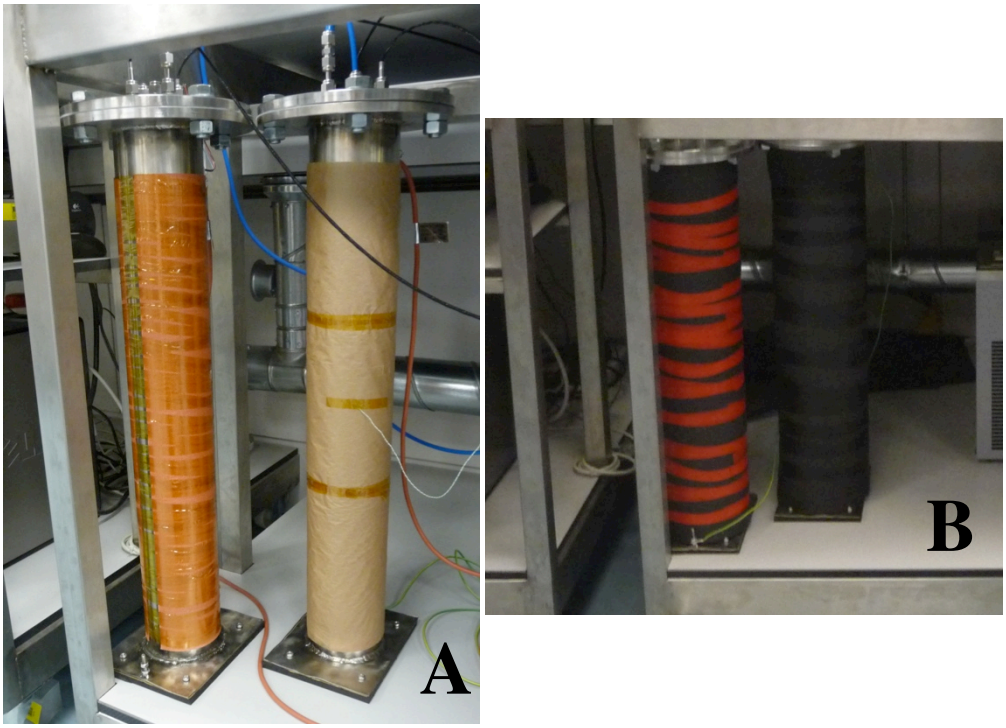

Figure 17: 'A' shows the humidification bottles being tested to check the outside temperature of the bottle does not exceed the insulation's operating temperature. 'B' shows the completed bottles with insulation attached.

2.2.2. Heated Lines

The heated lines were designed to provide a flexible passage that has a controllable, even, internal surface temperature so that the gas temperature would not drop, resulting in the water condensing on the walls of the lines. For this reason a flexible rope heater with a gas stream thermocouple near the outlet of the line was chosen in addition to insulation being applied to the heated line. The final design for the lines can be seen in Figure 18.

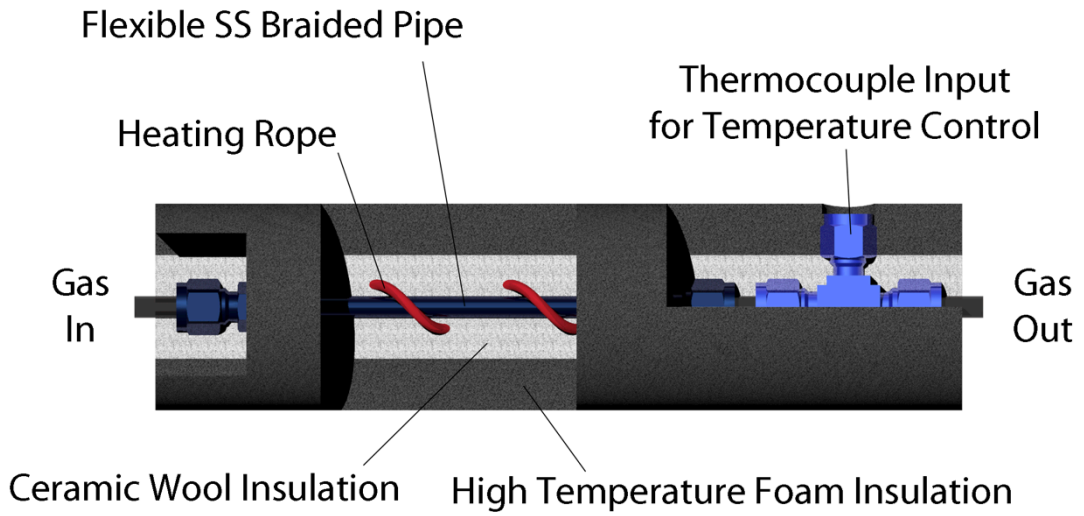

Figure 18: Diagram of the heated lines showing the key features of the design

Initially the heated lines had insulation put around the heaters but due to the slow nature of the heat transfer the temperature of the rope heaters rose to about 220 °C. The next stage was to improve the insulation and the heat transfer, this was done by putting a layer of ceramic wool around the heater and then this was tightly wrapped with a high temperature tape to increase both the heat transfer by conduction and the insulation. The layer of pipe insulation was then added back to the outside to further improve the insulation of the lines. Figure 19 shows the heated lines integrated into the test rig system.

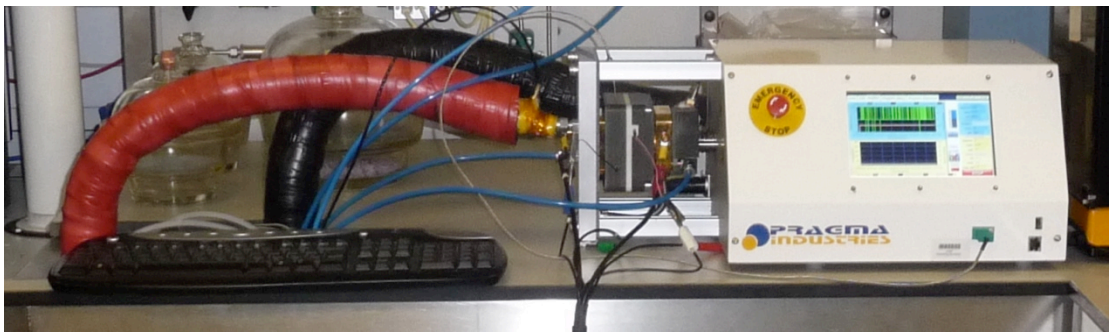

Figure 19: Picture of heated lines integrated into the rig system

2.2.3. Humidity measurement

Due to the importance of the humidification level of the gas steams, a heated probe humidity sensor (Vaisala HMT337, Sweden) was installed into the system. Figure 20 shows the initial design for the heated housing used for installing the sensor. Despite the sensor having a heated probe the housing was required to be heated as well to ensure that no water condensed on its transit towards the fuel cell. An aluminium housing was chosen due to its excellent heat transfer properties with two 100 W cartridge heaters that are controlled using the PID controllers on the test rig.

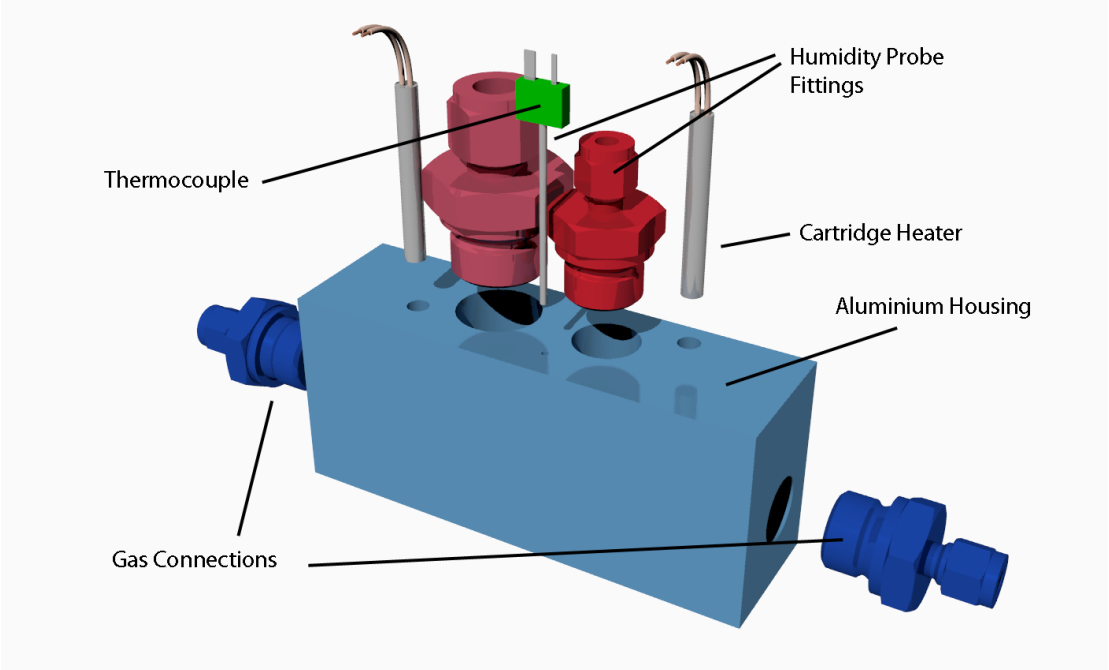

Figure 20: Initial design for humidity probe housing design for use with HMT337 (Vaisala, Sweden) humidity and temperature probes.

The sensor collects data in real time for the temperature and relative humidity of the stream and the dew point temperature of the gas. Having this data, whilst performing each experiment, allowed for dynamic control of the humidification parameters

ensuring that the humidification level of the gases was kept within a certain degree of accuracy. In practice the dew point temperature of the gas was controlled to within 0.5 °C of the target dew point. The completed humidity sensor and housing as it is installed on the test rig can be seen in Figure 21.

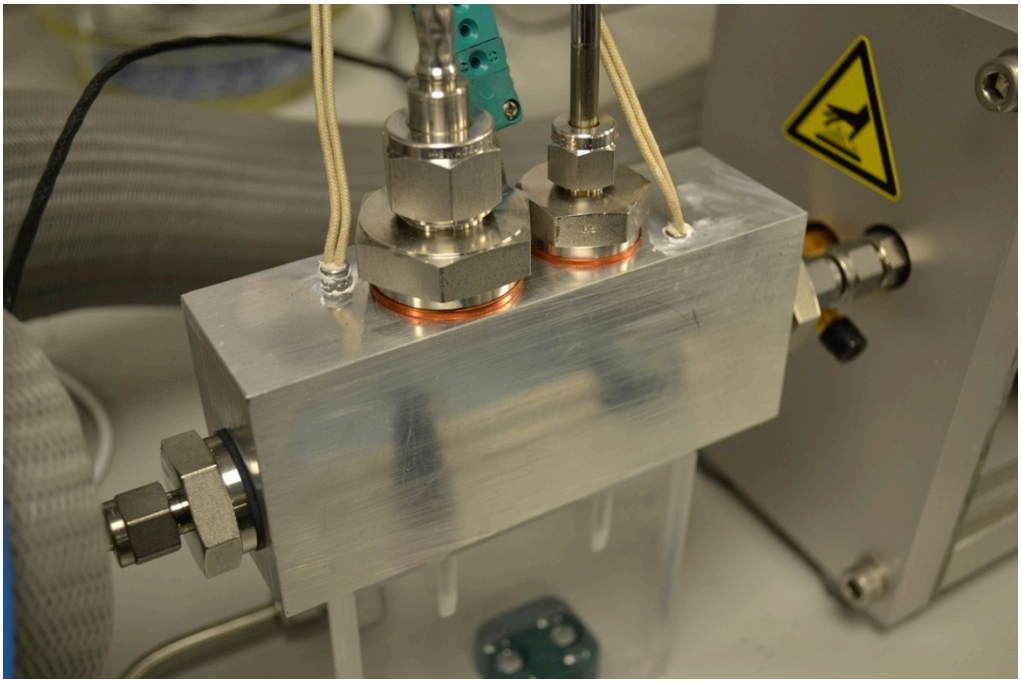

Figure 21: Humidity sensor and housing installed on fuel cell testing rig.

2.3. Electrolyte, GDL and MEA preparation

Electrolyte preparation (for Nafion 117, 115 and 212) was carried out using the following procedure, this process was carried out before each MEA was made or electrolyte material was tested:

- Cut the electrolyte to the required size from rolled sheet
- Soak in preheated 80 °C 3% H_2O_2 (Sigma Aldrich, UK) for one hour to remove organic compounds from the material
- Rinse thoroughly with deionised water

- Soak in preheated 80 °C 1 M H_2SO_4 (Sigma Aldrich, UK) for one hour to protonate the membrane
- Rinse thoroughly with the deionised water
- Store treated samples in deionised water until needed

The MEAs used were produced in-house using Nafion 212 or Nafion 117 electrolyte (Fuel Cell Store, US) and Alfa Aesar electrodes (045372, Alfa Aesar, UK) with an active area of 5 cm^2. The MEAs were pressed (Carver 4122CE, US) at 170 °C for 4 min with a pressure applied of 450 PSI. The cells were stored at room temperature and humidity prior to pre-conditioning before each experiment.

Pre-conditioning of the fuel cells was carried out by flowing 100% RH nitrogen and air over the anode and cathode respectively at a flow rate of 100 ml min^{-1} each for 30 min followed by 100% RH hydrogen and air at 100 ml min^{-1} for 30 min at 100 mA cm^{-2}.

Ex-situ Nafion water content experiments were carried out by measuring the thickness at three random points on the membrane using a micrometer, then taking an average. Weight measurements were taken using an analytical balance (Sartorius MC1 Analytic AC 210 P, US) with the water content controlled by immersing the samples in deionised water at 80 ºC for 1 hour, then removing and measuring the thickness and weight every two minutes to build up the data set as the sample dries. This process was repeated multiple times to build up the data set. Data for low water content were taken after >1 hours of storage in a drying oven at 110 ºC.

A range of commercially available GDL materials, as summarised in Table 7, was tested *in-situ* (Section 3) The materials were all 'pure' GDL without microporous layers (MPL) and used as received.

Table 7: Commercially available GDL materials tested.

Manufacturer	Type	Description
Ballard	1071HCB	Carbon cloth
	P75	Carbon paper
Sigracet	GDL 24 BA	Carbon paper with 5% PTFE loading
Toray	TGP-H-060	Carbon composite paper with 5% PTFE
	TGP-H-120	

The materials that were tested *ex-situ* (Section 4) are summarised in Table 8. The materials tested contained a mixture of 'pure' GDL, GDLs with micro porous layers and GDLs with various PTFE loadings.

Table 8: GDL materials that were tested *ex-situ*

Manufacturer	Type	Description
Ballard	1071HCB	Carbon cloth
	P50	P50 is the carbon paper substrate; P50T is a Teflonated carbon paper substrate; GDS 1120 contains a MPL
	P50T	
	GDS1120	
	P75	P75 is a carbon paper substrate; P75T is a Teflonated carbon paper substrate; GDS 2120 contains a MPL
	P75T	
	GDS2120	
Toray	TGP-H-030	Teflonated carbon papers of various thicknesses
	TGP-H-060	
	TGP-H-090	
	TGP-H-120	
Freudenberg	C2	Felt fibres carbon paper based on H2315 substrate

	C4	with a MPL applied
	I2 C6	Felt fibres carbon paper based on H2315 I2 substrate with a MPL applied
	I2 C8	
E-TEK	LT 1200 N	Non-woven web containing a MPL
	LT 1200 W	Woven web containing a MPL
Sigracet	GDL 10 BC	3D fibres carbon paper containing a MPL
	GDL 24 BA	A carbon paper with PTFE and with/without MPL. BA stands for 5% PTFE loading and no MPL. BC stands for 5% PTFE loading with a MPL DC stands for 20% PTFE loading with a MPL
	GDL 24 BC	
	GDL 25 BA	
	GDL 25 BC	
	GDL 34 BC	
	GDL 34 DC	
	GDL 35 BA	
	GDL 35 BC	
Tenax	TCC2660	Untreated woven carbon cloths
	TCC3250	

2.4. Software control

Control of the hardware on the fuel cell rig was achieved using a bespoke design using the LabVIEW programming language (LabVIEW 2009, National Instruments). The advantage of this system is that it allows control of hardware, data collection and visualisation on one piece of software that can then be controlled on the rig or remotely via remote desktop software (Teamviewer, Version 7). During operation of the test rig the mass flow controllers and PID controllers are directly controlled in LabVIEW while all the thermocouples on the test rig are read and the data stored in real time. The data collected is plotted in real time and also saved to a spreadsheet every 30 seconds to ensure that no data is lost in the event of power failure. The

LabVIEW interface and key features of the block diagram can be seen in Figure 86 to 89 (Appendix A).

2.5. SEM, EDS & GDL property measurement

Scanning electron microscopy (SEM) was carried out using a JEOL JSM-6480LV electron microscope (Jeol Ltd., Japan) with energy dispersive spectroscopy (EDS) using an Oxford Link system. The details of each individual image can be seen in the result section.

'Real' density (g cm^{-3}) values were measured using a helium pycnometer (Micromeritics AccuPyc II 1340). A sample of the GDL material was weighted (around 50 mg) and placed in the testing cup, and then 10 readings for the density were taken over 10 cycles of pumping and evacuating helium on the sample.

Bulk density (g cm^{-3}), porosity (%), tortuosity (dimensionless), pore size distribution and permeability (m^2) were measured using a mercury porosimeter (Micromeritics AutoPore IV). Here, the measured permeability corresponds to mercury permeation through the GDL with increasing pressure (MPa). Experimentally, a 1 cm^2 GDL sample (ca. 200 mg) was placed in the porosimeter stem to undergo low and high pressure mercury intrusion testing. Mercury was then deposited/inserted gradually into the sample by increasing the pressure up to 30,000 psi (~206 MPa) whereby the GDL sample pores were filled starting from the larger pores at low pressures and down to smaller pores at higher pressures. This method allowed the measurement and

determination of total pore volume, skeletal volume, real and bulk density as well as total porosity values.

Here, the Micromeritics AutoPore IV software uses the Washburn's equation [98] to determine the pore size distribution and the pore length of the GDL sample based on the assumption that the pores are of cylindrical geometry. Furthermore, the Katz and Thompson's equation [99, 100](derived from the percolation theory) is used by the software to calculate the absolute permeability (k) of the GDL sample. The permeability values are then used in the expression derived by Jörgen Hager to calculate tortuosity [101]. In the experimental work (Section 4), all these values were automatically calculated by the Micromeritics Instruments software as detailed and explained in a paper published by Micromeritics Instruments Corp. [101].

2.6. In-house rig development

In order to further develop and refine the experimental techniques presented in this work, in-house rigs were developed that offer several enhancements to the commercial system. Initially a single cell system that replicates the cell compression unit was developed followed by the designs for a stack system.

2.6.1. Single cell rig

The initial driver for designing an in-house compression rig was to increase the level of reliability and accuracy of the displacement and compression control. The in-house compression rig also enables the flexibility of being able to be used for compression

experiments of different types by removing the fuel cell plates. Design of the fuel cell compression rig was carried out using Rhinoceros (Version 4.0) CAD software with a screenshot of the design shown in Figure 22.

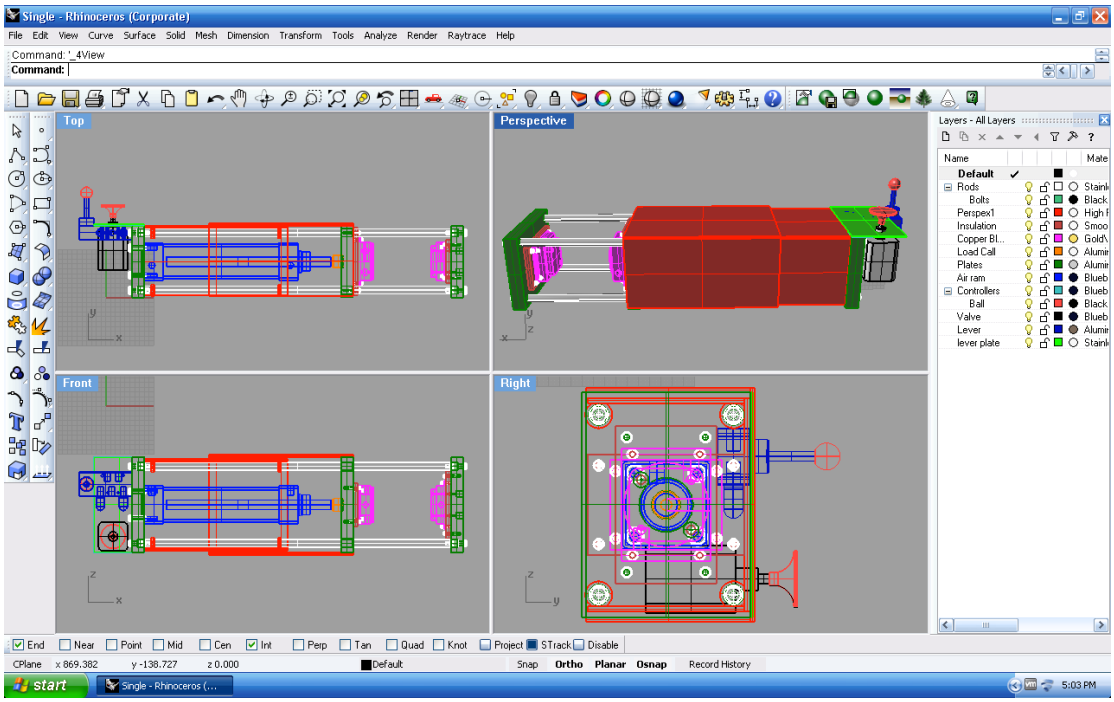

Figure 22: Screenshot of the CAD design for the single cell compression rig.

The commercial CCU offers a displacement resolution of 1 µm, while this is a relatively small resolution, in terms of contact displacement (LVDT type) resolution this is fairly large. Omron (ZX-TDS04T-L) provided the displacement measurement system chosen, which offers a resolution of 0.1 µm.

Of particular importance in the design of the fuel cell rig was the precise location of the Pragma type fuel cell into the system, an anode and cathode block were produced to line up the inlet of the fuel cells with the cradle (see Figure 23). A number of key considerations were made in the design of the anode and cathode blocks including the

internal gas channels for the reactant inlet and outlet, the location of the heating system, the sealing of the blocks against the cradle and the mounting of the blocks to the insulating plastic. Oxygen free copper blocks were used which were then coated with 5 µm silver and 2 µm gold to prevent corrosion and provide a good electrical connection (PMD Group, UK). The copper blocks contain two 100 W cartridge heaters (724-2052, RS Components, UK) that are controlled using PID controllers included in the rig system. To insulate the fuel cell from the cradle an engineering plastic was used which is advantageous due to its high-strength, high electrical resistance and low cost.

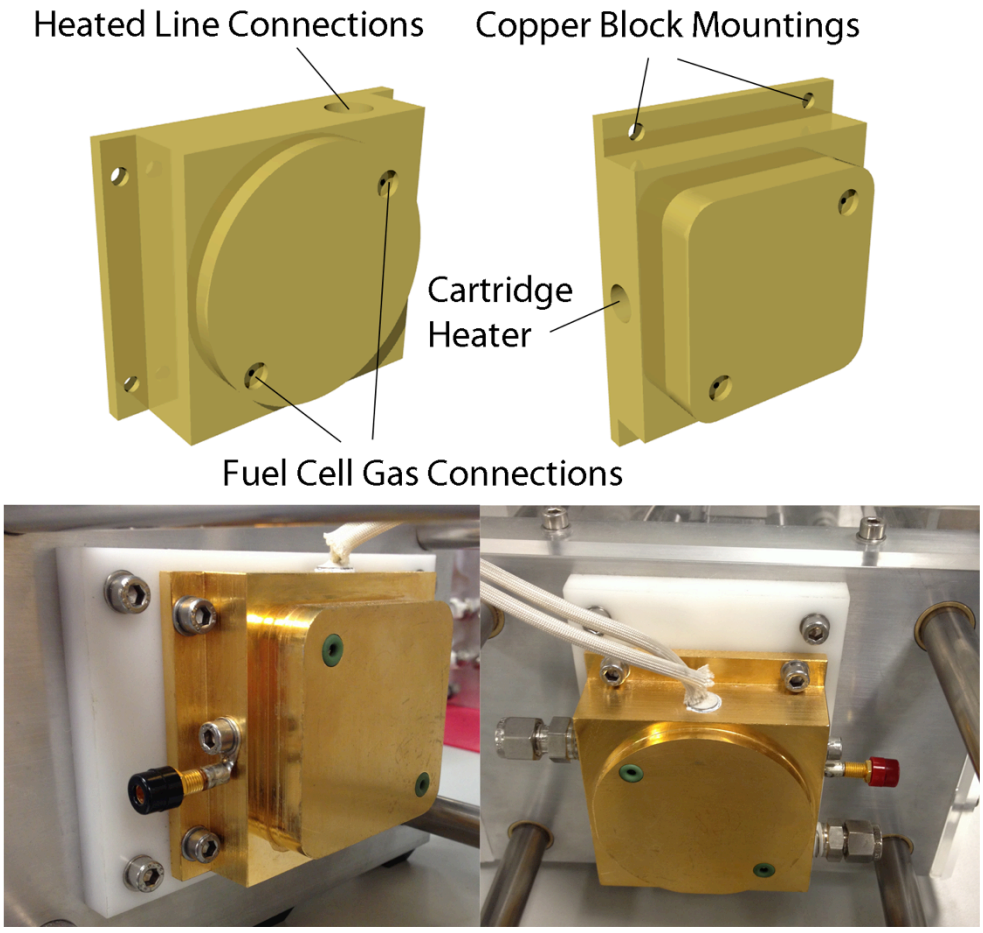

Figure 23: Anode and cathode mounting blocks for use with the Pragma cell (see Figure 12)

The cradle itself was made from plates of aluminium with stainless steel rods. The three aluminium plates (Figure 24) perform distinct roles and are designed accordingly; the static endplate is designed to enable the anode gases to pass through it, the floating plate is designed to use bushes against the stainless steel rods to enable smooth movement along the compression plane and the pneumatic ram mounting plate is designed to rigidly mount the compression piston. The floating plate uses brass bushes (AM1620-25, Simply Bearings, UK) which were reamed to fit ensuring high linearity in the movement of the plate.

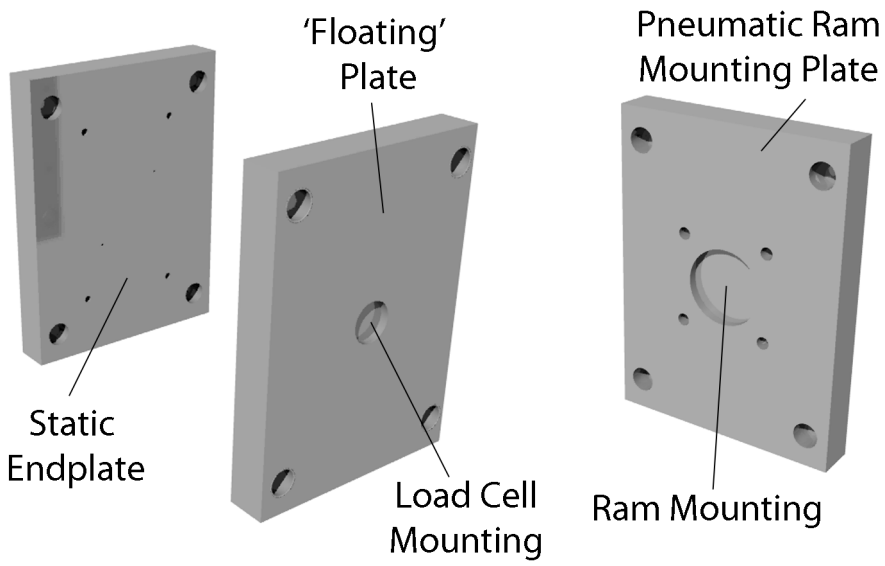

Figure 24: Designs for the three aluminium plates of the cradle.

The complete initial design for the single cell compression unit can be seen in Figure 25 along with the finished unit. The single cell compression rig was designed to use the Pragma type 'floating piston' cell design, the compression is applied pneumatically with a ram (H1M63/160C, Air Engineering Control Ltd., UK) that transfers its force to a load cell (LC304-100, Omega, UK) in the back of the floating

piston plate. The air ram was sized enabling a compression of up to 3 MPa on the fuel cell (of 5 cm^2 active area). The control of the air pressure in the ram was achieved using a high precision air valve (100-BCU, Air Engineering Control Ltd., UK) in conjunction with a control lever that allows the ram to be moved in and out to enable loading of the fuel cell and an absolute gas pressure gauge (LEO 2, Keller). A two part Perspex cover was designed to encase the ram section of the rig with a static section mounted to the rods and control endplate and a moving section attached to the floating plate allowing the ram to remain covered at all times.

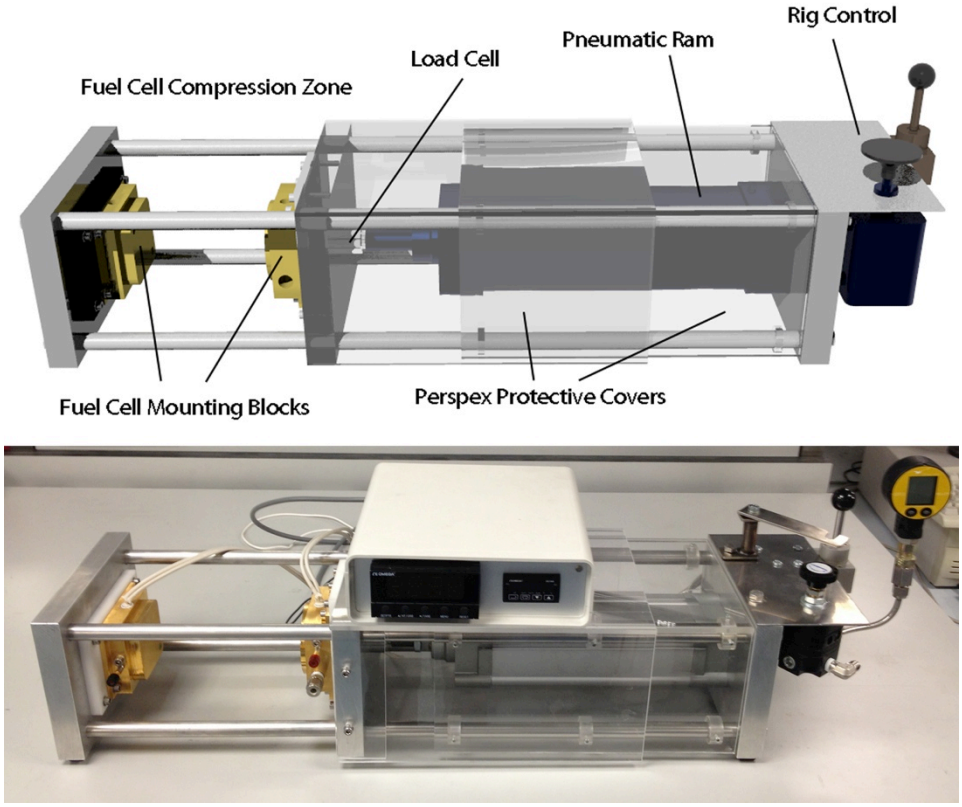

Figure 25: Initial rendered design for in-house single cell compression rig and the completed experimental rig with load cell and heater control box.

In order to enable testing on a variety of cell sizes and flow field designs it was necessary to design an in-house 'floating piston' cell which could be used in a

commercial CCU or the in-house designed single cell compression rig. Figure 26 shows the rendered design with our interpretation of the floating piston design. The design allows interchanging of the flow field plates, thus allowing for different size active area cells and flow field designs.

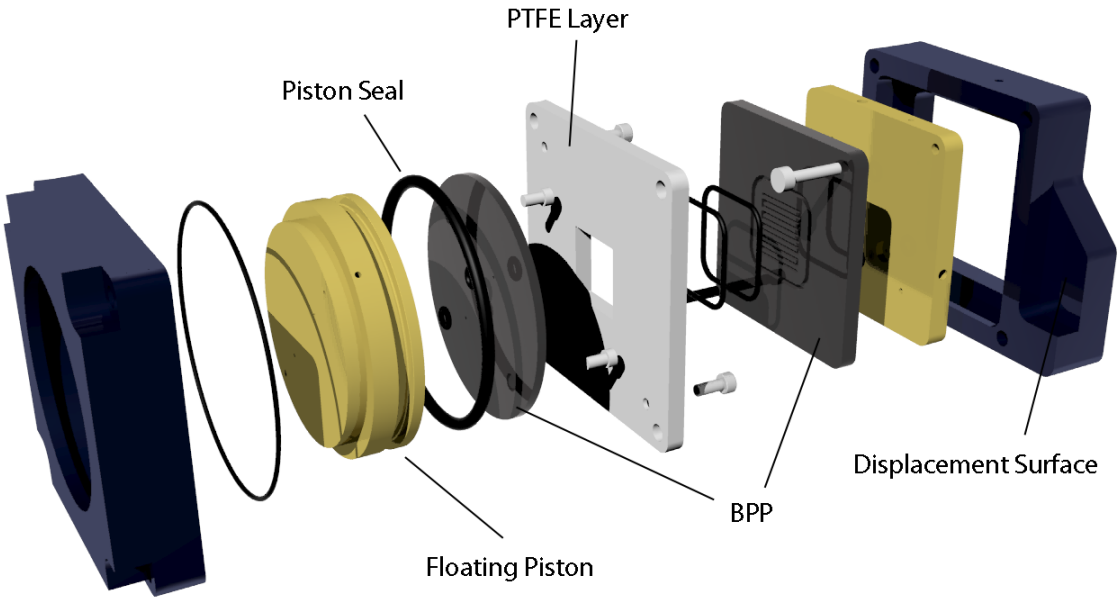

Figure 26: In-house designed compression cell to enable interchangeable cell size and flow field design.

2.6.2. Stack rig

A natural progression from the single cell in-house compression rig was to design a system allowing compression of a fuel cell stack. The stack rig was designed to incorporate displacement measurement and additional testing technology including compression and possible current mapping. The bespoke fuel cell stack with all its components can be seen in Figure 27, there is significant scope to alter the design of individual components such as flow field plates and look at how this affects the

overall performance of the fuel cell stack. The fuel cell active area is designed to be 100 cm^2 representing a commercially relevant fuel cell size, there is also scope to change the shape and size of the MEAs in order to test different fuel cell stack designs.

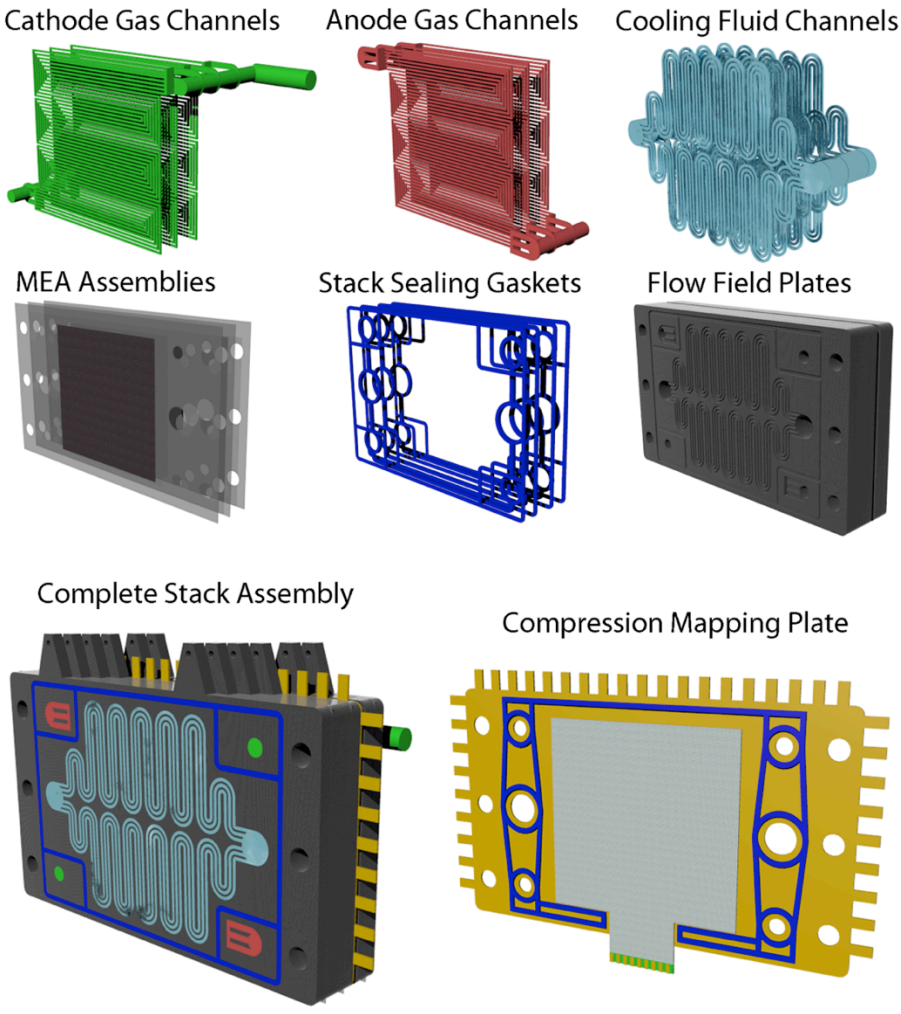

Figure 27: Composition of the bespoke fuel cell stack including the compression mapping plate.

Figure 28 shows an image of how the fuel cell stack is incorporated into the compression rig. The significant design components incorporated into the stack assembly are the flow field and compression mapping plates. The stack design

incorporates liquid cooling channels alternating between the MEAs in the stack; the compression mapping plate is designed to fit in between these cooling channels. The importance of the fuel cell stack design is that it is scalable in a sense that it can be run as a single cell up to a theoretical 9 cell stack, although a larger than 9 cell stack is possible with longer cradle rods, with the compression mapping plate located at any point within the stack.

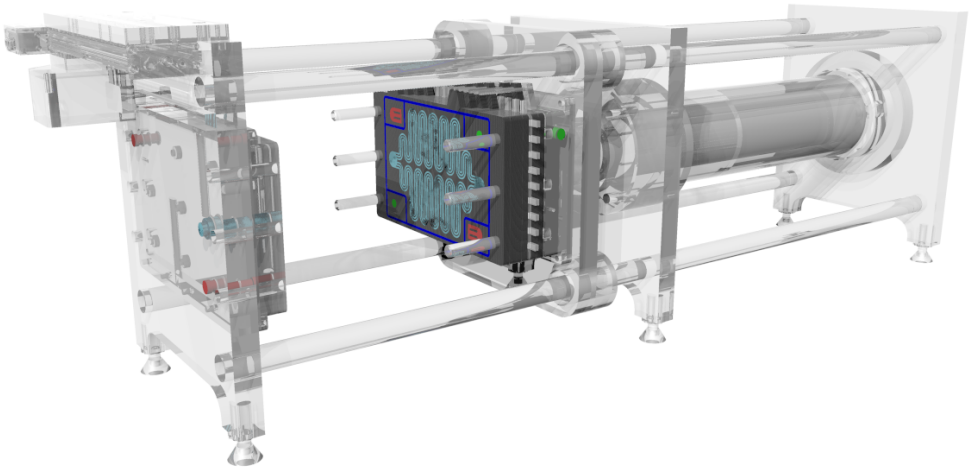

Figure 28: Image of how the fuel cell stack fits within the compression rig.

Figure 29 shows the design for the fully assembled fuel cell stack compression rig. The design incorporates a pneumatic compression ram (similar to single cell compression rig) capable of delivering compression of up to 3 MPa (30,000 N) over the 100 cm^2 active area.

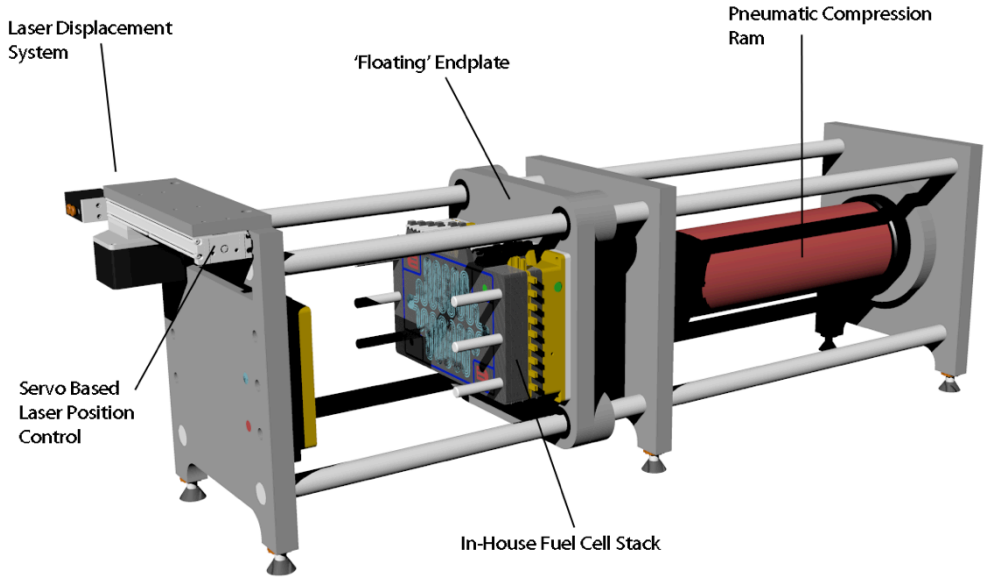

Figure 29: Stack compression rig design to enable full displacement measurement of individual cells and compression mapping.

The design of the stack compression rig cradle (seen in Figure 30) differs slightly to that of the single cell compression rig thanks to lessons learned from its construction. In particular the design changes include the additional of a cradle plate to increase the stability of the cradle rods (necessary due to the increase in span of the stack rig over the single cell rig), the slot gap used to guide the laser displacement measurement system and the adjustable height rig feet to ensure the system remains completely level. The stainless steel full-length cradle rods are made from precision turned bar to ensure as high as possible straightness.

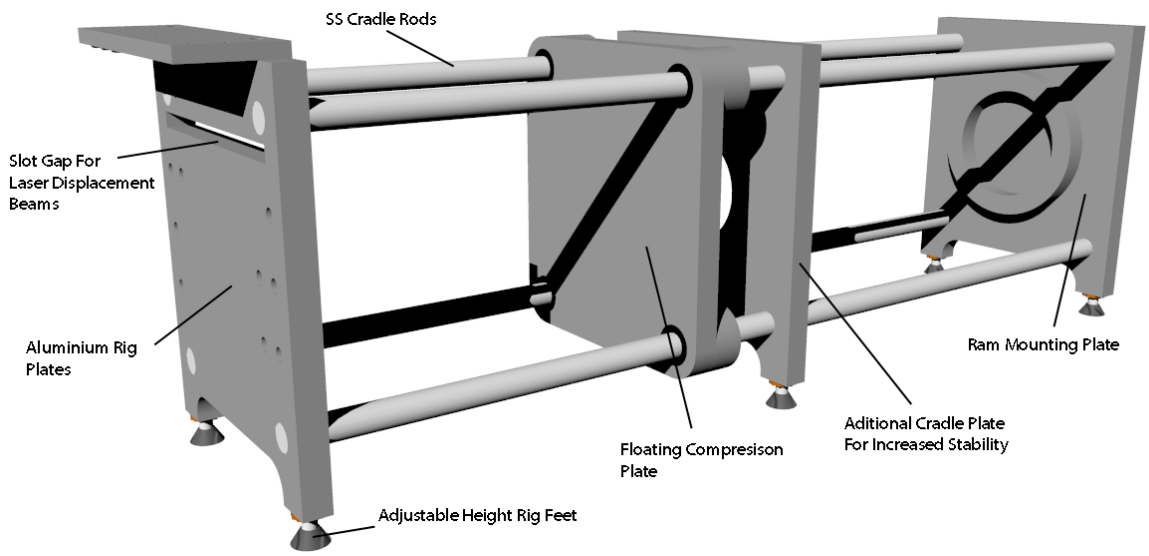

Figure 30: Stack cradle design

The method of inclusion of the fuel cell stack to the rig design is perhaps most important in producing a robust test rig. Figure 31 depicts the insulation and current collecting mounting blocks for the fuel cell stack. The insulating planes are designed to use a high-strength engineering plastic, which has a high electrical resistance, the current collecting blocks are designed to use the same material as with a single cell compression rig of gold and silver plated oxygen free copper. All the seals between mating surfaces are designed to be standard size Viton O-rings. The most important part of the mounting assembly are the PTFE mounting guides, these guides fit throughout the whole stack enabling low friction movement of each component.

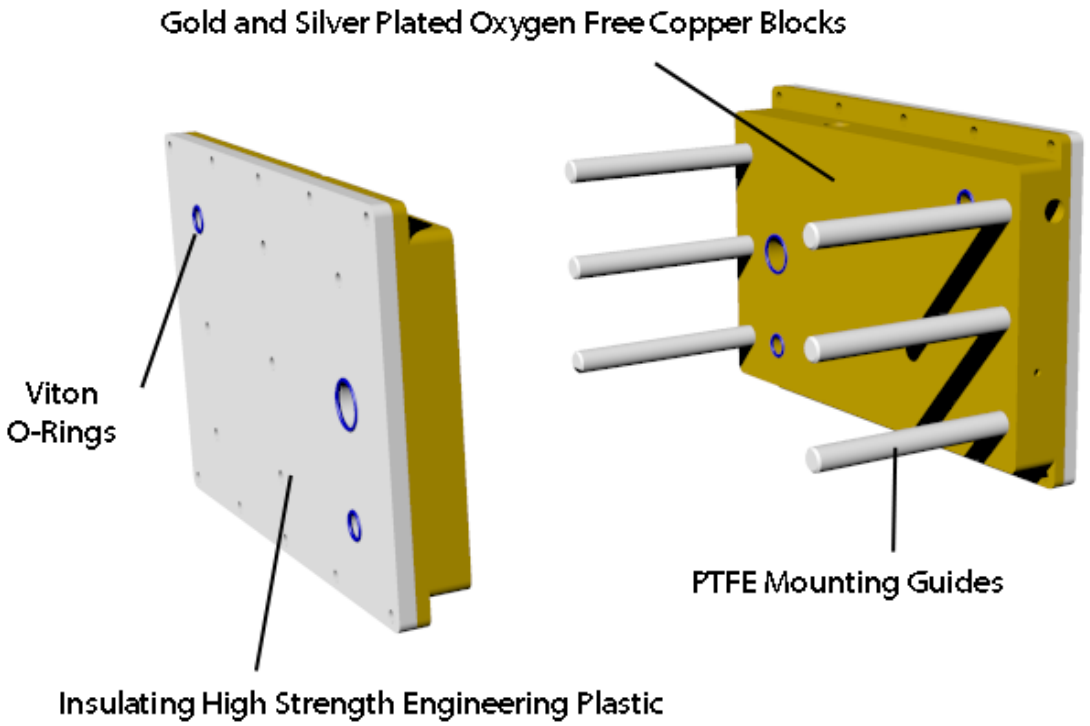

Figure 31: Mounting components for stack compression rig.

Incorporated into the design of the flow field plates are tabs on the top surface (see Figure 32), these tabs in combination with the positioning rods enable the laser displacement system to take differential measurements between each plate. The tabs are arranged on top of the flow field plates in the form of two separate systems, this allows the laser displacement system to take binocular measurements of displacement change. Due to the laser operating in a fixed plane this allows twisting movement of the MEAs to also be measured. The position of the laser displacement system is controlled using a servo actuated linear positioning system, which provides sub micron levels of positioning accuracy. The key advantage to this later system is that it offers a high level of resolution (0.4 μm) and enables both total system and individual MEA changes to be measured during the operation of the stack.

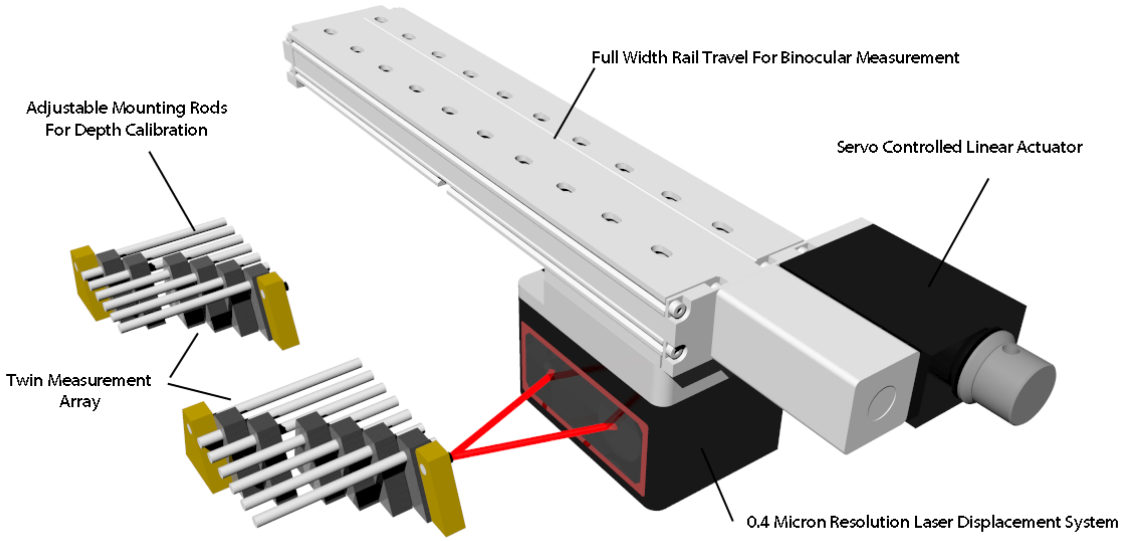

Figure 32: Laser displacement measurement system with laser resolution of 0.4 µm and servo controlled positioning of the laser to an accuracy of 0.2 µm.

Results

3. *In-situ* GDL characterisation

This chapter looks into the behaviour of the GDL material when it is placed in a fuel cell. Pure samples of material are placed in the cell, compression is varied and the mechanical response (displacement change) and electrical response (bulk and contact resistance) are observed. This technique is then applied to various materials in order to produce comparison data for commercially available GDLs, this is important as it can inform selection of a material. The cyclic response of the GDL to compression is then investigated to get an insight into the long-term degradation that multiple cycles may cause. For the overall study it is important to begin with establishing the compression response of the GDL to fully understand the relationship of compression to fuel cell behaviour (mechanical change) and performance of the system first needs to be broken down into it constituent parts.

The results presented in this section feature the pure material responses after removal of the system response from the recovered data. The system compression response in terms of displacement is approximately linear with a gradient equal to 14.5 μm MPa^{-1} (see Figure 70).

3.1. Compression Cycle

The compression cycle response of a sample of Toray H120 GDL can be seen in Figure 33. The response indicates that after one cycle of compression to a maximum value of 2.5 MPa the GDL material exhibits irreversible compression resulting in a deficit between the initial displacement value and the value after the cycle that is

~50% of the total displacement change. A similar lack of reversibility is shown in the resistance, resulting in a net reduction of 5.6 mΩ cm^2.

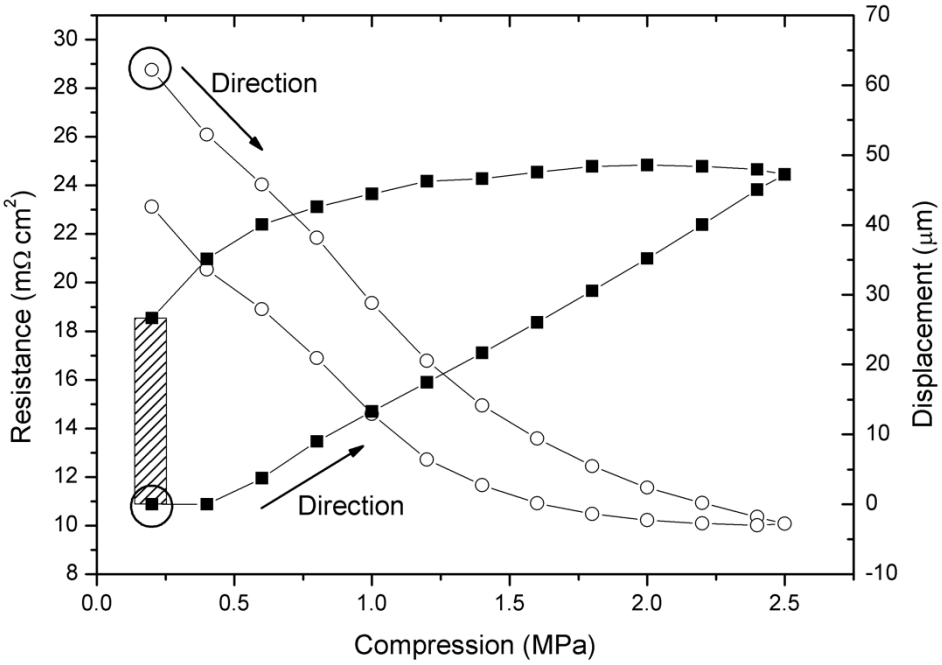

Figure 33: The first compression cycle after initial loading of the GDL sample to 2.5 MPa and back to minimum compression of 0.2 MPa. Trends show the displacement (■) and resistance (○) relationship to compression for a sample of Toray H120, with the shaded area representing the extent of irreversible compression. The initial linear response for the displacement has a gradient of 24.0 μm MPa^{-1}.

Figure 34 shows an SEM image of the GDL sample, the compressed (land) and uncompressed (channel) are clearly distinguishable. Figure 34(b) shows a close up of the land area where it can be observed that the carbon fibres are broken and compacted. This not only reduces the porosity of the material but also increases internal fibre connections, which may account for the lower resistance after the initial cycle. This can be compared to the open channel parts (Figure 34(c)) where no compression has occurred.

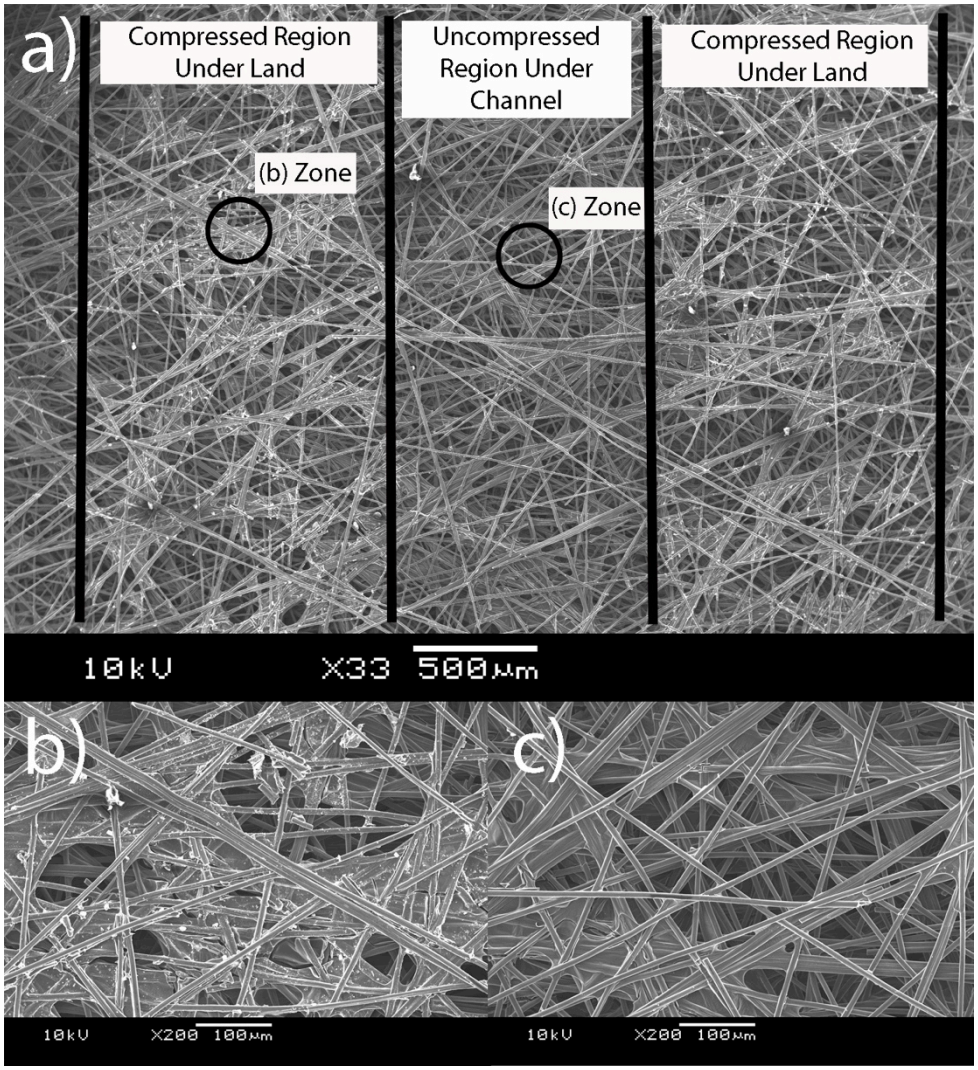

Figure 34: SEM images of un-teflonated Toray paper showing: (a) the impression of the flow-field land made upon compression to 2.5 MPa with the black vertical lines as a visual aid, (b) a close up of the compressed zone under the land area showing broken fibres and (c) showing the uncompressed region from under the flow channel.

Figure 35 shows the effect of extreme compression up to many times operating compression of 12.5 MPa, this exaggerated compression illustrates the crushing

problem. Part (a) shows the imprint made by the land; part (b) shows a close-up of the crushed zone with many short (broken), well compacted fibres.

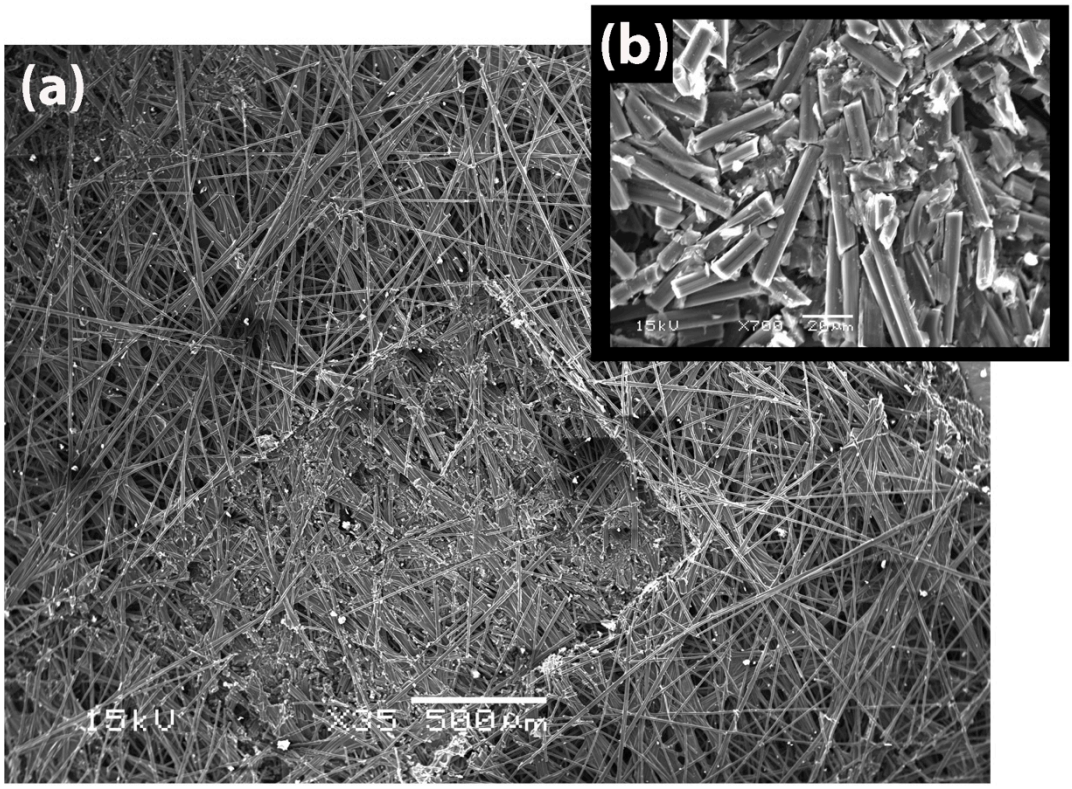

Figure 35: SEM images of un-teflonated Toray paper showing: (a) the impression of the flow-field land made upon compression to 12.5 MPa, and (b) a close-up of the compressed zone under the land area showing broken fibres.

While the unteflonated GDL compression results are interesting it is more common for GDL materials to contain PTFE as a way of creating the desired hydrophobic/hydrophilic balance to promote effective water management. Figure 36 shows as SEM image of a compressed region of Toray H-series GDL material that was taken from an MEA that was operating with typical performance that had been compressed to 2.5 MPa.

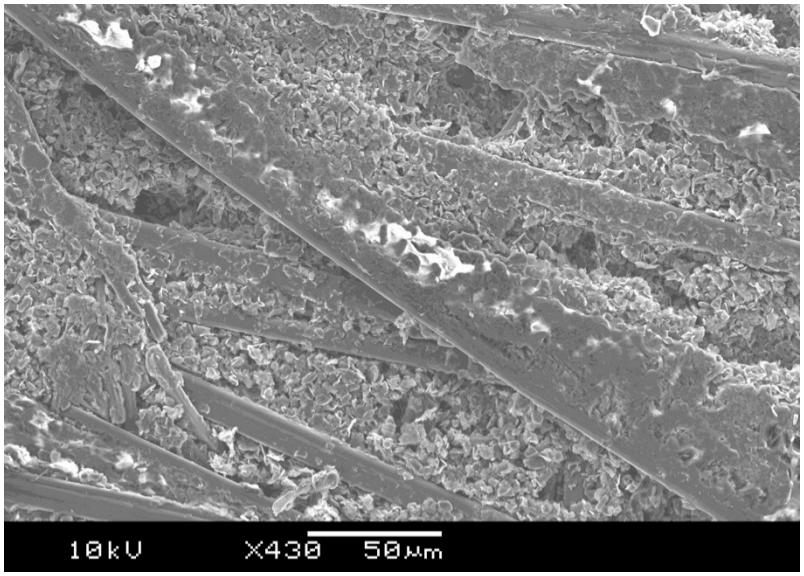

Figure 36: SEM image of a compressed section of Toray H-series GDL material taken from an MEA that was operating with typical performance that had been compressed to 2.5 MPa.

Figure 37 shows the make-up of the material by highlighting responses that show carbon (red) and fluorine (green). The test was conducted over the same area as the sample in Figure 36. What is particularly interesting about this compressed sample (from under the land) was that the sample clearly shows that there is very little porosity at the surface (especially when compared to images of the uncompressed region of the same material, Figure 38). A relatively high proportion of the image shows the presence of fluorine, which provides the handle for assessing the distribution of PTFE in the structure. With PTFE being highly non-conductive it is interesting that the surface has such a large quantity of it near or on the visible surface. As such one would expect that increasing compression would not improve the contact resistance (due to the PTFE presence at the interface) however this is not the case as discussed in this section.

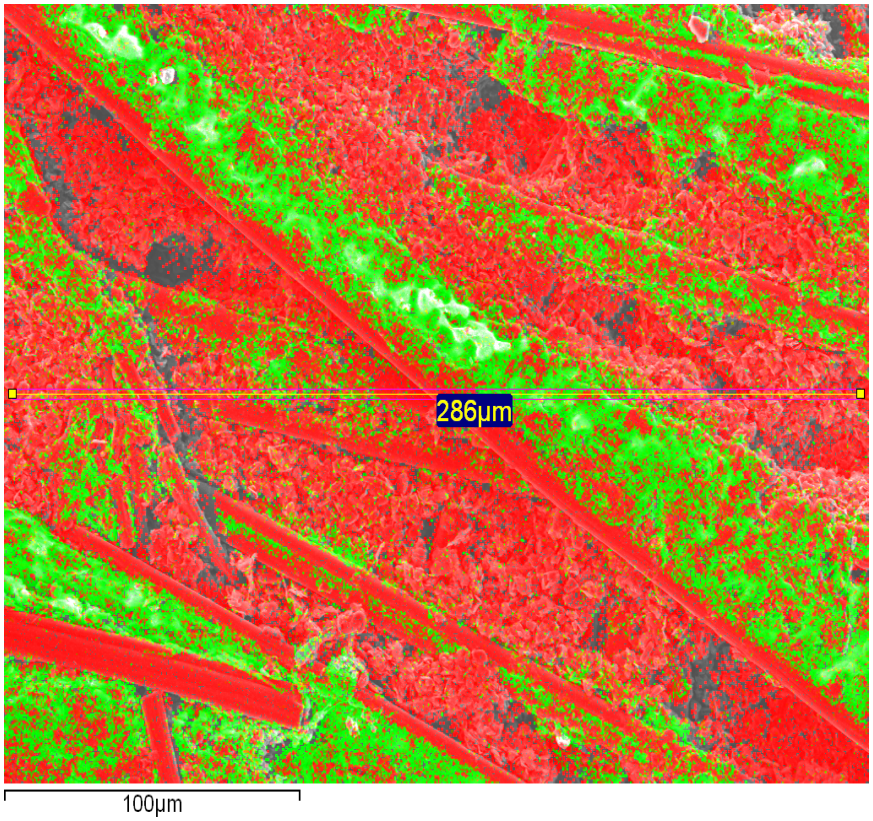

Figure 37: Image of the sample from Figure 36 taken using EDS showing the distribution of carbon (red) and fluorine (PTFE, green).

Figure 38 and Figure 39 show the SEM image and EDS spectrums of the uncompressed region of the GDL that is seen in Figure 36. The image shows a clear difference in the material properties when compared to the compressed region with a noticeable increase in the porosity at the surface. A decrease in porosity is expected from the irreversible compression that is implied in Figure 33.

Figure 39 shows the EDS spectra from the points in Figure 38, in the spectra the fluorine peak (labelled 'F') is an indicator of the PTFE presence and the carbon peak (labelled 'C'). As was shown in the compressed region, the PTFE content is distributed along the carbon fibres with the indication from the image that the hydrophobic regions of the material appear to line the visible pores in the structure.

The strong fluorine peak from spectra 1 shows that the PTFE in the image is indicated by the white responses in the SEM image, spectra 2 is taken from the material that is lining the carbon strands and shows a fluorine peak, spectra 3 is directed purely at the carbon fibre and as such shows no fluorine responses as expected. Spectra 4 is taken from a region of the material that is neither fibrous carbon nor PTFE (no fluorine response) but is a carbon by-product from the manufacturing processes.

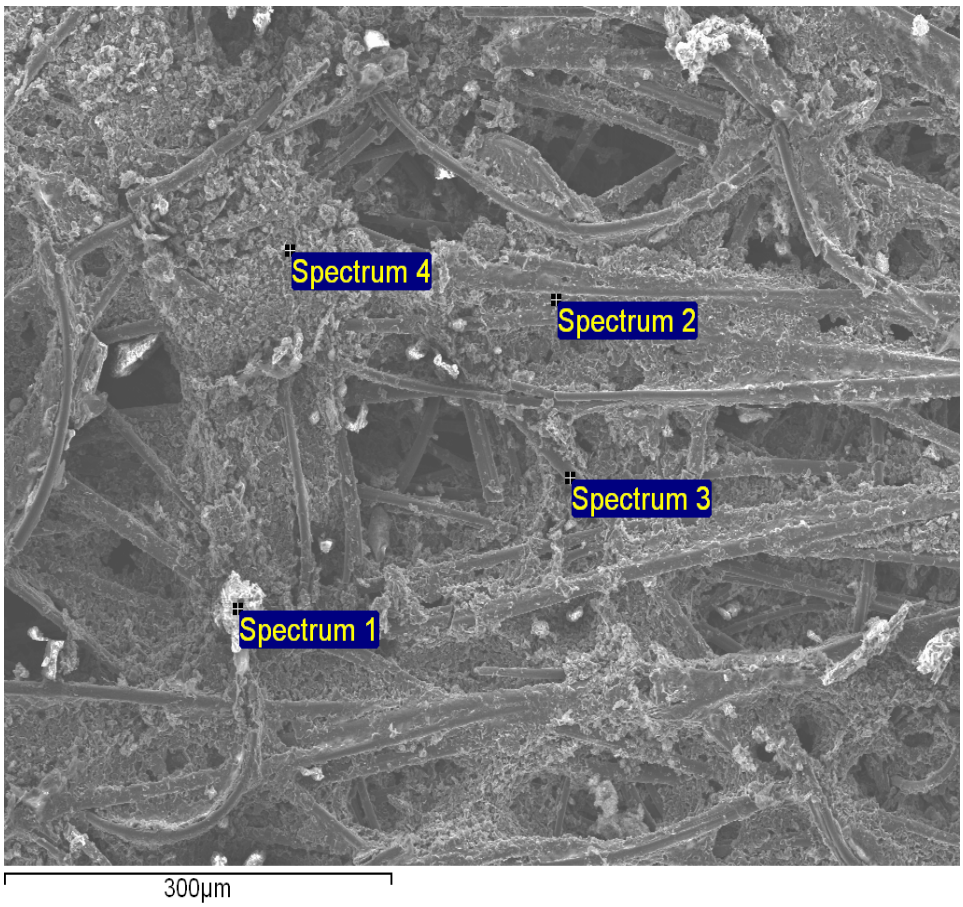

Figure 38: SEM image of the corresponding uncompressed region of the same sample as seen in Figure 36, Labelled on the diagram are the points at which the EDS scans were taken to analyse the materials present that can be seen in Figure 39.

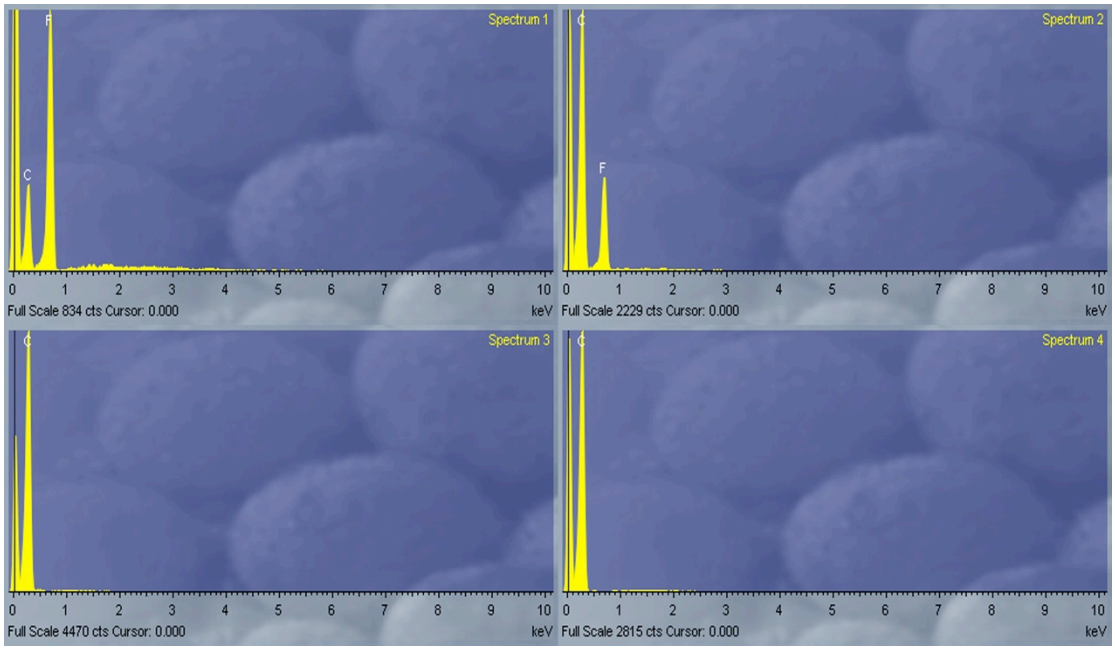

Figure 39: EDS spectra for the sampling points from Figure 38.

3.2. Compression Reversibility

To examine reversibility of the compression effects, the CCU was programmed to return back to a minimum operating pressure of 0.2 MPa after each compression step. This enables the displacement and resistance response to be obtained before and after each compression step and thus determine the extent of irreversible compression. The compression reversibility characteristics are shown in Figure 40 to Figure 42.

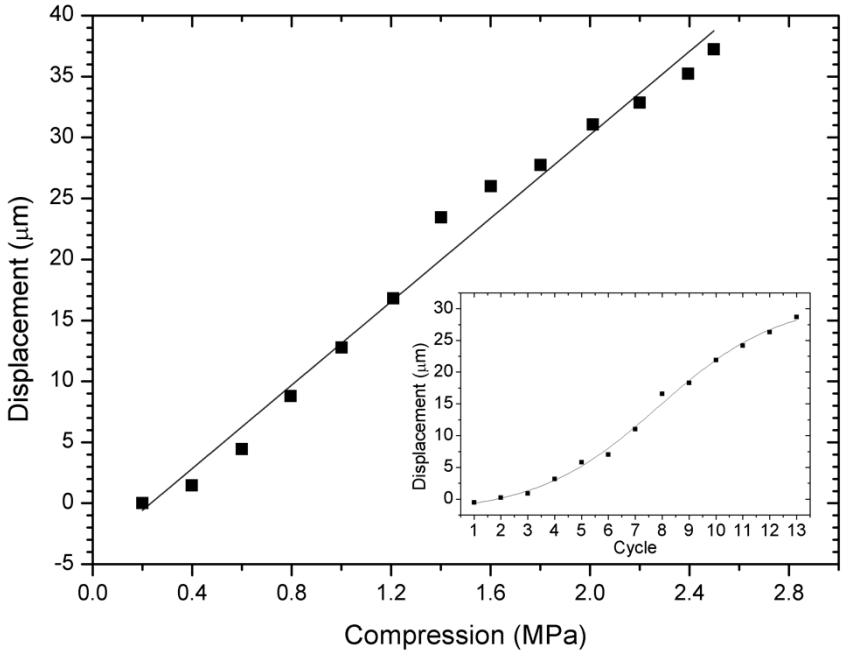

Figure 40: Trend observed for Toray H120 displacement when compression is returned to 0.2 MPa between each step of increased compression on a single GDL sample. Inset: Irreversible displacement with increasing compression step as in the main figure (reduction of the thickness of the sample after each cycle, points are at 0.2 MPa).

It can be observed in Figure 40 that the displacement of the sample increases in an approximately linear fashion in a similar way to that in Figure 33. However, the gradient is lower at 17.1 μm MPa^{-1} compared to 24.0 μm MPa^{-1} for the monotonic increase in pressure without returning to minimum compression. This is considered to be due to the limited displacement reversibility of the GDL, which means that cycling between compressed and relaxed states leads to less net compression of the component. This may have useful practical consequences when formulating cell compression protocols.

The level of irreversible compaction is shown in the graph inset in Figure 40. The first few cycles show that the GDL has only a slight (few microns) net compression effect. The degree of irreversibility increases with cycling and the extent of compression.

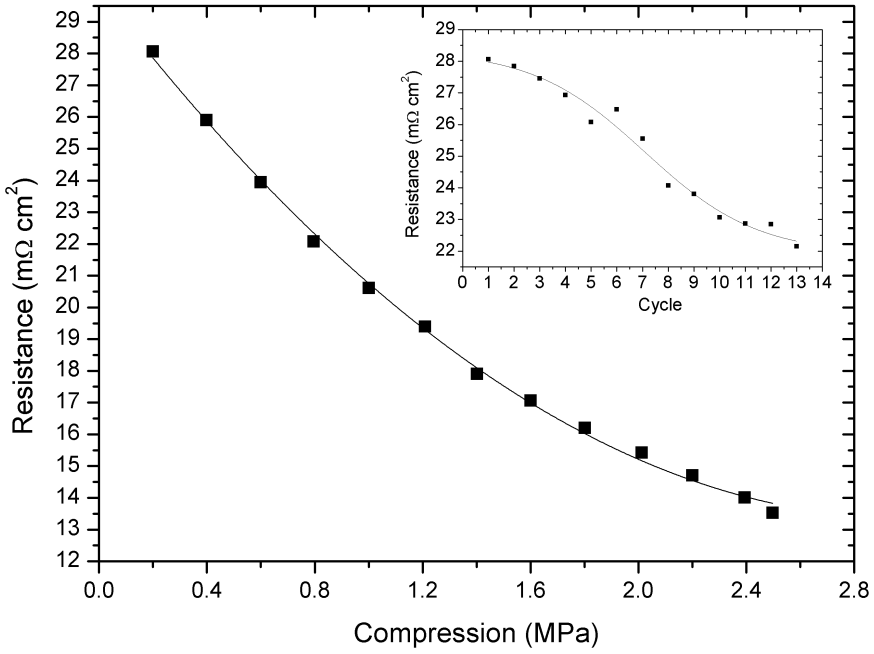

Figure 41: Corresponding trend for Toray H120 the resistance response to the data in Figure 40. Inset: Values for the resistance at 0.2 MPa after each cycle of compression.

For the resistance (Figure 41), a similar non-linear profile is observed to that of Figure 33. The relaxed state (0.2 MPa, inset in Figure 41) shows a net decrease in resistance with cycling. This may be due to improved contact between the GDL by virtue of the compacted broken fibres under the lands or tenting in the channels (intrusion of the fibres into the channels leading to new contacts between the GDL and the inner walls of the channels).

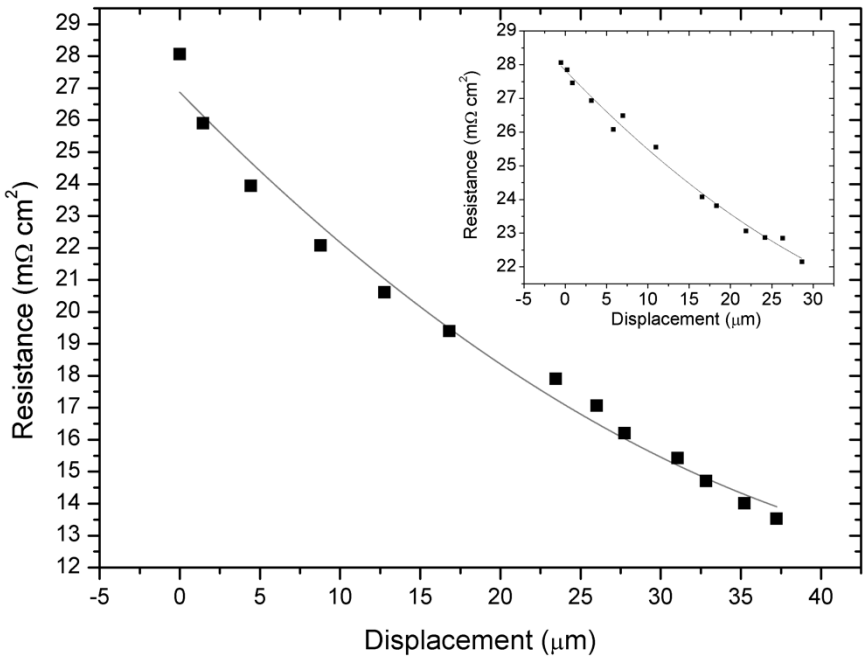

Figure 42: Relationship between displacement and resistance response of Toray H120 from Figure 40 and Figure 41. Inset: Trend for values obtained at 0.2 MPa.

Figure 42 shows the relationship between resistance and displacement of Toray H120 over a range of compression from 0.2 to 2.5 MPa. The figure inset shows the same relationship but all points are at 0.2 MPa. Figure 42 demonstrates that while the resistance decreases at a near constant rate in relation to displacement, the rate of decrease of resistance reduces as the displacement increases.

3.3. Comparison of various GDL materials

Figure 43 shows the effect of compression force on the dimensional change and resistance of a range of commercially available GDL materials. During the initial phase of compression there is an engagement feature that can be seen in both the

displacement and resistance traces for each of the GDL materials. The engagement feature does not appear to be dependent upon the type of the GDL due to difference in the trends observed by the two thicknesses of Toray material. This feature can be attributed to the initial interaction of the surfaces of the FFP and the fibres of the GDL.

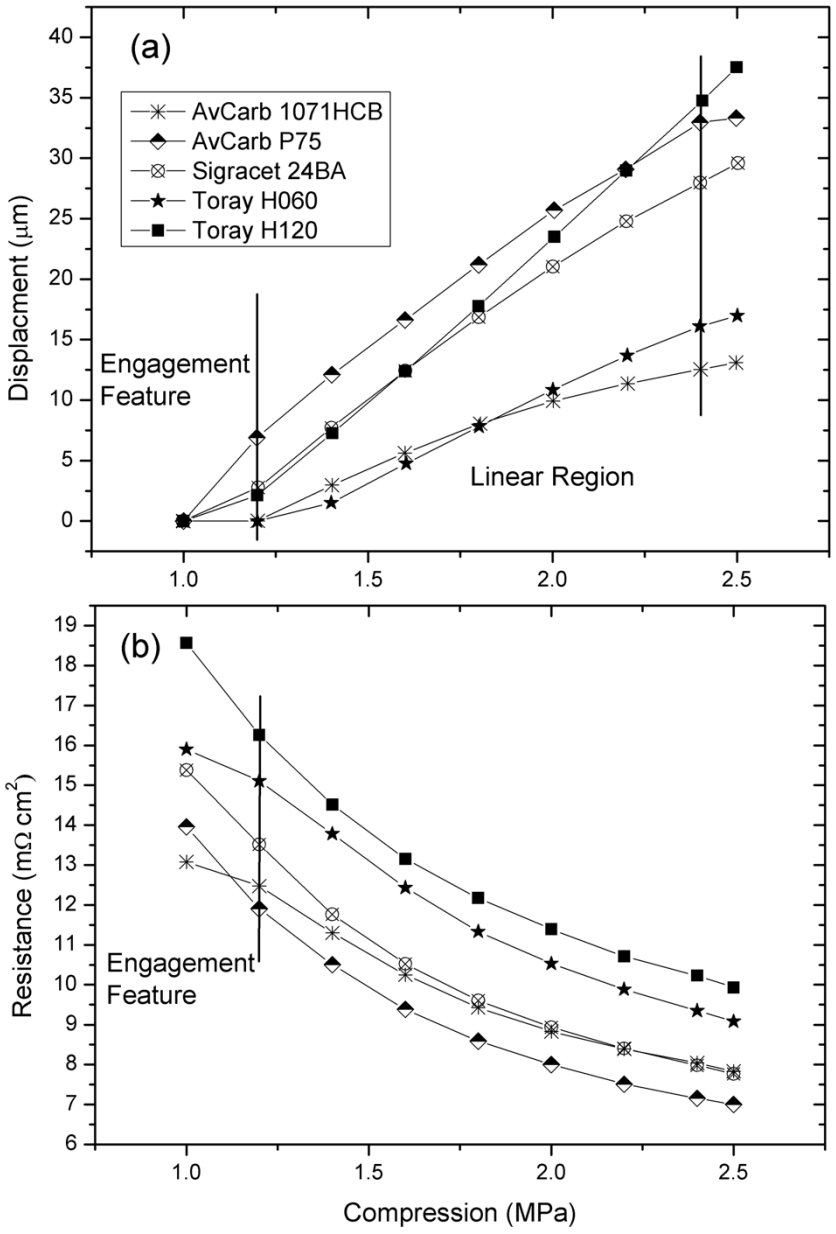

Figure 43: (a) displacement response comparison graph for various GDL materials tested *in-situ* from 1 to 2.5 MPa compression; (b) corresponding resistance response.

Table 9: Comparison table of the rate of change of displacement with compression for various GDL materials from the linear region of Figure 43(a).

GDL Material	Material Type	Thickness (μm)	Through-plane Resistivity from manufacturer data (mΩ cm^2)	Measured Resistance @ 1.5 MPa (mΩ cm^2)	Displacement Factor (μm MPa^{-1})	Relative Displacement Factor (μm MPa^{-1} μm^{-1})
AVCarb 1071HCB	Cloth	220	7.7	7.70	9.6	0.043
AvCarb P75	Paper	200	7.4	7.11	20.9	0.104
Sigracet 24BA	Paper	200	<10.0	7.98	20.3	0.101
Toray H060	Paper	190	1.9*	9.42	14.6	0.077
Toray H120	Paper	370	3.0*	9.96	27.4	0.074

* mΩ (not area specific)

Table 9 shows manufacturer data for GDL materials and results from this study. Note that the total resistance is composed mainly of the contact resistance; hence, thickness has a small effect on the total resistance (cf. Toray H060 and H120). The 'displacement factor' describes the change in dimensional thickness with compression force, i.e. the gradient of the linear section for each GDL material from Figure 43(a). This represents a convenient metric for comparing the mechanical properties of different GDL materials. Of the materials that are of comparable thickness (190 to 200 μm) and construction (paper type) the Toray H060 exhibits the lowest displacement factor; however, there is a range of values for materials in this category. The carbon cloth, AvCarb 1071HCB, has the lowest displacement factor and therefore most resistant to dimensional change with compression. The 'relative displacement factor' (MPa^{-1}) shows the displacement factor normalized for thickness; i.e., change in thickness with pressure divided by initial thickness (μm MPa^{-1} μm^{-1}). This factor

shows that the Toray materials have a similar response as expected due to the bulk of the material being the same.

From Figure 43(a), the displacement trend includes a large linear region from 1.2 to 2.4 MPa. This linear region is important as it represents the range over which fuel cells commonly operate (Table 4) and as such shows how the GDL material reacts to changes in compression during operation. It is apparent from analysis of the linear fits of this region, Table 9, that the type of material is important in determining the response of the GDL to compressive force.

The linear trend for the displacement graph contrasts with a curved profile for the resistance response, shown in Figure 43(b). Each of the materials start from a different initial resistance and then decrease with increasing pressure, following very similar profiles for each of the paper-based GDLs. The carbon cloth exhibits a shallower response, the resistance decreasing at a slower rate with increasing pressure than the paper type GDLs. Note that although the paper type materials are generically similar, the fabrication methods vary and the structures can be quite different [48].

These results imply that there is an 'intrinsic' resistance associated with each GDL material manifest under minimum compressive force. The change in resistance is a function of the class of material (paper or cloth). The difference between the initial resistances of the two Toray papers (each made of the same material) is attributed to the difference in thickness.

3.4. Resistance and displacement relationship

The relationship between the displacement and resistance response gives additional insight into the way the GDL responds in a fuel cell environment, as shown in Figure 44. Initially, the resistance increases with a relatively small decrease in displacement; however, this is non-linear and a progressively greater displacement is associated with resistance drop. Figure 44 compares Toray H060 and AVCarb 1071HCB with extremes of performance (see Figure 43). However, with the exception of the initial resistance, each follows a very similar profile of dimensional and resistance change.

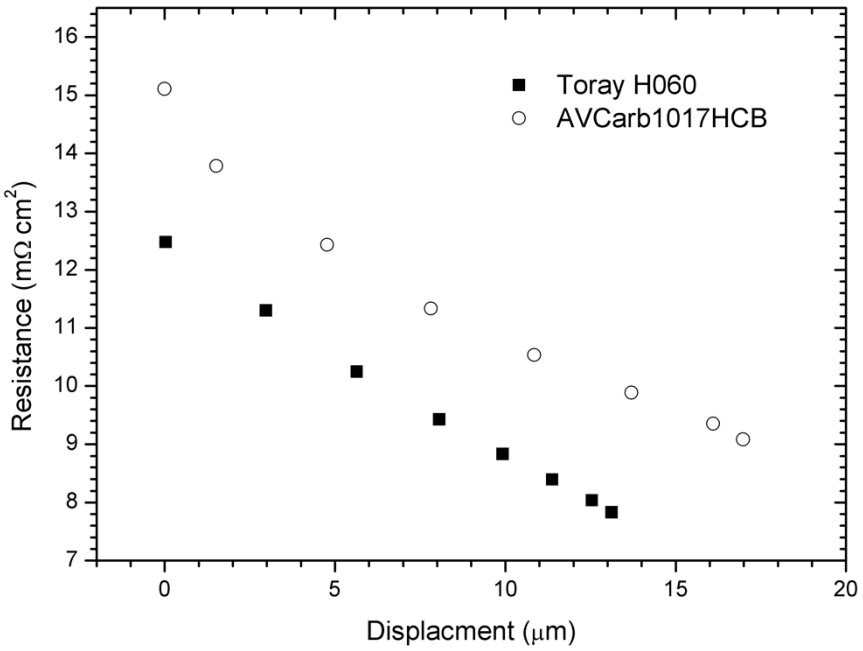

Figure 44: Relationship between the resistance response and the displacement for Toray H060 and AVCarb 1071HCB GDL. This figure shows the response over the compression range between 0.2 and 2.5 MPa. The compression was not returned to the minimum in-between each point.

3.5. Cyclic behaviour

The durability of GDL materials is improtant as they have to operate for many thousands of hours in practical applications. During operation there are several factors that may cause dimensional change in a fuel cell. Thermal cycling, antagonised by components with different thermal expansion coefficients (i.e., BPP materials, metallic backing plates or end plates or the cell tie rods) and hydration cycling of the electrolyte and GDL, can all impose mechanical stresses and consequent strain in PEFC stacks.

Figure 45 shows the multiple cycle profile for a GDL (Toray H120) sample. The displacement response from Figure 45(a) shows and initial straight line trend followed by the secondary curved trend that is repeatable and does not vary significantly when compression is increasing or decreasing. The resistance trend in Figure 45(b) shows that the difference between initial and secondary trend of the displacement response is not repeated for resistance, it also shows that the trend is repeatable after a number of compression cycles.

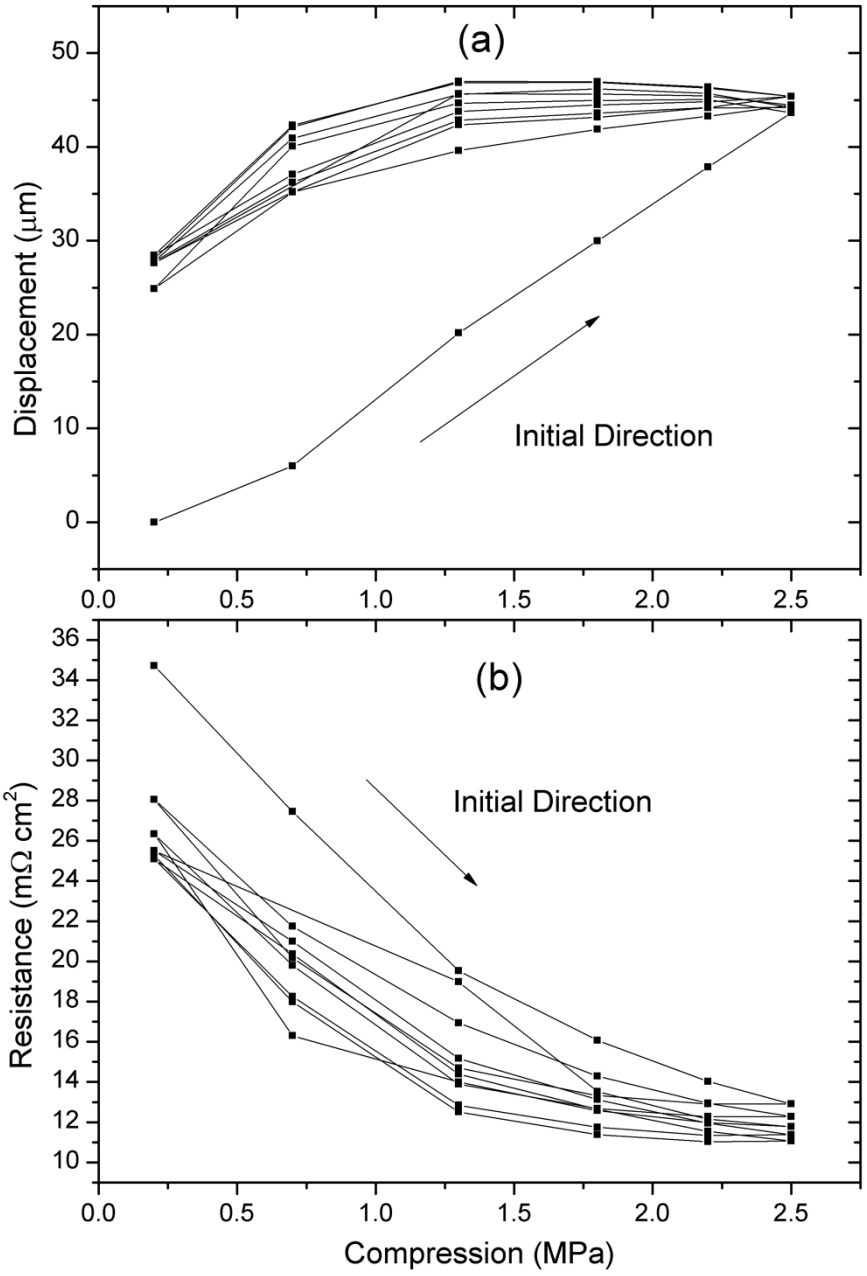

Figure 45: (a) depicts the multiple compression cycling effect on the thickness of a Toray H120 GDL with (b) showing the sample resistance response.

Figure 46 shows the maximum and minimum of the displacement and the resistance response respectively for each cycle of compression. Each response shows a trend towards a plateau in the data at approximately nine cycles of compression from 0.2 to 2.5 MPa. This suggests that the relaxation of the GDL material due to the

compression occurs after a relatively low number of cycles. The displacement figure rises 3.5% from the initial maximum, suggesting a small reduction in thickness and therefore porosity of the material. The resistance response at maximum compression corresponds to a ~20% reduction in ohmic resistance of the GDL material over the number of cycles measured. The resistance data was fitted to a first order exponential decay equation resulting in the trend line in the figure. A decay process of this type may be expected if the material stabilises after a certain level of irreversible compression.

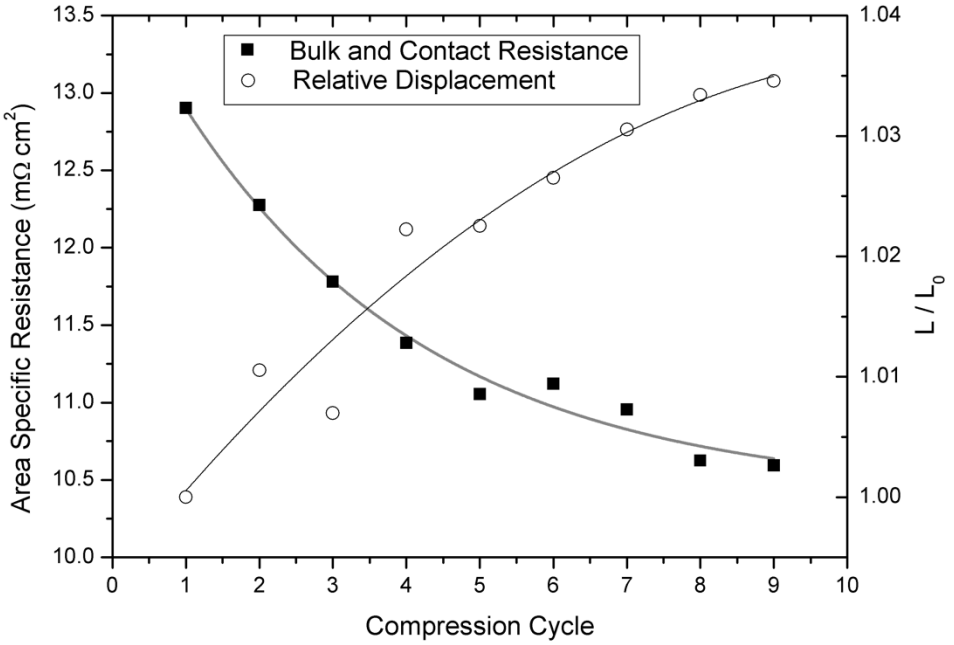

Figure 46: Graph depicting the multiple cycling effects on Toray H120 after cycling of compression from 0.2 to 2.5 MPa. The measurements are each taken after stabilization at maximum compression for each cycle. The displacement trend shows the material compresses 103.5% of the original maximum displacement and the resistance response tends towards a plateau at ~10.5 mΩ cm^2.

3.6. Conclusions

The results in this section show that hard-won millivolts of performance, brought about by catalyst and membrane advances, can be lost through poor choice of GDL material or compression engineering (e.g. for operation at 1 A cm^{-2}, every mΩ dropped in the GDL equates to a mV less of voltage loss). Increasing compaction pressure leads to a decrease in resistance; however, this relationship is non-linear and there are diminishing returns on resistance decrease when increasing compacting force that can lead to deleterious effects such as GDL damage, loss of porosity and tenting.

For Toray paper, compaction becomes more irreversible with compression pressure – at low compression there is only slight net reduction in GDL thickness but there is no evidence that an 'elastic' region exists. It was found that different GDLs have an intrinsic resistance that is a function of their thickness and material / structural composition. Subsequent increase in compaction pressure leads to a very similar reduction in total resistance that is common to all of the paper type GDLs.

The GDL is the most compliant component in the fuel cell assembly. Understanding how it deforms under pressure is vital for understanding how to put cells and stacks into compression. Over the full range of compression force studied, the relationship between changes in resistance and GDL displacement are very similar for all GDL types.

Cyclic compression of Toray GDL leads to progressive improvement in resistance and reduction in thickness that stabilises after ~10 cycles.

4. *Ex-situ* GDL characterisation

Ex-situ GDL analysis is by far the most common way to analyse material whether that be using an imaging technique or building a specific test rig to look at a particular property of the material (gas permeability for example). The purpose of this chapter is to perform consistent tests on a large range of commercially available GDL materials in order to produce data enabling the comparison of material properties. In this section imaging techniques (SEM) are used to visualise the difference in structure of various materials to give insight into the difference in values obtained. A comprehensive comparison table is then produced as reference for the variety of values obtained from experimental analysis of each material. The porosity values are then used to assess how the range of values affects the theoretical calculation of limiting current, which helps to link this work directly to fuel cell performance. This section of the study is important as it compliments the *in-situ* study (Section 3) to produce a comprehensive analysis of commercially available GDL material properties.

This work was carried out in collaboration with Ahmad El-kharouf and Prof. Bruno Pollet of Birmingham University.

4.1. GDL structure

Of the many types of GDL that are commercially available, two fundamental types are produced, that of woven cloth type GDLs and the non-woven paper type materials. The non-woven materials can be further sub-divided into a straight fibre

group and a ‘spaghetti like’ felt group. Figure 47 depicts the most common structures available, namely that of (a) cloth types, (b) paper type and (c) felt type.

Commercial woven cloth type GDLs are available but due to the relatively high cost of manufacturing compared to the non-woven paper GDLs and the surface not being flat they tend not to be used. Table 10 shows the main difference between the woven type GDLs, notably the weave width and fibre diameters from SEM image measurements. Figure 48 shows an SEM comparison of the visual variation of woven GDL types across the various manufacturers. The SEM image for LT1200W in Figure 48 (c) shows the PTFE loading on the cloth type material. Here, the woven structure gives the GDLs high mechanical flexibility and compressibility. Table 11 depicts the measured values from this study (all *ex-situ* measured values) alongside manufacturer data.

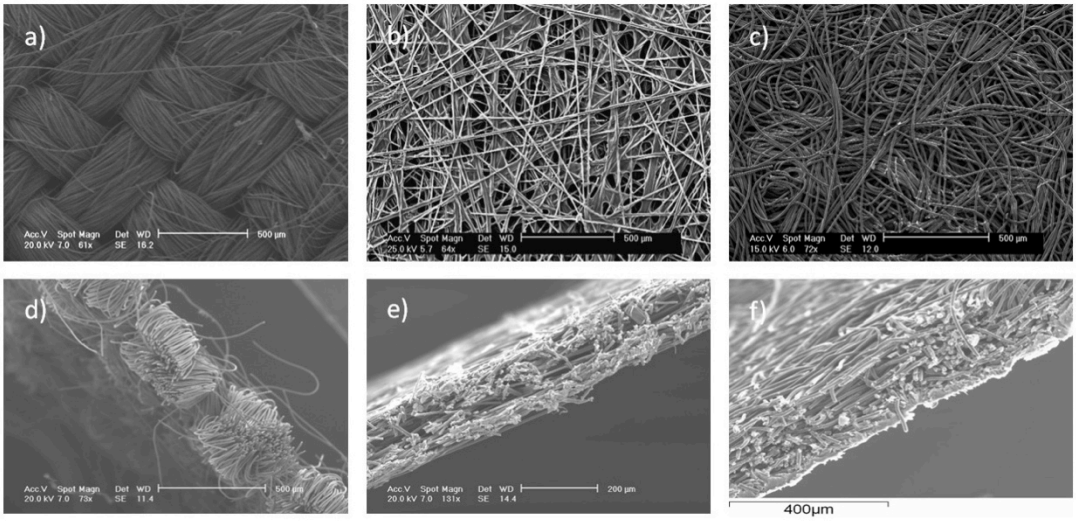

Figure 47: SEM images taken of the various types of GDL structure that are commercially available. Images (a) and (d) show the cloth type woven fibres, (b) and (e) show the paper types fibres and (c) and (f) show the felt type GDL material.

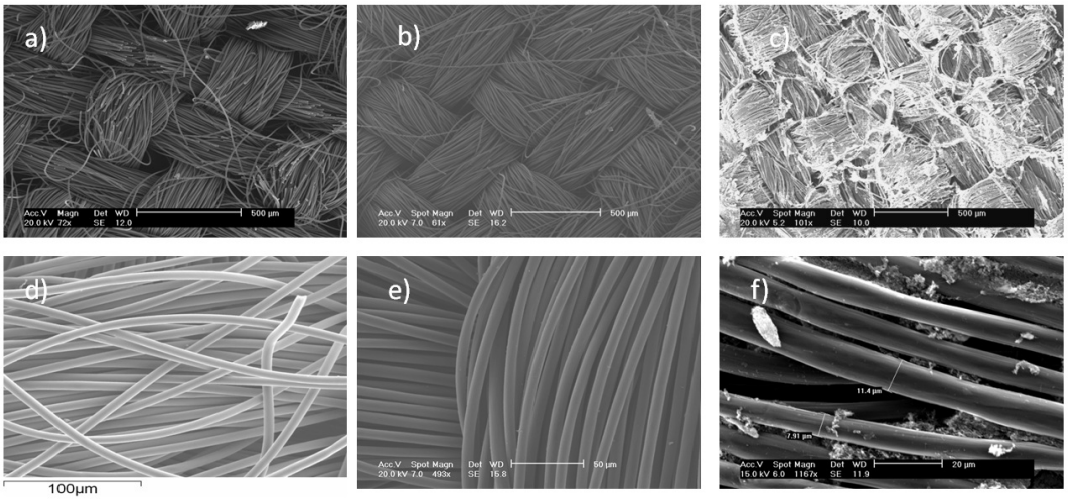

Figure 48: SEM images of several type of woven carbon cloth samples; surface views and close ups of: Tenax (a and d), Ballard 1071HCB (b and e) and ETEK 1200W (c and f).

Table 10: Woven GDL weave width and fibre details

Material	Weave width (µm)	Fibre diameter (µm)
1071HCB	350 – 500	8 – 9
TCC2260	200 – 250	8 – 9
TCC3250	250 – 375	11 – 12
LT1200W	450 – 500	8 – 11

Table 11: Commercial GDL properties [48]

Materials	Manufacturer materials' properties			*Ex-situ* measured properties					
	Thickness (µm)	**Area weight (g/m^2)**	**Bulk density (g/cm^3)**	**Real density (g/cm^3)**	**Bulk density (g/cm^3)**	**Porosity %**	**Tortuosity**	**Mean pore diameter (nm)**	**Permeability (m^2) (mercury)**
1071HCB	356	123	0.35	1.816± 0.002	0.39	64.9	1.95	3401	2.36E-11
P50	170	50	0.32	2.083 ±0.004	0.36	48.7	3.01	993	9.21E-12
P50T	180	62	0.34	2.151 ±0.004	0.37	44.9	2.55	1528	1.41E-11
GDS1120	210	79	0.40	2.125± 0.005	0.46	44.8	3.24	859	4.73E-12
P75	230	75	0.33	2.083± 0.005	0.35	62.4	2.43	2074	1.11E-11
P75T	255	88	0.33	2.087± 0.003	0.36	59.9	2.23	1227	1.31E-11
GDS2120	260	101	0.40	2.131 ±0.005	0.40	60.2	2.62	2998	6.06E-12
TGP-H-030	110	-	0.40	2.071 ±0.001	0.37	64.6	2.50	2625	1.07E-11
TGP-H-060	190	-	0.44	2.002 ±0.003	0.43	63.1	2.76	2631	6.15E-12
TGP-H-090	280	-	0.44	2.019 ±0.003	0.49	67.2	2.55	3324	4.53E-12
TGP-H-120	370	-	0.45	1.985 ±0.004	0.49	61.8	2.51	1717	3.90E-12
C2	250	130	-	1.882 ±0.002	0.57	49.2	4.51	658	9.12E-13
C4	250	130	-	1.900 ±0.002	0.49	61.0	4.26	158	1.04E-12
I2 C6	250	135	-	1.867 ±0.002	0.54	46.2	5.02	1148	8.57E-13
I2 C8	230	135	-	1.934 ±0.002	0.62	47.0	4.91	682	6.25E-13
LT 1200 N	185	75	0.41	2.053 ±0.004	0.39	64.9	2.74	769	6.45E-12
LT 1200 W	275	200	0.73	1.906 ±0.002	0.50	31.8	2.74	1055	4.98E-12
GDL 10	420	135	-	1.945±0.008	0.36	34.6	2.95	2919	8.04E-12
GDL 24	190	54	-	2.140 ±0.010	0.28	73.9	1.40	2208	3.67E-11
GDL 24	235	100	-	2.010 ±0.003	0.44	40.0	3.00	2450	5.09E-12
GDL 25	190	40	-	1.941 ±0.002	0.21	66.2	1.45	1705	4.54E-11
GDL 25	235	86	-	2.009 ±0.007	0.34	36.5	2.92	842	5.64E-12
GDL 34	315	140	-	1.987 ±0.001	0.41	47.5	2.47	2197	8.97E-12
GDL 34	-	-	-	1.978 ±0.004	0.48	40.8	2.62	1593	6.91E-12
GDL 35	300	54	-	2.022 ±0.009	0.19	70.5	1.33	2469	5.31E-11
GDL 35	325	110	-	1.980 ±0.007	0.31	52.6	1.94	1467	1.72E-11
TCC-2660	260	80	0.31	1.793 ±0.003	0.34	66.9	1.83	2291	2.96E-11
TCC-3250	320	100	0.31	1.803 ±0.002	0.36	71.0	2.32	1631	1.74E-11

4.2. Porosity and tortuosity

Porosity, tortuosity and pore size distribution are important factors in determining gas and water transport within and through the GDL. The effective diffusion coefficient (D_{eff}) can be estimated using the measured values, which is an important GDL parameter. Furthermore, D_{eff} can then be used in the calculation to see the affect on limiting current that the observed porosities have. The tortuosity values shown in this section are based on an approximation made by the software used to calculate the values that the pores are perfect cylinders. This is clearly not a practical assumption and therefore when calculating the limiting current density D_{eff} is estimated using the porosity only approximation ($\phi^{1.5}$, see Equation 15). The tortuosity values presented are still useful for the purpose of comparison.

Figure 49 shows the wide variation in commercial GDL porosity (a) and tortuosity (b) values as measured in this study. The values for porosity, tortuosity and average pore diameter values are listed in Table 11. The table clearly shows that porosity and tortuosity are affected by the presence of PTFE and MPL. Generally speaking, PTFE loading decreases the porosity and tortuosity. The decrease in porosity is mainly due to the blockage and narrowing of the pores and the decrease in tortuosity might be due to the blockage of closed and longer pores leaving shorter open pores for permeability. Adding an MPL introduces an extra layer with lower porosity and smaller pores resulting in a decrease in the overall porosity and thus an increase in tortuosity, the values obtained from MPL added samples are therefore skewed and are less reliable than for a more homogeneous system (without MPL).

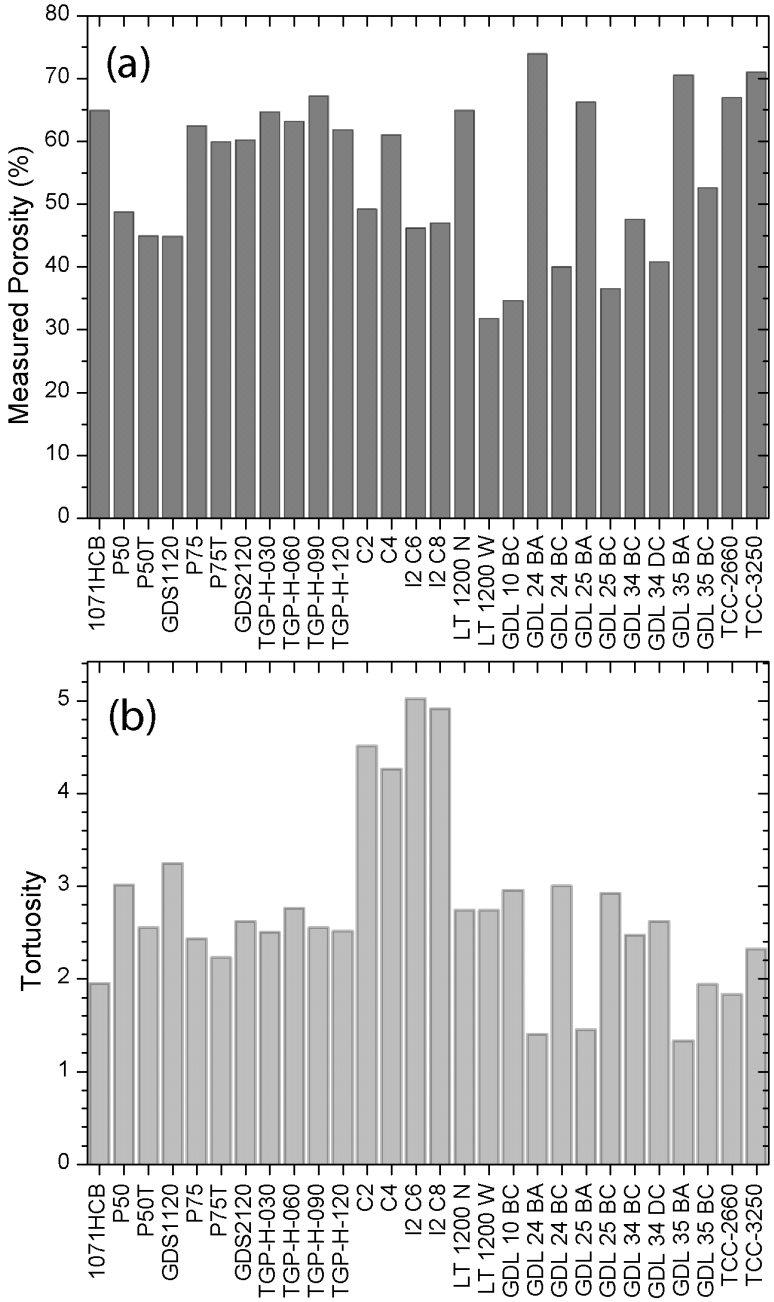

Figure 49: Plots of the range of values measured porosity (a) and tortuosity (b) for commercially available GDL materials.

The calculated limiting current for the various GDL materials based upon the measured porosity and thickness are shown in Figure 50. The values are obtained using the limiting current equation (Equation 14, for equation parameters see Table 14) for the cathode with O_2-N_2 reactant feed. The majority of the calculated values lay

within the 5-20 A cm^{-2} region which represents an unrealistically high limiting current. There is a significant limitation with this calculation, this is discussed below. As a general rule of thumb the lower the thickness the larger the limiting current and the higher the porosity the larger the limiting current.

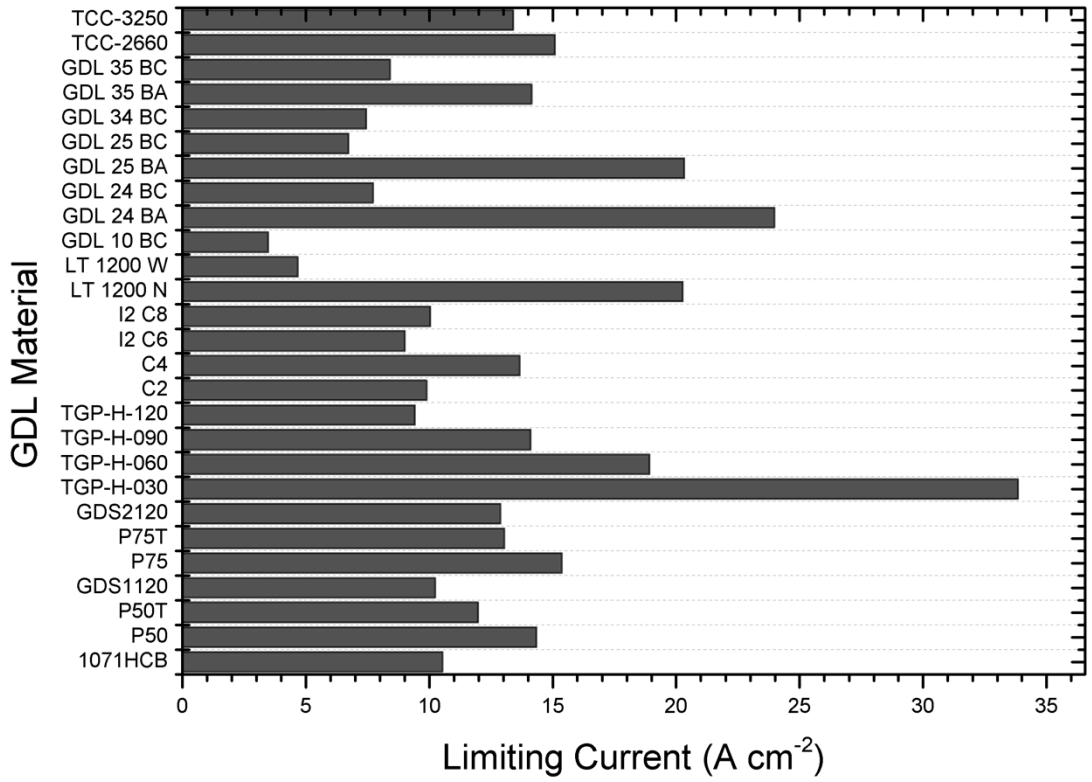

Figure 50: Calculated values of the limiting current for various GDL materials based upon using the measured porosity values to calculate effective diffusion (D_{eff}) for O_2 in N_2 then utilising Equation 14 for i_l for a system at 80 °C.

The limitations of the calculated values of limiting current density (Figure 50) lie in the assumptions made about the porosity. Due to the varied nature of construction of the GDL material (cloth vs. paper, PTFE content variation and MPL presence) the porosity value is an average across the whole thickness of the material. This is of course not realistic as the MPL inclusion, as an example, adds a dense layer to one

edge of the GDL therefore skewing the result (as porosity is the proportion of a material that is void space). Another limitation is that lack of water management term in the limiting current equation, which makes it difficult to be conclusive with the analysis. The values are useful however for comparison purpose across the range of materials.

4.3. Pore size distribution

Distribution and variation in pore sizes shown by the pore size distribution are important for their effect on the capillary pressure driving the water out of the PEM fuel cell [102]. Pore size distribution measurement is commonly determined by the coverage of the volume of mercury intrusion over the range of pore diameters in the GDL material. This section compares various materials that have varying properties (such as PTFE content) to observe the effect on pore size and distribution.

Figure 51 shows that the pore size distribution curve for the Toray paper samples show larger pores in TGP-H-030 and TGP-H-060 with lower volume intrusion for the latter. TGP-H-090 and TGP-H-120 samples show a shift to smaller pore diameters. This observation of high volume intrusion and pore size in TGP-H-030 is interesting and could be due to the small thickness of the GDL. Here, the porosity values for the Toray samples are in very good agreement with those obtained by Fishman *et al.* [103].

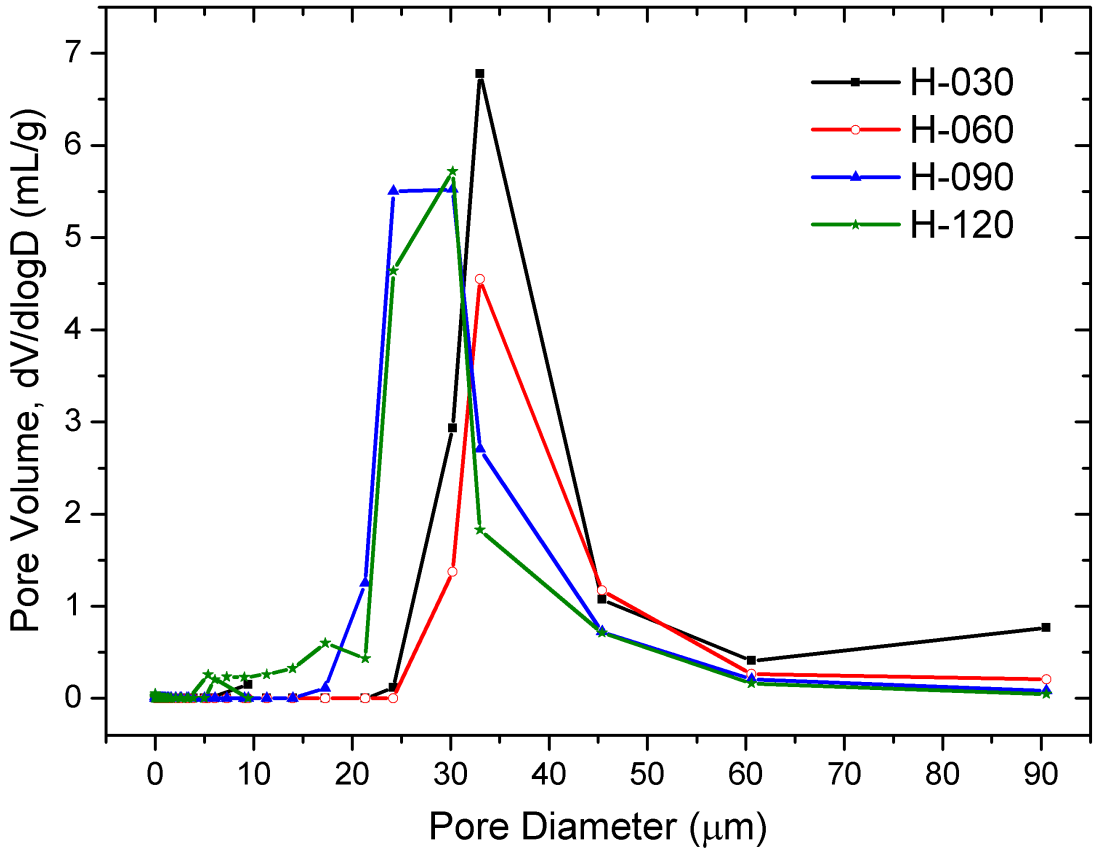

Figure 51: Pore size distribution as a function of thickness of Toray paper

With the application of a MPL on the substrate a significant change in the pore distribution is observed, as shown in Figure 52. The figure shows that the curve peak shifts to lower pore size values with less volume intrusion causing a significant decrease in the bulk porosity, as can be seen in Table 11.

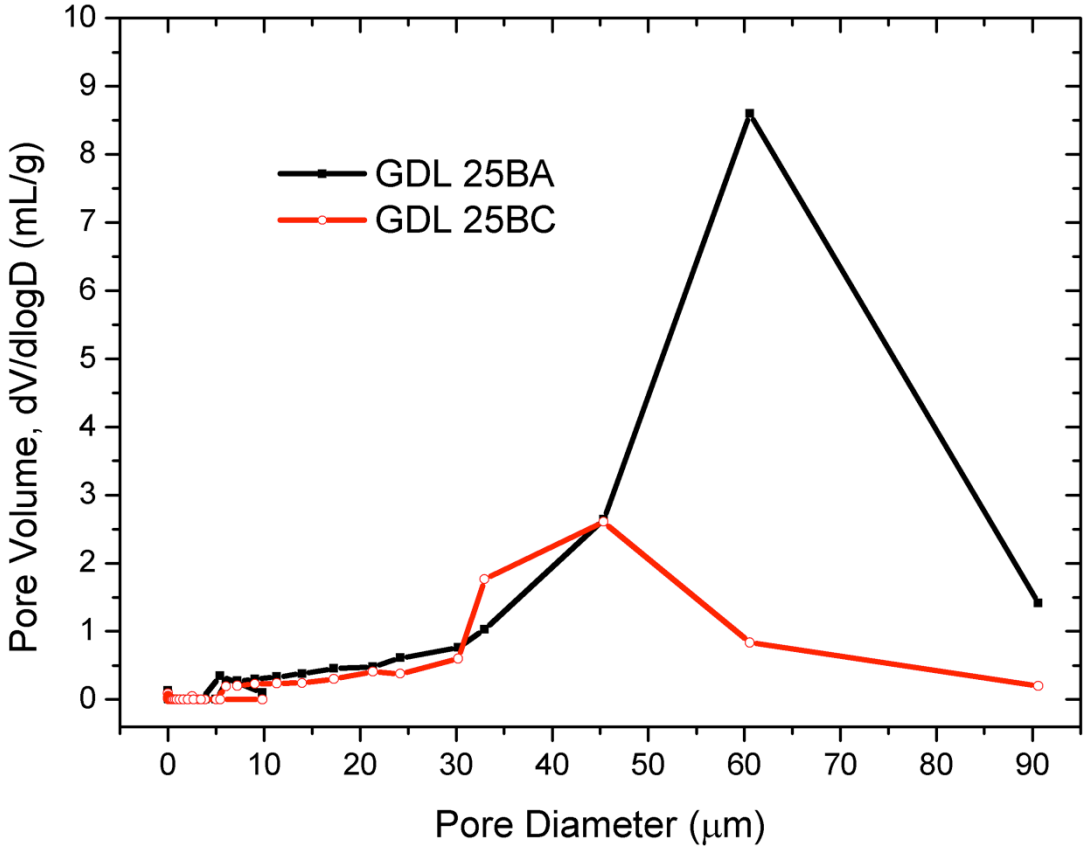

Figure 52: Change in pore distribution with (GDL 25BC) and without (GDL 25BA) an MPL.

Figure 53 shows the gradual change in the pore size distribution for the substrate when loaded with PTFE and a MPL. A significant decrease in the intrusion volume can be observed when the GDL is loaded with PTFE; this is also manifested in the decrease in the bulk porosity. When the MPL is applied, the GDL maintains constant bulk porosity. P50, P50T and GDS1120 also exhibit a similar behaviour. These findings are very interesting and could be due to the structure of the MPL and the surface roughness of the MPL in these GDLs.

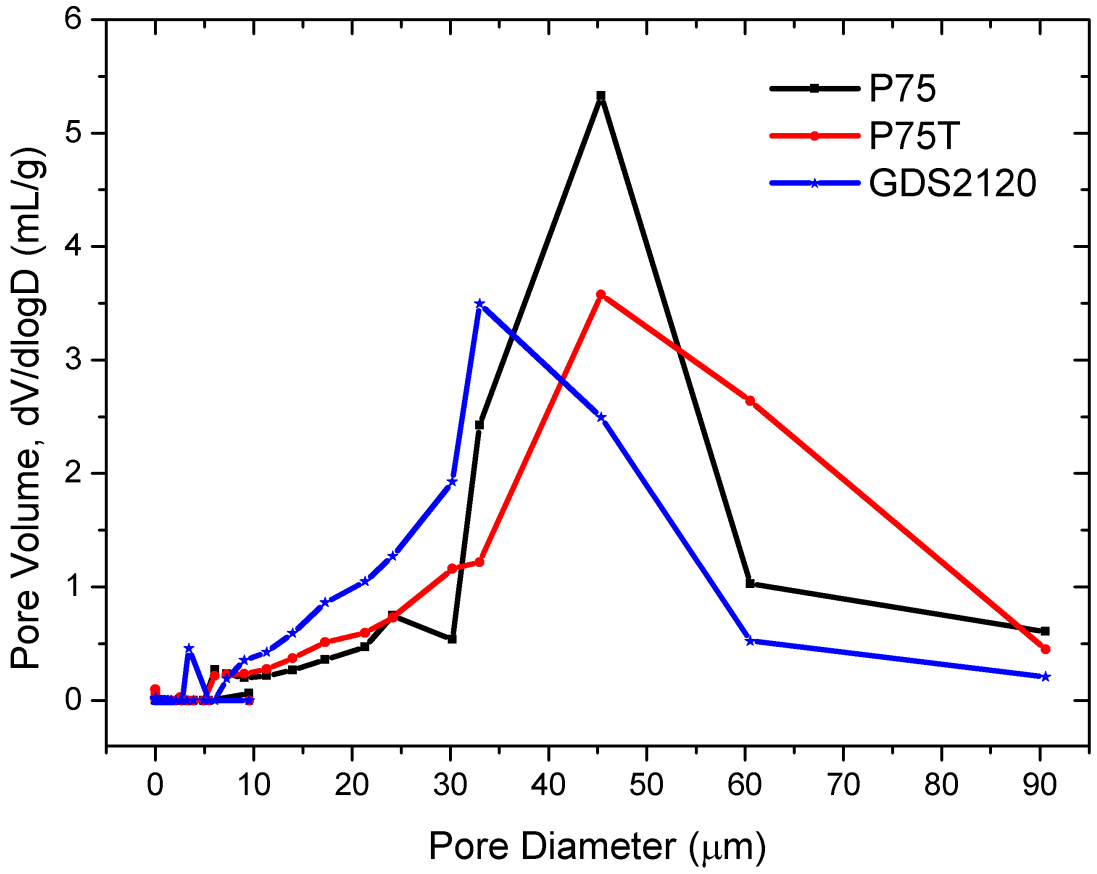

Figure 53: Pore size distribution change between unteflonated (P75), teflonated (P75T) and teflonated with a MPL (GDS2120) GDL samples.

Woven carbon cloth pore size distribution curves show a different trend to that of the GDL papers (Figure 54). Volume intrusion can be observed on a wide base of pore diameters that extends to high pore sizes as a result of the material construction. The results show that the three woven GDLs with no MPL have the same bulk porosity.

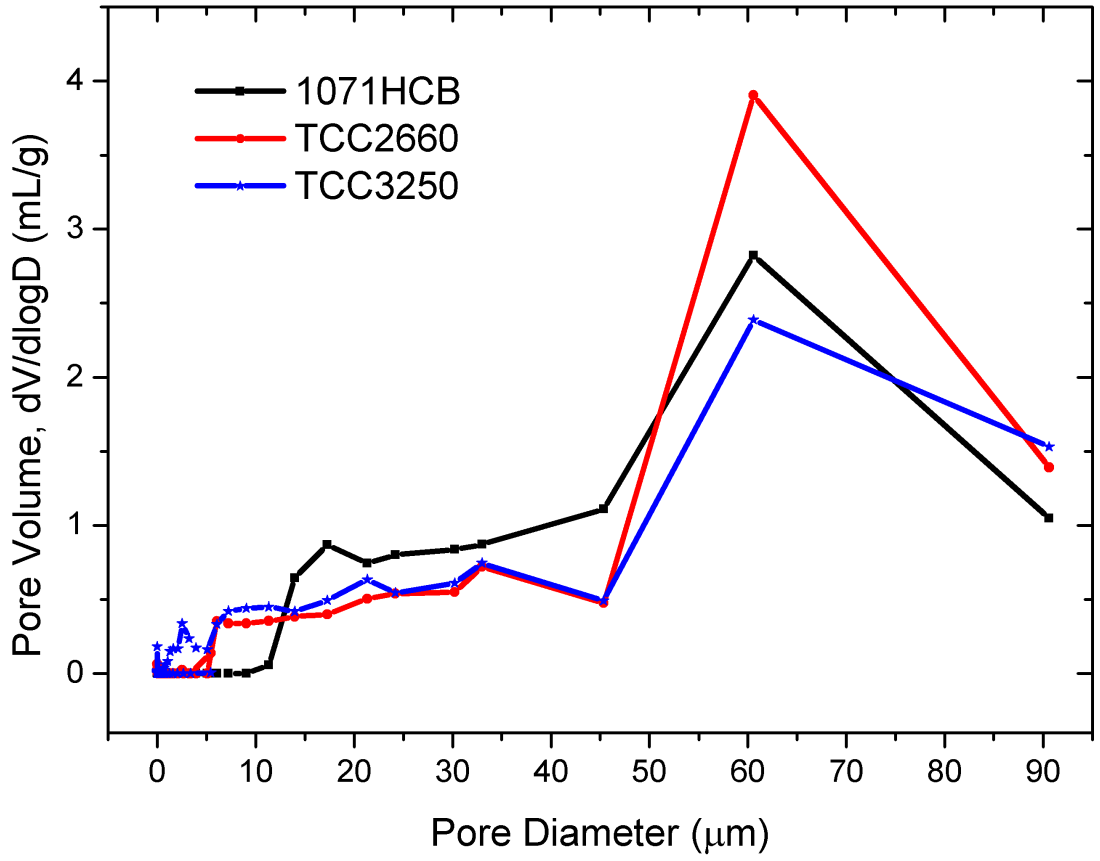

Figure 54: Pore size distribution for commercial woven cloth type GDLs.

4.4. Conclusions

In this section a wide range of GDL material properties have been reported, obtained through *ex-situ* analysis of various commercially available GDL materials, with a large range of constructions and compositions. This, as with the *in-situ* testing, highlights the need to be selective when constructing MEA to gain the combination of materials that provides the greatest performance for the given environment. The theoretical limiting current has also been calculated to highlight the differences in performance that are possible from the range of materials and their respective properties (particularly porosity and thickness).

5. Electrolyte testing and water management

In order to continue to build a picture of the behaviour and characteristics of each component part of the fuel cell (MEA) this chapter considers the electrolyte and the changes that it is likely to undergo during typical operation as well as its fundamental properties. Initially this section will look at the *ex-situ* mechanical properties (dimensional change with hydration) providing useful information to apply to the response of the whole system when operating. A MEA is then operated under various operating conditions including start-up and non-ideal flooding operation to observe the effects on the mechanical and electrical properties. This Chapter applies the knowledge gained from how the GDL material behaves (section 3) and the electrolytes relationship with hydration (section 5.1) to the full operating MEA.

From electrochemical impedance spectroscopy (EIS) measurements, Figure 55 shows a Nyquist plot for the fuel cell operated at 0.8 V. The high frequency intercept with the real axis represents the Ohmic resistance of the system, which is primarily due to the electrolyte membrane. A frequency of 5 kHz was used to monitor the resistance with time, measurements made every 1 s to follow transients.

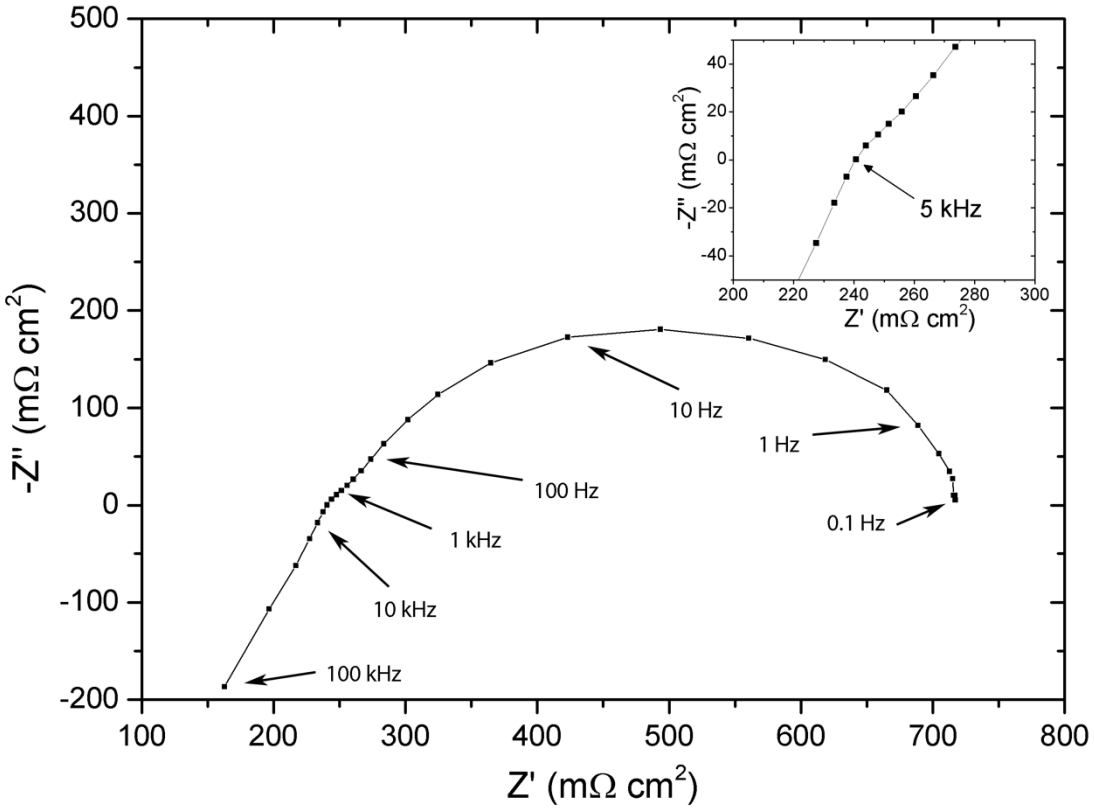

Figure 55. Nyquist plot of the fuel cell operating at 0.8 V with a voltage amplitude of 15 mV and a frequency range of 100 kHz to 0.1 Hz. Figure inset shows the 5 kHz point where the impedance is taken during the time scans.

5.1. Individual electrolyte and GDL properties

Before studying the effect of compression, dimensional change and water management on whole MEAs, it is necessary to characterise the individual components, i.e. the membrane and GDL. In this section the *ex-situ* derived relationship (Figure 57) using the Springer et al. equation and the result from Figure 56 will be referred to as '*ex-situ*' whereas the results obtained from the CCU experimentation is referred to as 'startup' results.

Membrane Electrolyte: The relationship between water content and thickness of Nafion 117, 115 and 212 (pure membrane, no GDL) is described in Figure 56, Figure 58 and Figure 59 respectively. Measurements were taken by weighing the sample and measuring the thickness with a micrometer. The water content of the electrolyte, λ (mol H_2O / mol SO_3^-), is related to the mass of the sample by Equation 16 [17].

Equation 16

$$\lambda\left(\frac{\text{mol } H_2O}{\text{mol } SO_3^-}\right) = \frac{\left(M_{Test} - M_{Dry}\right)\cdot\frac{1 \text{ mole } H_2O}{18.015 \text{ g } H_2O}}{M_{Dry}\cdot\frac{1 \text{ mole } SO_3^-}{1100 \text{ g Membrane}}}$$

Under ambient lab conditions the Nafion 117 material used has a measured thickness of 178 ±2 μm, this is in agreement with the '117' assignment (7 mils = 177.8 μm). Each thickness measurement was taken three times at various positions on the Nafion samples, giving rise to the error bars shown. The relationship between thickness and water content shows a linear fit with a gradient of 0.49 λ μm^{-1}. The dashed lines represent three water content regimes: $\lambda = 0$ represents a dry membrane; $0 < \lambda < 16.8$ represents the water content in equilibrium with air and $16.8 > \lambda > 22$ that for the membrane in equilibrium with liquid water [32].

Figure 56 shows a linear relationship between water content and thickness over the 'vapour' range. Upon exposure to liquid water, there is a sharp increase in the water content corresponding to liquid water saturation; this result suggests that exposure of an operating membrane to significant amounts of liquid water, as might be experienced during a flooding event, could lead to a relatively large increase in thickness.

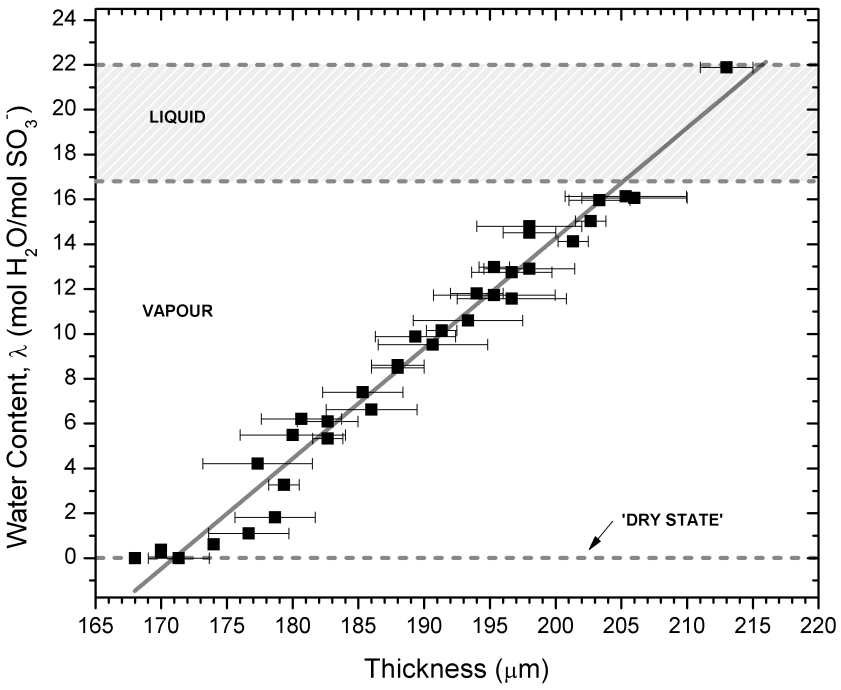

Figure 56. Relationship between thickness and water content of Nafion 117 across a range of hydration levels. Dry conditions were generated by treatment at 110 °C for 1 hr, vapour equilibrated measurements we taken at lab conditions and fully hydrated conditions generated by immersion in liquid water at 80 °C. Water content was calculated using Equation 16, the linear fit shown has a gradient of 0.49 λ μm^{-1}. The dashed lines represent three key water contents: dry, vapour and liquid.

Springer et al. [32], have presented a relationship equating conductivity (σ, S cm^{-1}) of Nafion 117 samples to water content (λ), see Equations 17 and 18.

Equation 17 $$\sigma_{30} = 0.005139\lambda - 0.00326 \; (for \; \lambda > 1)$$

Equation 18 $$\sigma(T_{cell}) = exp\left[1268\left(\frac{1}{303} - \frac{1}{273 + T_{cell}}\right)\right]\sigma_{30}$$

It is therefore possible to transform the trend from Figure 56 into a relationship between thickness and conductivity (and therefore resistance). Figure 57 shows the

ex-situ measured results transformed to equate to resistance values as reported in this study (mΩ cm^2) against thickness of electrolyte.

The resistance value obtained for the membrane thickness of 178 μm (see Figure 57) is equal to 835 mΩ cm^2, this point is used as a reference for analysis linking the relative displacement values (obtained from the CCU) with absolute thickness values. This approximation is possible as the initial resistance value of the startup test (Figure 61) is equal to 842 mΩ cm^2 therefore if prescribed an absolute thickness value of 178 μm, this enables direct comparison of both the *ex-situ* and startup data from the same initial point.

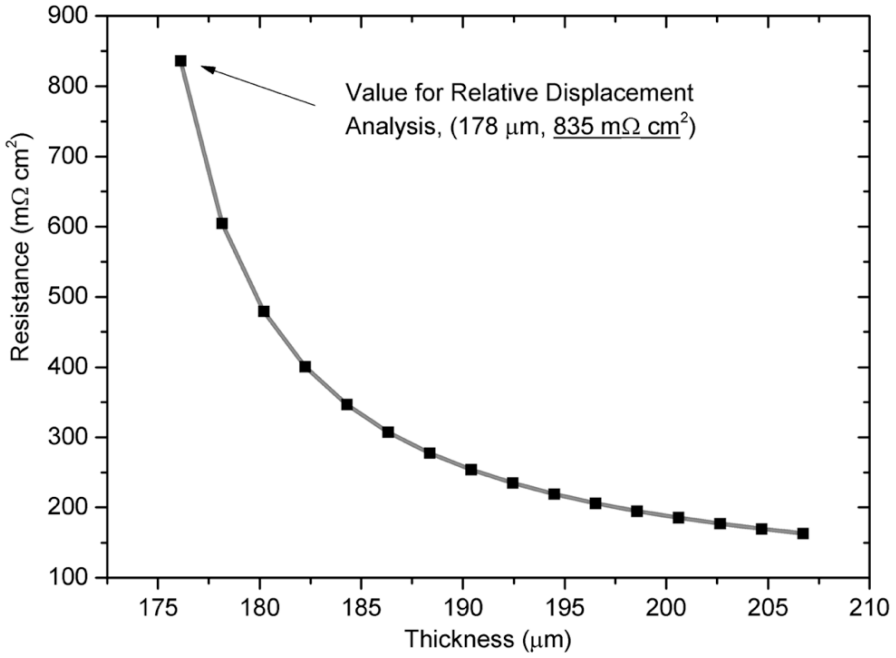

Figure 57: Relationship between resistance and thickness as calculated using Springer et al. [32] temperature adjusted conductivity and water content relationship. Water content then adjusted to thickness using the *ex-situ* relationship described above. The indicated value for resistance at 178 μm total thickness is 835 mΩ cm^2.

Table 12 shows the various data gained from *ex-situ* testing of Nafion samples. The 'as received' thickness refers to the sample at room temperature and humidity, the 'desiccated thickness' value was taken from a sample that had been stored in a desiccator for at least 48 hours and the hydrated thickness value was taken after the sample had been immersed in 18 MΩ cm de-ionised water at room temperature for at least 48 hours. The values were taken by averaging 10 thickness measurements at different points across the membrane using a micrometer.

Table 12: Data of samples of Nafion 117, 115 and 212 undergoing *ex-situ* hydration and dehydration at room temperature in 18 MΩ cm de-ionised water and a lab desiccator

Nafion Membrane	'As received' thickness (μm)	Desiccated thickness (μm)	Hydrated thickness (μm)	% Change	Water content gradient ($\lambda\ \mu m^{-1}$)
117	178 ± 4	170 ± 2	212 ± 2	18	0.49
115	129 ± 1	126 ± 2	154 ± 2	19	0.57
212	52 ± 0	51 ± 1	71 ± 1	36	0.93

The data from Table 12 has two purposes. Firstly, with the values matching those of the other published data, as can be seen in Table 5, this means our sample properties are similar. Secondly, it gives us a reference for the range of values to expect during experiments where thickness change due to hydration occurs.

Of the three types of Nafion membrane being tested (117, 115, 212), the 212 membrane is made using a different manufacturing technique. The 212 is a dispersion cast membrane as opposed to the 115 and 117 which are extruded materials [104]. From the percentage changes in thickness observed in Table 12 the manufacturing method has the effect of increasing the percentage thickness change.

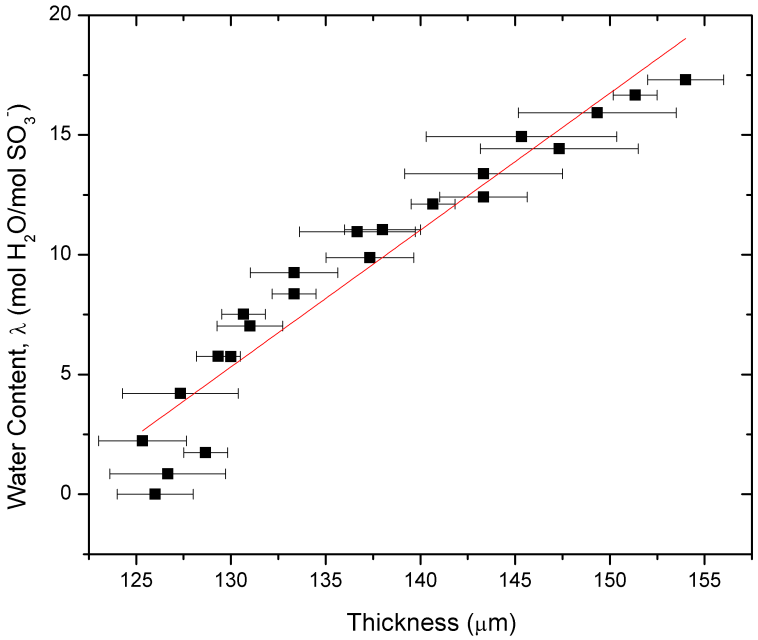

Figure 58: Graph of the thickness of Nafion 115 against the water content. The Linear fit has a slope of 0.57 λ μm^{-1} and all measurements were carried out at room temperature.

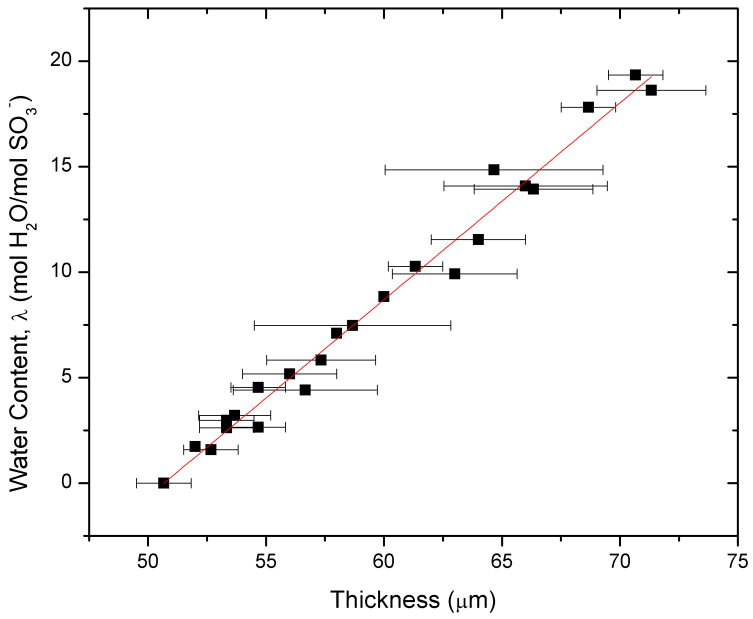

Figure 59: Graph of thickness against water content for a pre-treated sample of Nafion 212. The linear fit line has a slope of 0.93 λ μm^{-1} and all measurements were carried out at room temperature.

Gas diffusion layer: When a fuel cell is operated in constant displacement mode, which is analogous to a fuel cell compressed by tie-rods without stress relief, the compression changes as the membrane swells. This swelling of the membrane will impose a force on the GDL material. Previous work has shown that there is a direct relationship between the compression force applied to a GDL material, its change in thickness and the resulting resistance of the sample, this being a combination of a change in the effective resistance of the GDL (as the fibres coalesce under compression) and the contact resistance with the fluid flow plate [87]. Figure 60 shows the relationship between resistance and compression for the GDL used in our MEAs (Toray H060) in the same CCU apparatus. The gradient of the trend is -9.2 mΩ cm^2 MPa^{-1}, this agrees well with the work previously published where a value of approx. -10 mΩ cm^2 MPa^{-1} was obtained for this region of compression [87].

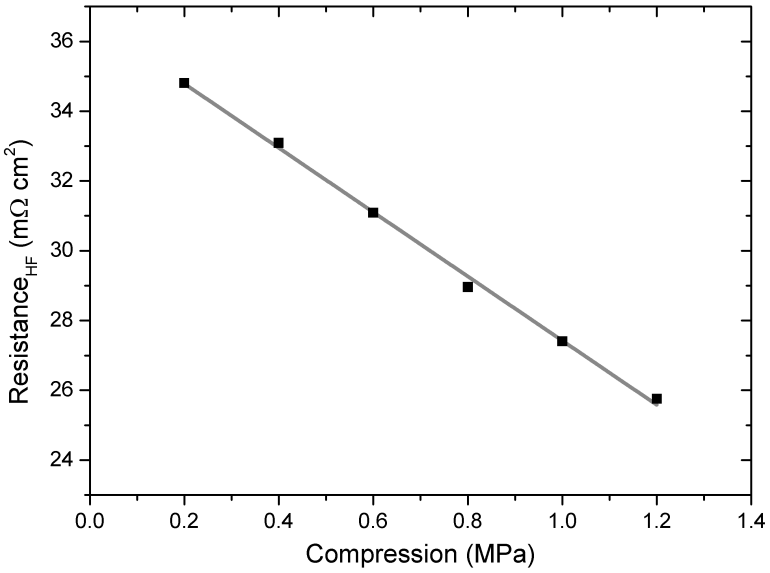

Figure 60. Relationship between resistance and compression of a single piece of Toray H060 measured using the CCU. The gradient of the line is -9.2 mΩ cm^2 MPa^{-1}. In-between each step increase in compression the sample was returned to 0.2 MPa.

5.2. Fuel cell start-up

Upon start-up of a fuel cell, the membrane must be hydrated from a 'dry state' to operational conditions; typically this is achieved by passing a humidified gas through the flow field; this process involves the membrane physically expanding (swelling) which has an impact on the adjacent GDL.

Figure 61(a) shows the resistance and displacement trend in controlled compression mode for the fuel cell with humidified nitrogen flowing on one side of the cell (80 °C, N_2 flow rate of 100 ml min^{-1} at 100% RH). There is a correlation between the resistance and thickness change, both reaching equilibrium after ca. 125 s. Figure 61(b) shows the hydration transition under the same conditions in constrained mode (controlled displacement mode); when the MEA is hydrated, resistance decreases and

the pressure exerted on the MEA increases significantly. The transition to equilibrium occurring over a similar, but shorter, time period than that in constant pressure mode.

Some variability in the conductivity of notionally dry MEAs was observed between different samples due to variation in the lab conditions and duration between sample drying (at 110 °C) and installation in the apparatus. However, the final resistance was always of the order of 200 mΩ cm^2. The displacement response lags the resistance change in constant pressure mode but leads it in constrained mode; the resistance reaches its equilibrium in ~100 s whereas the displacement takes ~125 s to reach equilibrium. In controlled compression mode the expansion of the membrane leads to an increase in the membrane thickness (swelling) of 30 μm coupled to a reduction in resistance of ~630 mΩ cm^2. However, constrained compression mode does not best reproduce the most common method of fuel cell construction (tie-bars), which is better replicated by the constrained displacement operating mode. In controlled displacement operating mode the compression change upon start-up (hydration) is + 0.56 MPa. The resistance value of the membrane at the end of the start-up (hydration) transient under each operation mode is different, with constrained displacement mode lower than constrained compression; a 22% improvement is observed. A reduction in resistance is expected due to the improved contact resistance from the crushing of the GDL materials with the increased compression (Figure 60). A significant change in compression will occur each time a fuel cell MEA undergoes a hydration cycle, which will often be a feature of a standard start-up / shutdown cycle. The stresses that this can impose on a stack are therefore significant and a potential cause of failure.

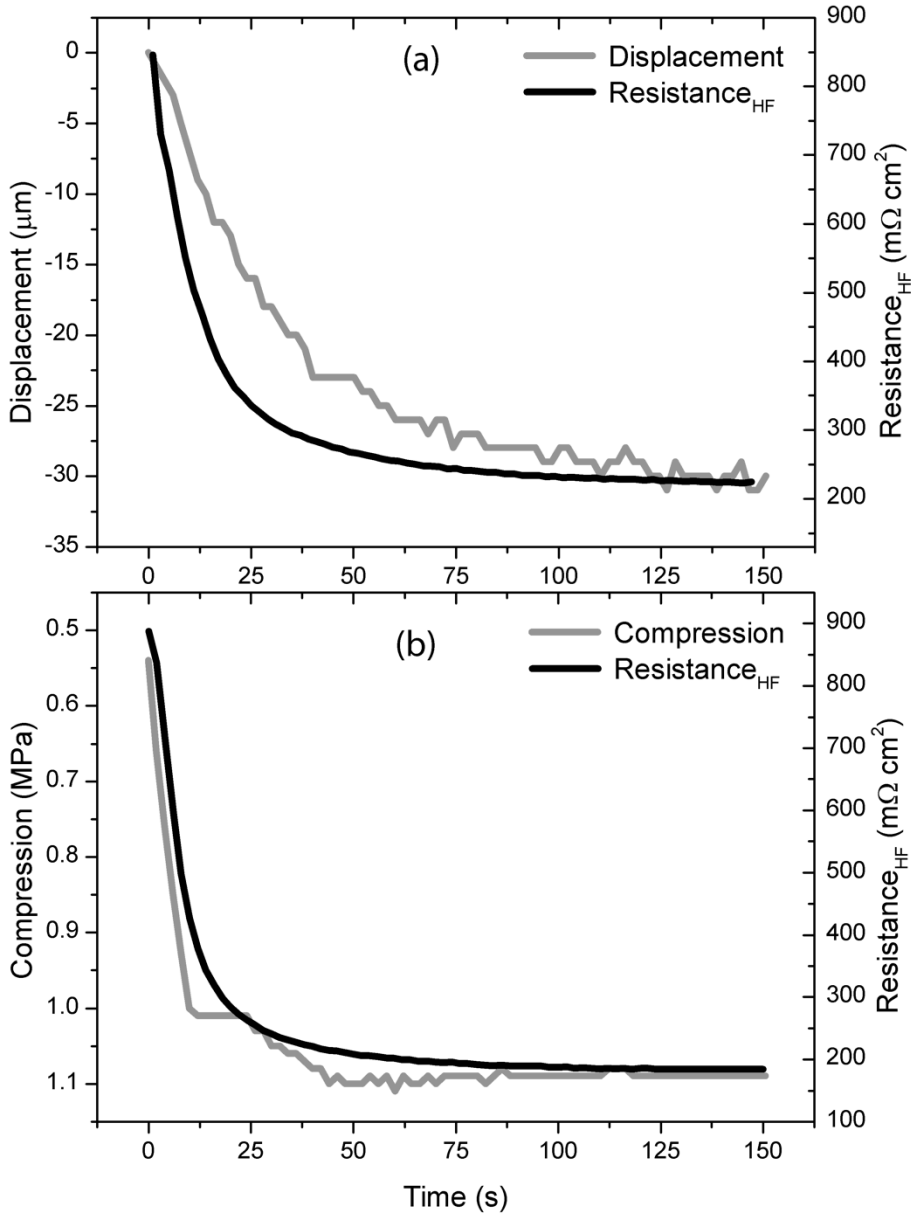

Figure 61. (a) Controlled compression mode (0.2 MPa): The displacement and high frequency resistance response for hydration of the fuel cell from a dry state with humidified nitrogen. (b) Controlled displacement mode: Initial hydration of an MEA with constrained displacement to enable measurement of compression change during start-up. Operating conditions for both tests were cell temperature at 80 °C and 100% RH on the anode with the cathode sealed. The gas flow rate was 100 ml min^{-1}.

Figure 62 shows the non-linear relationship between resistance and displacement for the initial hydration of an MEA, whereby the MEA goes from a 'dry state' to an initial operating mode where hydration equilibrium is reached with the humidified gas.

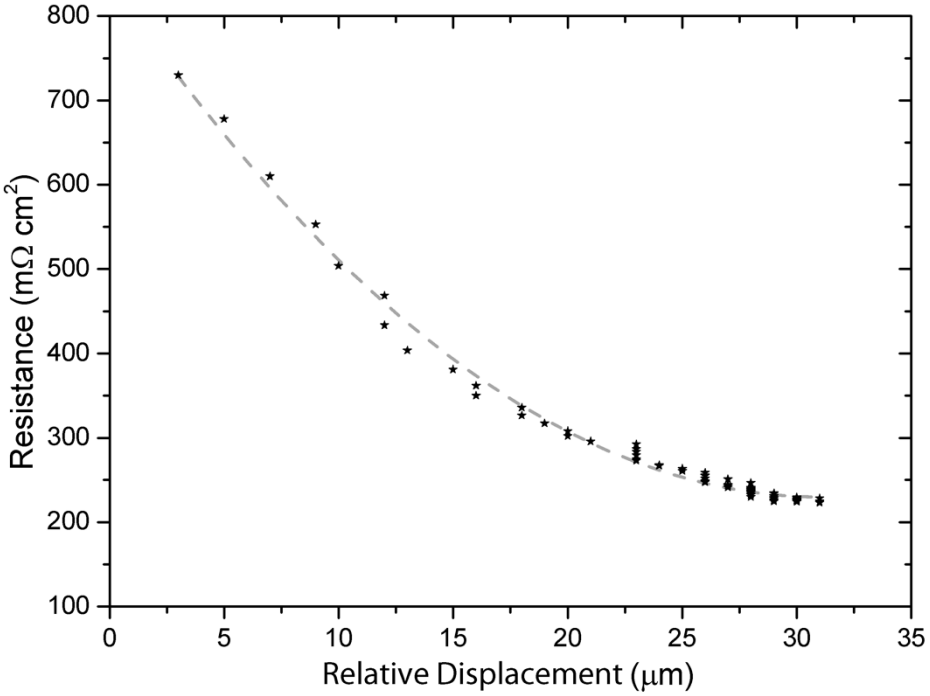

Figure 62. Relationship between resistance and relative displacement for start-up of the fuel cell from the data in Figure 61(a). Data obtained in compression control mode at 0.2 MPa.

In order to further explore the relationship between resistance and displacement the experimental results (Figure 62) were compared with the theoretical relationship from Zawodzinski et al., this is shown in Figure 63. The purpose of which is to understand the differences observed in practice compared to the model.

Two curves are plotted in Figure 63, for startup and *ex-situ* data, both have a common starting point in resistance and displacement, however with increasing displacement,

the resistance is lower than that of the observed values while following a similar trend culminating in a plateauing in the region of 200 mΩ cm^2. The nonlinear comparison is a result of the unknown equilibrium position of the startup data. The *ex-situ* experiments were performed on samples at equilibrium while the startup study is dynamic and hence does not reach equilibrium. For the experimental measurements, the resistance value is akin to an average measurement across the active area of the cell whereas the displacement measurement is in essence the maximum value noted across the cell area. Due to the heterogeneous hydration of the cell as the wave front of hydrated gas flows over the cell this trend is expected [105]. Also noted on this graph is a line associated with the minimum resistance obtained from the flooding experiments (see Figure 64), this shows that when the cell is operating, and electrolyte hydration has reached equilibrium, the resistance does equate to that of the *ex-situ* derived relationship.

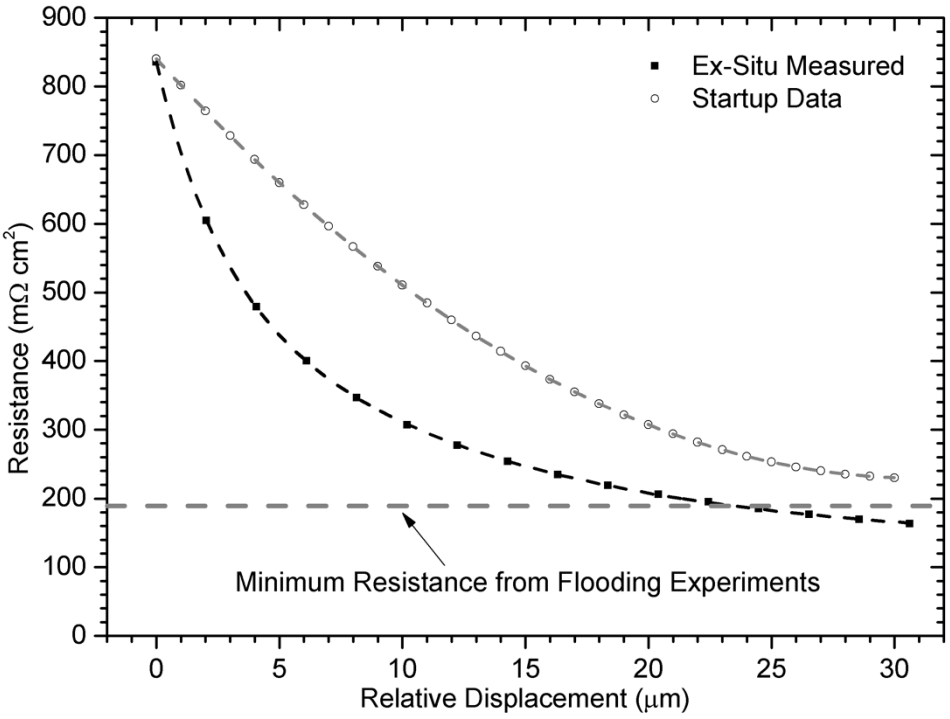

Figure 63: a) Relationship between resistance and relative displacement from startup plotted alongside *ex-situ* relationship (previous figure).

The current technique gives the maximum value for the displacement; however, improvements in the technique by multiple measurement points could give improved spatial resolution. For a system at equilibrium it would be possible to measure the relative displacement from fuel cell system startup and thus derive resistance (or water content of the membrane) values. An application of this technique would be inclusion in a fuel cell stack system enabling the local monitoring of cell hydration and therefore individual cell resistance.

5.3. Flooding effects on MEA operation

Durability studies of PEFC operation often feature abrupt 'spikes' of negative performance. These transients are usually the result of a flooding event at one of the electrodes (usually the cathode) [50]. Here we examine the effect on the membrane conductivity of these events and the impact on the dynamic stress / strain conditions in the cell.

Figure 64 shows a cell running under non-ideal conditions, expected to lead to flooding, Large current spikes are observed over periods ranging up to 100 s, swelling of the membrane by over 30 μm and significant changes in the resistance of the membrane (over a range between 183 and 212 mΩ cm^2) are seen to be associated with the current spikes.

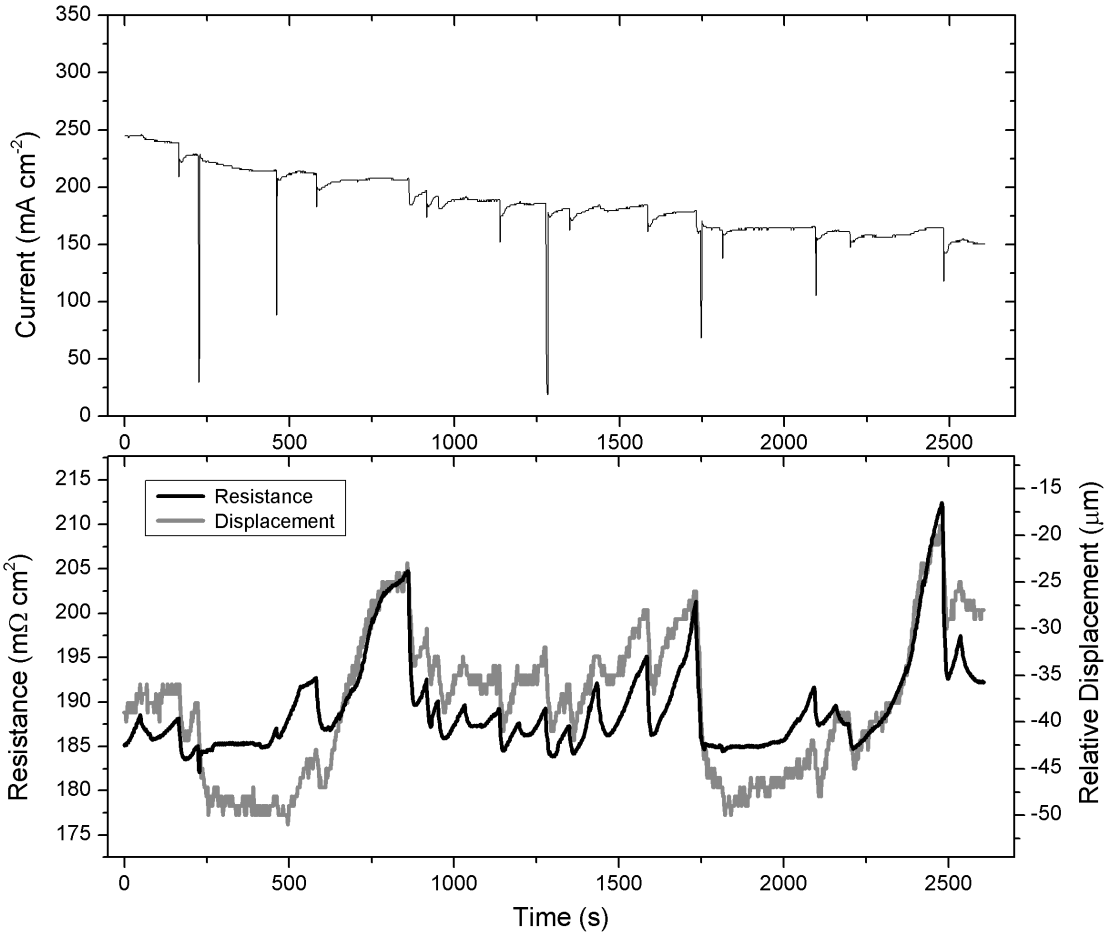

Figure 64: Controlled compression mode (0.2 MPa): Voltage trace showing spikes in voltage caused by water flooding. The cell is run at high humidity resulting in the high frequency resistance decrease and subsequent increase in thickness observed. The cell was operated with constant voltage of 0.7 V at 80 °C with anode and cathode humidification of 100% RH at 85 °C and flow rates of 50 ml min^{-1} each. Displacement is relative to the thickness of the system at the start of the experiment (not shown).

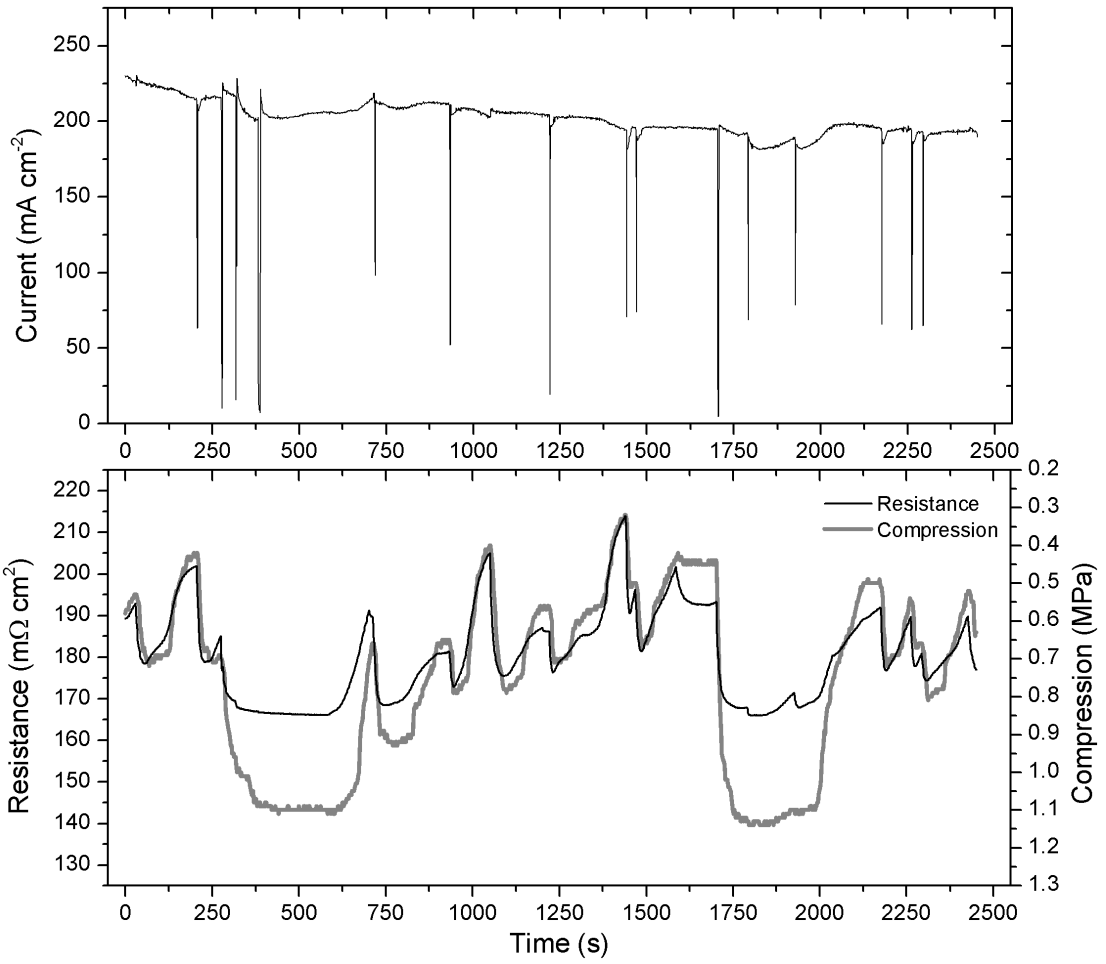

Figure 65: Controlled displacement mode: Trends observed when displacement is held constant with the compression being measured while flooding spikes occur. The cell was operated with constant voltage of 0.7 V at 80 °C with anode and cathode humidification of 100% RH at 85 °C and flow rates of 50 ml min^{-1} each.

Figure 65 shows the fuel cell operating in controlled displacement mode. The cell was operated at a constant voltage of 0.7 V with a flow rate of 50 ml min^{-1} for both the anode and cathode gas (H_2 and air). The controlled displacement mode enables the compression between the flow plates to be measured while the cell is running. Figure 65 shows that resistance decreases when water flooding spikes occur, as seen previously, and the compression increases. The compression increase is due to the

membrane swelling and forcing the GDL material into the flow field plate, which is detected by the CCU. The resistance is also measured with the range observed being greater than that observed in Figure 64, this is due to the contact resistance change that occurs when the GDL material is compressed, as seen in Figure 60.

As the GDL is compressed into the flow field plate by the expanding electrolyte membrane there are several mechanisms that affect the overall ohmic response. The most significant of which are contact resistance change between the GDL material and the flow field plate and the increased internal connections between the fibres of the GDL [87].

Figure 66 shows the fuel cell operating in constant current mode under conditions expected to give minimal flooding or voltage spikes. However, it is clear that while the system appears relatively stable with respect to voltage (only ~ 20 mV variation), there is an appreciable change in the resistance and displacement of the MEA. The resistance change in the plot varying by ~ 50 mΩ cm^2, while the membrane thickness is changing by a total of 16 μm over the period; these changes also correlate exactly with the variations that occur in the voltage trace (see Figure 66 inset).

The performance of the cell under these operating conditions suggests that the system is operating in a dynamic manner in terms of membrane hydration. Due to the relatively unchanged voltage trace, it is likely that the majority of the active area is operating at a near constant level of performance. The large variations in resistance and displacement could therefore be due to the nature of the measurement being an average and a maximum for the resistance and displacement respectively.

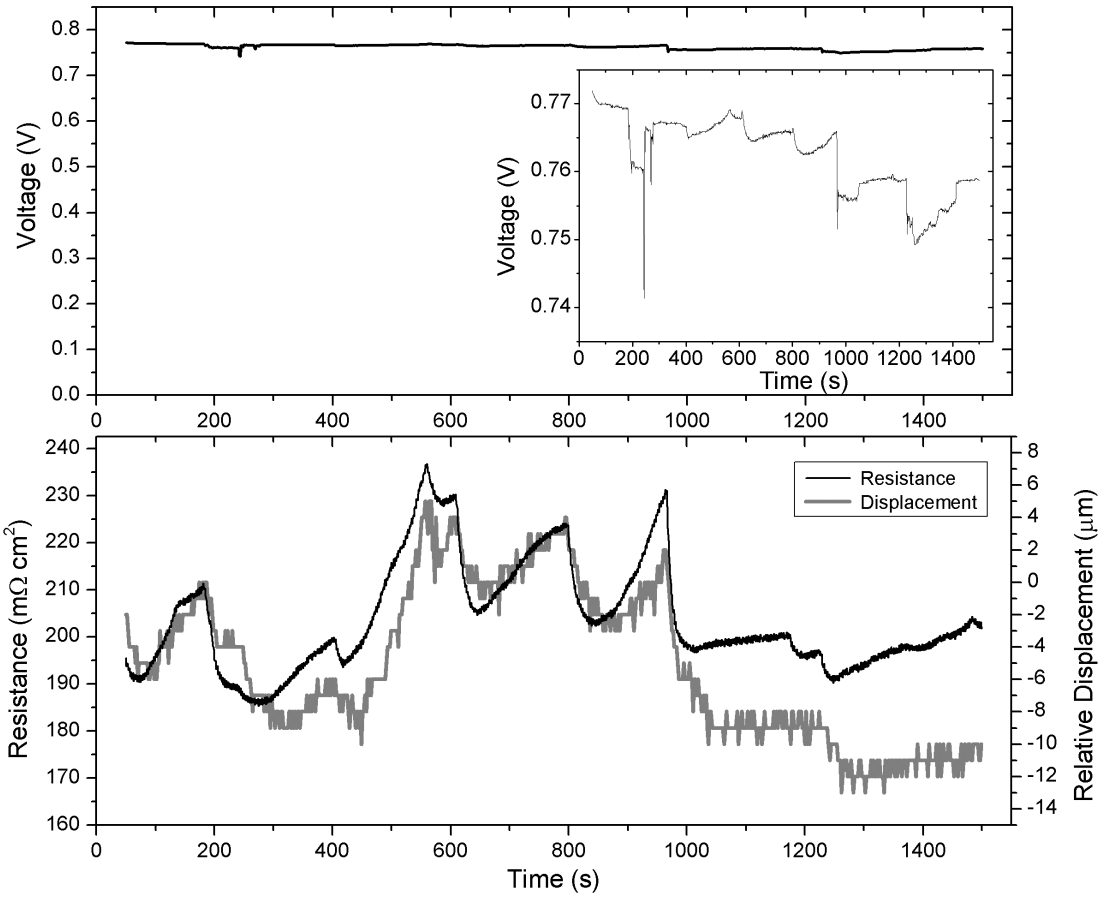

Figure 66: Controlled compression mode (0.2 MPa): Graphs showing the operation of a fuel cell in constant current mode (200 mA cm^{-2}) under conditions expected to give minimal flooding (cell at 85 °C with anode flow rate of 100 ml min^{-1} at 75 °C and 100% RH). The top trace shows the voltage variation with smaller scale plot inset. The bottom figure shows the change in high frequency resistance and thickness of the MEA during operation.

5.4. Flooding simulation by water injection

To verify that the voltage performance transient 'spikes' seen in Figure 64 & Figure 65 are indeed a result of flooding, water injection into the gas stream at the inlet of the anode was carried out to simulate the effect of flooding. Figure 67 shows the cell operating at a constant current of 200 mA cm^{-2} when 2 ml of water was injected into

the gas stream (20 s from the start of the run). A voltage spike of ~250 mV resulted with a decrease in the resistance of the membrane to the minimum resistance level observed of the electrolyte and a significant swelling of the membrane by around 12 μm.

The water injection causes a mass transport limitation by blocking pores in the GDL and / or the flow field, temporarily starving areas of the electrode of reactants, so decreasing the voltage. The period between the injection of water and the effect on the system is attributed to the time for the liquid water to get from the injection point to the MEA. The time taken for each change to occur also differs; the voltage spike recovers to nearly the initial voltage within approximately 14 seconds, the resistance change occurs within 12 seconds and the displacement change happens over 120 seconds. The significantly longer time scale for the displacement change is likely due to the control delay of the CCU.

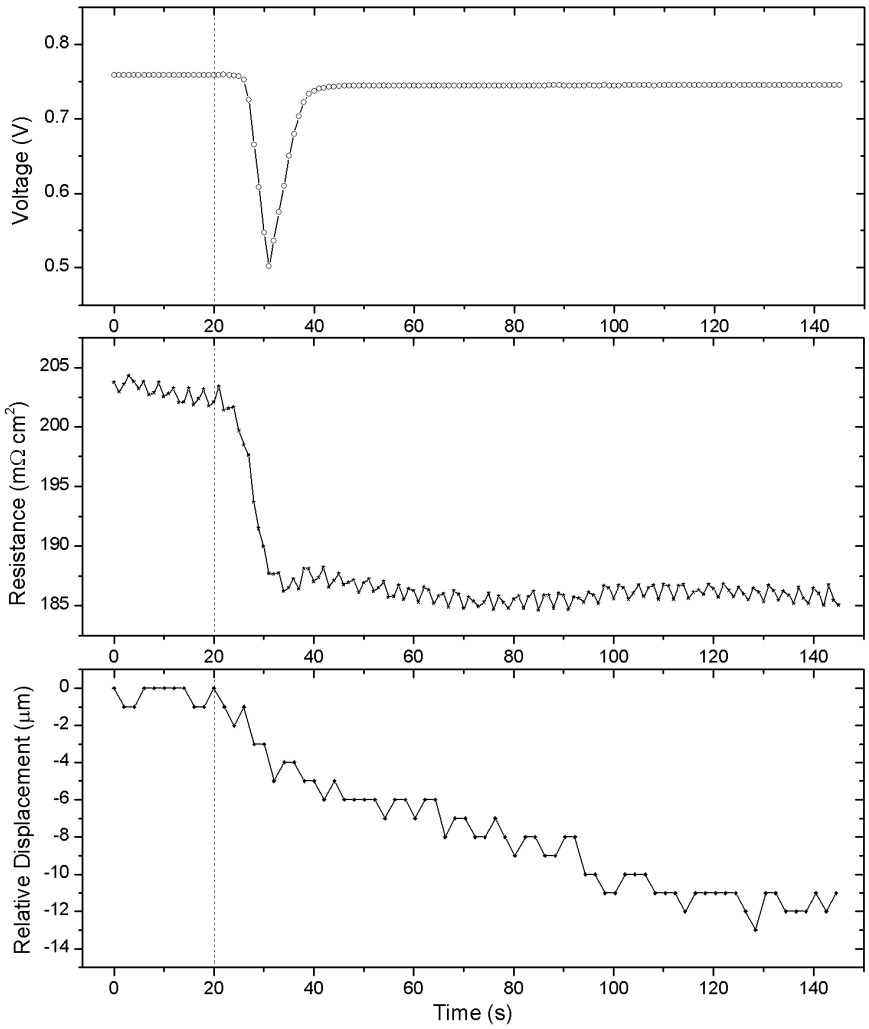

Figure 67: Controlled compression mode: Transient response after injection of the 2 ml water into the anode inlet of the cell. The water was injected into the line at 20 s. The cell was operated in constant current operation of 200 mA cm^{-2} with a cell temperature of 80 °C and anode and cathode heated lines at 50 ml min^{-1} and 100% RH at 75 °C.

5.5. Relationship between resistance, displacement and compression

Figure 68 shows the relationship between the high frequency resistance and the thickness of the MEA (relative displacement) based on the time-varying data points for 'flooded mode' operation, similar to that in Figure 64. The time-varying data points convert into a consistent relationship between resistance and thickness. As the membrane swells the resistance decreases to a point where the membrane has reached maximum saturation and the material's lowest resistance has been reached.

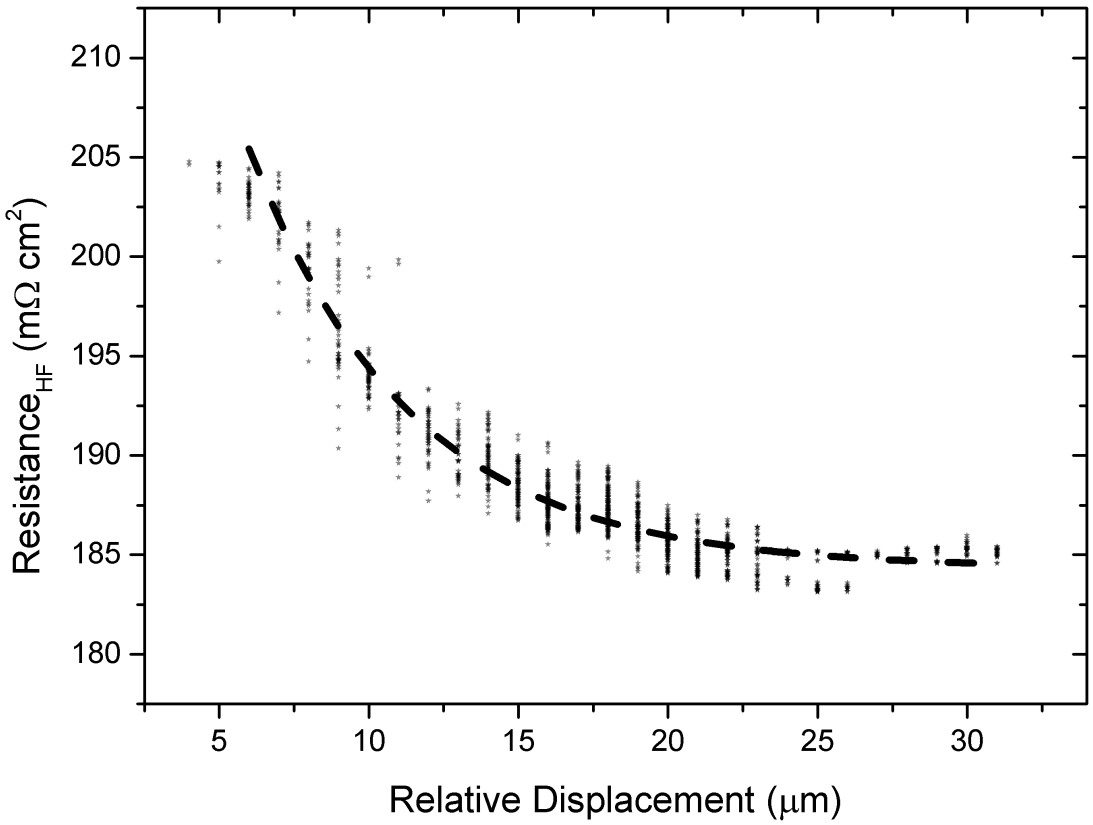

Figure 68. Relationship between the resistance and the relative displacement of an operating MEA. The cell is operated in a 'flooding mode' similar to that of Figure 64.

Figure 69 shows the relationship between resistance and compression of an operating MEA in flooding mode, similar to that of Figure 65. The lower resistance at the high compression region, compared to that in Figure 68 at high displacement, is a result of the reduced GDL / contact resistance due to the 'crushing' effect of the expanding membrane on the GDL in constrained displacement mode.

At the fully compressed region (of Figure 69) the resistance is approximately 15 mΩ cm^2 lower than for constant displacement operation (Figure 68). Taking the value of the gradient of Figure 60 as a guide to the reduction in resistance caused by GDL compression, it can be seen that this difference can be attributed to the crushing of GDL resulting in the previously reported improvement in bulk and contact resistance [87].

Figure 68 and Figure 69 are taken from an operating fuel cell undergoing flooding, whereas Figure 62 is from data of the fuel cell during start-up. The way this differs is by the start-up operating mode getting the MEA to vapour equilibrium whereas the flooding data results in liquid equilibrium. The relationship between resistance and displacement shows a similar trend.

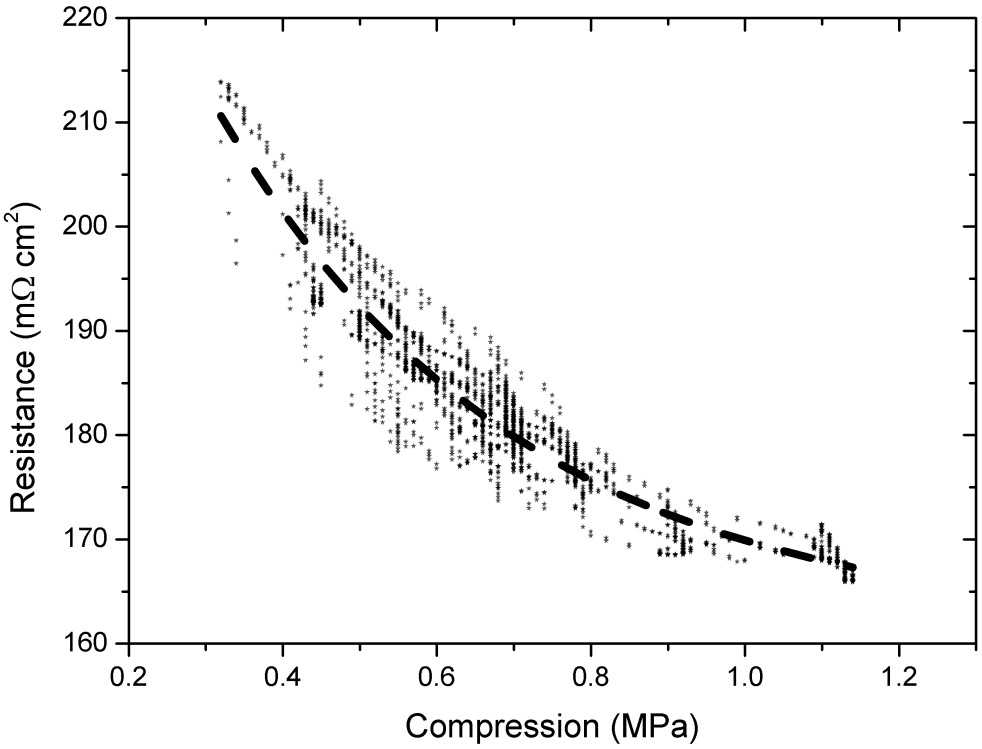

Figure 69: Relationship between compression and resistance of an operating MEA that is constrained at a fixed displacement with a fit as a guide to the eye. The data is taken from a cell operating in flooding mode similar to Figure 65.

Figure 68 and Figure 69 show that there is a consistent relationship between the resistance and mechanical properties, while Figure 64 and Figure 65 show that there is a correlation between the timing of current spike (flooding) events and changes in resistance and dimension. However, there is no consistent quantitative relationship between the size of the current spike and the extent of the resistance / mechanical change. The reason for this is that the current spike is primarily a consequence of the blocking effect of water build-up in the cell, acting to starve the electrode of reactant. In a single channel serpentine flow field, liquid water removal is rapid and therefore the current spike is a relatively short lived event compared to membrane hydration due to liquid water. In addition, liquid water generation, as for example droplets in

the flow field, is not a homogeneous process. Different amounts of the cell may be affected by the blocking effect and hydration effect.

5.6. Conclusions

During start-up of the fuel cell, significant compression changes occur (in controlled displacement mode) as the MEA hydrates, this type of hydration cycling will occur during repeated start-up and shutdown procedures and may cause significant degradation in cell performance. The changes in membrane dimensions due to hydration transients that are translated through the GDL to result in a net change in thickness of the MEA (in controlled compression mode). In controlled displacement mode the overall thickness of the system is constant and hence replicates a typical tie-bar type fuel cell construction, this leads to crushing of the GDL as it absorbs the increase (analogous to a spring) in thickness of the electrolyte, which in turn produces an increase in compression within the cell.

From comparison between the startup experiment obtained relationship between the resistance and displacement and the *ex-situ* derived equivalent trend there appears to be a strong correlation. This is significant as it not only adds weight to the experimental technique but also indicates that it would be possible to measure thickness in an operating system relative to startup and have knowledge of the electrolyte water content and therefore resistance.

Flooding has a significant impact on the hydration state of the membrane as the liquid water is absorbed by the electrolyte that, in turn, affects the conductivity and causes a relatively large change in the thickness of the electrolyte.

Monitoring the change in thickness of the MEA during operation is a useful diagnostic to compliment conductivity and current / voltage measurement in determining the role of membrane hydration and contact resistance impact on fuel cell performance and durability or indeed to act as a method to determine real-time resistance measurement in an unobtrusive manner and without expensive test equipment. Flooding may be a major cause of long-term performance degradation due to the destructive nature of stress / strain cycles on the GDL caused by the hydration transients. The compression transients suggest that a dynamic compression control regime would be beneficial for practical fuel cell construction.

6. Compression effect on performance

Throughout this thesis the component level analysis has built up to enable analysis of the operating system. The test rig has been operated under extreme condition to highlight the relationships between the mechanical and electrochemical mechanisms. This chapter builds further on this work by applying the system to investigating the affects of compression on performance of an operating cell under typical conditions. The pure mechanical properties of the whole MEA system are analysed leading to the characterisation of the system as a network of spring and piston components. The performance of the cell is then interrogated using polarisation performance analysis and EIS to look at the mechanisms for the change in performance with the variation of compression. A focus is then applied to how the system is expected to behave from a theoretical standpoint of the modelling of limiting current and an assessment is made of the suitability in the real world of this calculation.

6.1. Mechanical properties

In order to get mechanical values purely for the MEA and GDL the system response was first obtained in order to subtract it from the total response. Figure 70 shows the system response when the cell is empty, the displacement data corresponding to each compression is subtracted from every response in this section (section 6.1) in order to ensure that the responses are material specific and not an artefact of the machine.

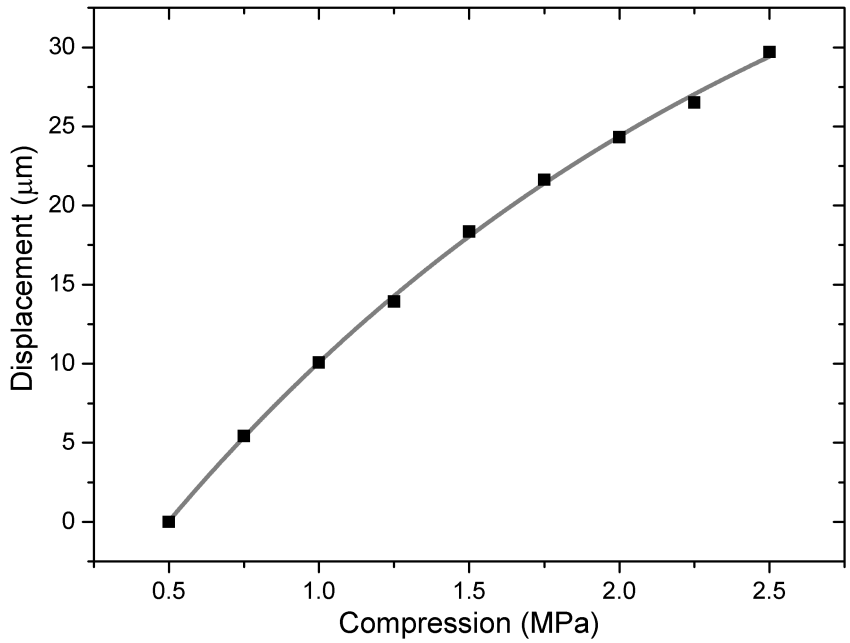

Figure 70: System response graph for the CCU when empty with increasing compression. The value of displacement at each compression is subtracted from the total response for all subsequent data in this section (Section 6) thus enabling all data to represent the material being tested.

The mechanical analogy of springs in series can be used to explain how composite materials of different thickness and compressibility experience different dimensional changes when force is applied [106].

An assumption is made that the membrane remains in a constant state of hydration over the compression range, therefore the membrane will not expand or compress (swell or contract due to hydration), under which circumstances the membrane has the mechanical properties of a piston and not a spring [107]. The GDL used in experiments is a Toray material (H-060) with a 190 μm initial thickness a measured porosity of 63.1% (manufacturer data 78%) [48].

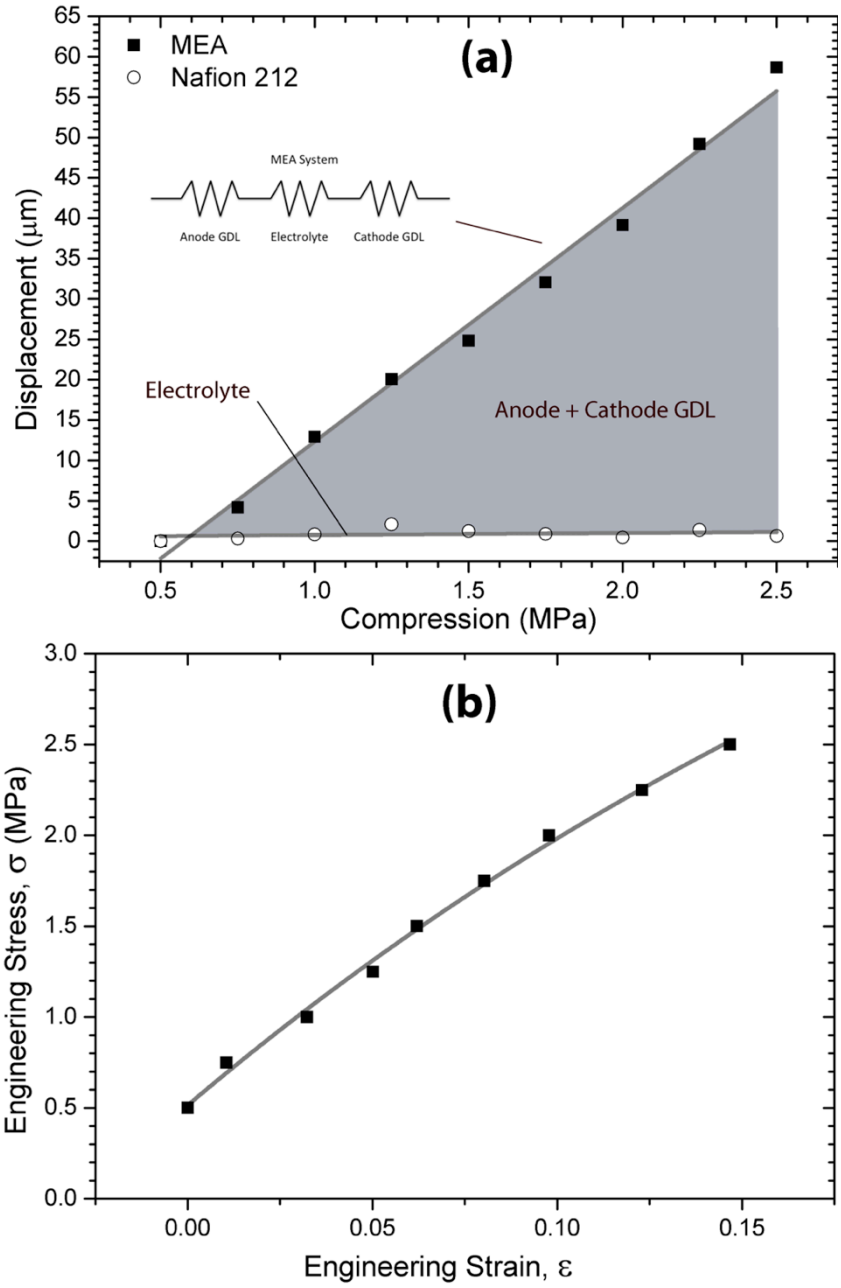

Figure 71: (a) Trend between the displacement and compression of the MEA showing full MEA and the electrolyte with the shaded area representing the remaining components (anode and cathode GDLs). (b) Engineering stress / strain graph showing non-linear behaviour of the MEA which indicates stress-induced plasticity. This agrees well with previously published work that showed irreversible compression over this range [87].

Figure 71 (a) shows the displacement trend for the MEA undergoing compression change (similar to the data from Figure 76 later), included is the trend for Nafion 212 showing that the displacement change is mostly due to the GDL crushing and only partly due to the compression of the Nafion. The gradients of the MEA and the electrolyte fits are 28.94 and 0.24 μm MPa^{-1} respectively; this shows that the electrolyte change is effectively zero and indicates that effectively all the displacement change is associated with the GDL materials. The total change in displacement over the compression range for the MEA is 59 μm, representing the total change associated with the two GDLs and the electrolyte. However, this displacement is relative to the initial compression of 0.5 MPa and there will be additional displacement change associated with the compression to 0.5 MPa. The total initial thickness of the MEA is ~450 μm, measured *ex-situ*.

Figure 71 (b) shows an engineering stress / strain diagram, the non-linear response indicates stress-induced plasticity. This trend agrees with previously published work, which showed irreversible compression loss associated with GDLs over this compression range [87]. A straight line fit of this curve however, gives a Young's modulus (E_c) of 13.7 MPa (see Figure 72) which corresponds directly with moduli reported by other authors (range of 9.5 – 13 MPa) [93].

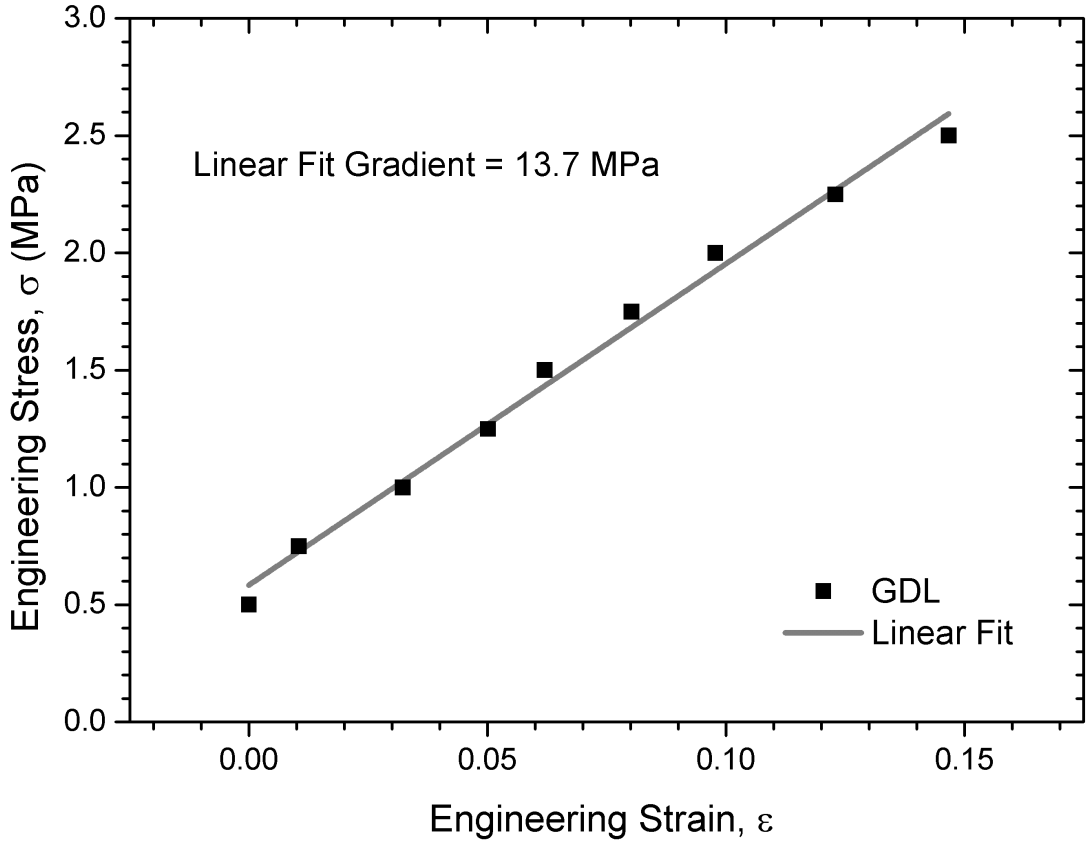

Figure 72: GDL engineering stress strain diagram with linear fit in order to obtain the Young's modulus for the material. From the linear fit to the data a Young's modulus of 13.7 MPa is obtained.

6.2. Polarisation performance

Analysis of the polarisation performance of any type of fuel cell is the most common way used to assess the operational characteristics of the cell. This is in part due to the lack of specialist equipment required to perform the test. In this section the polarisation performance is compared at different levels of compression with assessments made on the effects of the compression at the various operating regions.

Figure 73 (a) shows repeat polarisation curves for three different cell compressions. For each compression force (0.5, 1.0 and 2.5 MPa), three repeat runs were performed and averages of the limiting current taken. It is seen that as the compression increases the performance at the higher current densities is restricted. The current density limit, i_L, varied by ~110 mA cm^{-2} at 0.4 V across the range of compression force, as can be seen inset in Figure 73 (a). This limit will be affected by the gas flow rate with a maximum current density at 1.0 cathode stoichiometry of 1.2 A cm^{-2}. For a compression of 0.5 MPa a 620 mA cm^{-2} current density represents a cathode and anode stoichiometry of 2.0 and 4.5 respectively. Table 13 shows the change in the stoichiometry with the changing limiting current density achieved. The figure inset also shows the displacement change with varying compression, it can be seen the displacement change is linear whereas the limiting current is not (also seen inset).

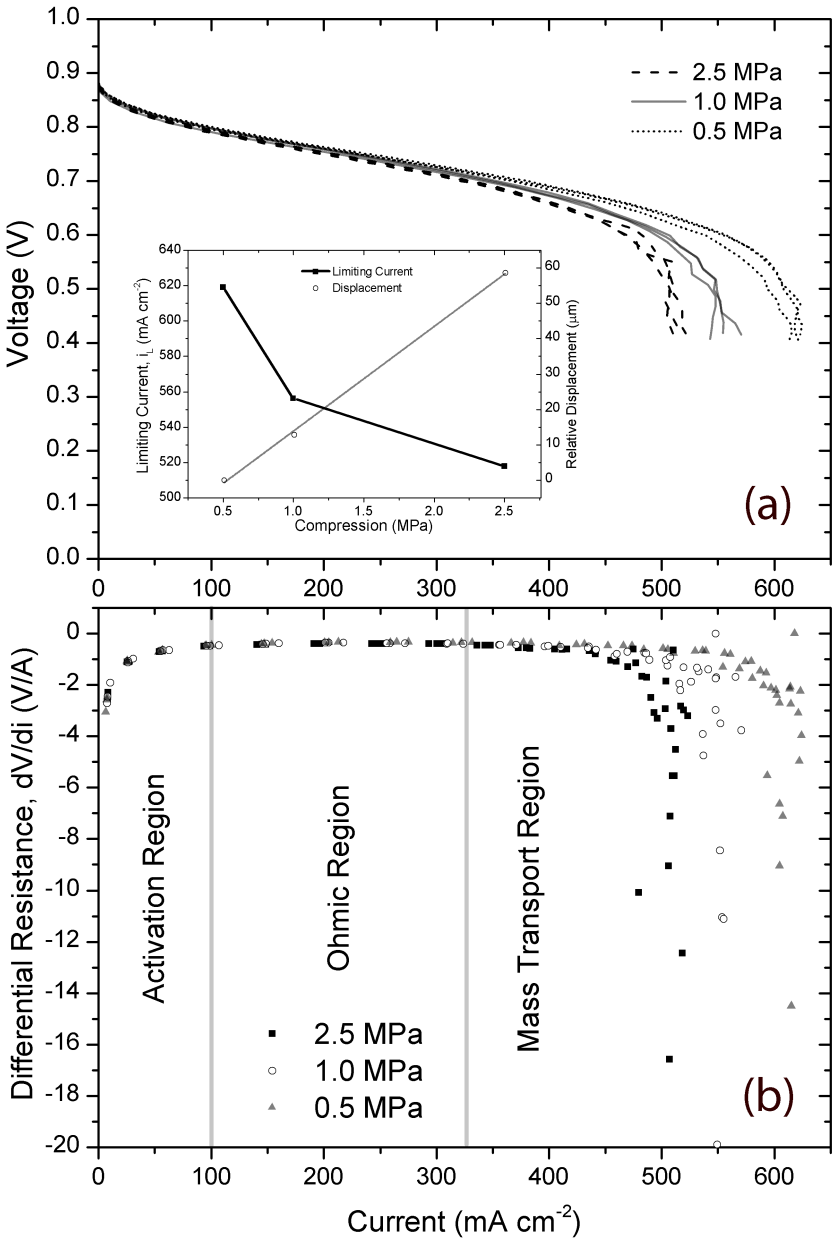

Figure 73: (a) Repeated runs of polarisation curves for various compressions. The fuel cell was operating at 80 °C with constant anode and cathode flow rates of 100 ml min^{-1} at 100% RH. Inset: Limiting current density (i_L) as a function of compression. (b) Representation of the regions of the polarisation curve in the form of differential resistance (from gradient data of part (a)), showing the different loss dominated regions and highlighting the limiting currents under different compressions.

Table 13: Table of limiting current densities observed with associated stoichiometries at various compression values.

Compression (MPa)	Limiting Current Density, i_l (mA cm^{-2})	Anode Stoichiometry	Cathode Stoichiometry
0.5	620	4.5	2.0
1.0	560	5.0	2.2
2.5	520	5.5	2.3

Figure 73 (b) shows a representation of the VI curve data from Figure 73(a) using the gradient of the VI curve between each collected data point, this therefore shows the differential resistance (V/i) at each current density. This data was shown in this way to more clearly differentiate the regions of the VI curve and to highlight that the differences between the three compression values occur in the mass transport region of the graph with relatively higher current density.

Throughout the range of compression there is no affect on the OCV observed, which remained at 876 ± 2 mV. There is however a counterintuitive effect on the ohmic region of the curve, from the previous work done in this thesis (section 3) and increasing compression commonly results in a reduced resistance and hence you would expect an improvement in performance.

Figure 74 shows the average absolute differential resistance between ~100 and ~300 mA cm^{-2} (approximately 0.8 to 0.7 V) for the VI curves at the three compressions with error bars showing the range of data. Over the compression range, an increase in the differential resistance is observed representing an increase in the losses of the system (in approximately the ohmic region). The mechanism for the apparent differential resistance increase is difficult to explain, but it could be due to the mass

transport losses for the area under the lands occurring at the higher voltages at the higher compressions and that effect being greater than the improvement in contact resistance due to increasing compression (See section 6.3).

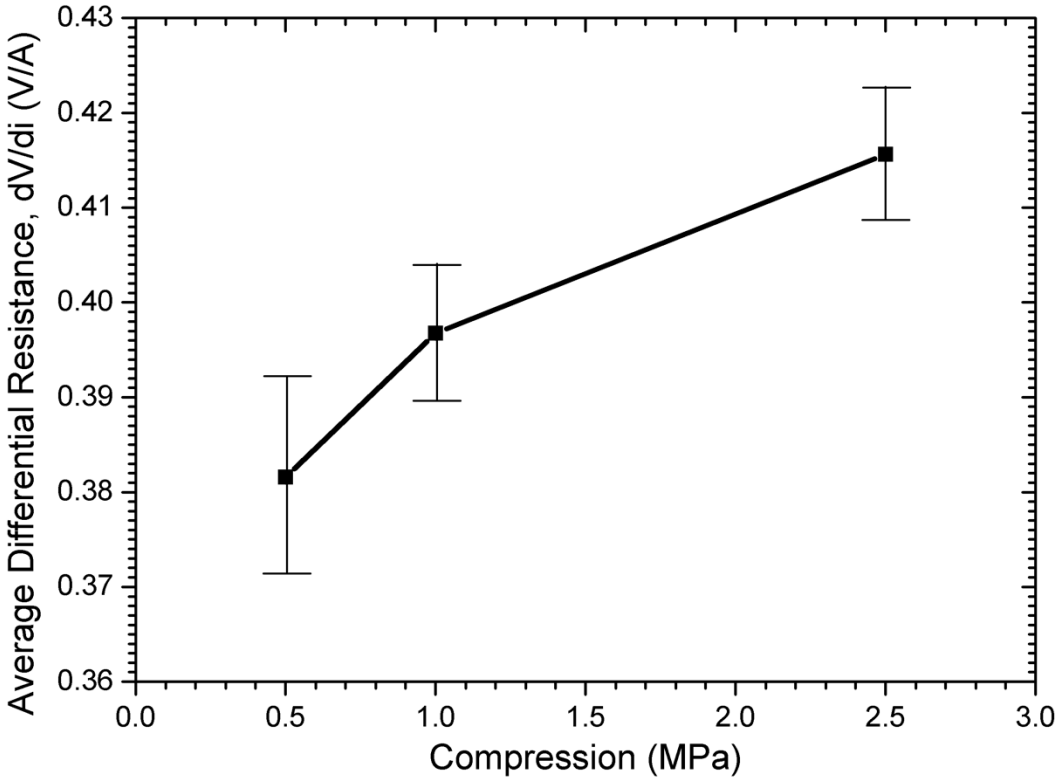

Figure 74: Average differential resistance as a function of fuel cell compression, values calculated over an approximate voltage range of 0.8 to 0.7 V identifying the ohmic region.

6.3. Compression effect on performance

It is clear that compression has a significant effect on the limiting current, as described in previous studies [11, 13, 89, 91, 92]. However, in practical operation, fuel cells are rarely exposed to such extremes of polarisation. In the conventional range of operation, the differences in performance levels are less obvious and the respective contribution from the contact resistance and mass transfer limitation effects are not assessable by simple polarisation analysis. Therefore, EIS was employed to deconvolute the respective loss mechanisms.

A frequency range of 20 kHz to 0.5 Hz was used to capture the range of the processes occurring with different time constants. A voltage of 0.7 V was chosen as representative of practical PEFC operation.

Since the EIS analysis is performed on a complete PEFC, the response is a composite of the anode and cathode. However, due to the much faster electro-kinetics of the hydrogen oxidation reaction HOR (anode), compared to that of the oxygen reduction reaction ORR (cathode), and the higher diffusion coefficient of pure hydrogen compared to the binary diffusion coefficient of 21% oxygen in nitrogen, the composite EIS response is expected to be dominated by the cathode.

Figure 75 compares the response for anode and cathode operation in symmetrical cell mode where the same gas environment is introduced to both sides of the cell; the result is therefore representative of each electrode (anode and cathode) exclusively.

Since no net current is passed in this mode, the arc in the Nyquist plot is confined to the electro-kinetics of each reaction.

It can be seen that the electro-kinetics losses associated with the HOR are very small compared to the ORR and that compression has no significant effect on the electro-kinetics. It can therefore be assumed that the cathode dominates the bulk cell response and that changes in the arc profiles of the EIS response is primarily associated with mass transport processes.

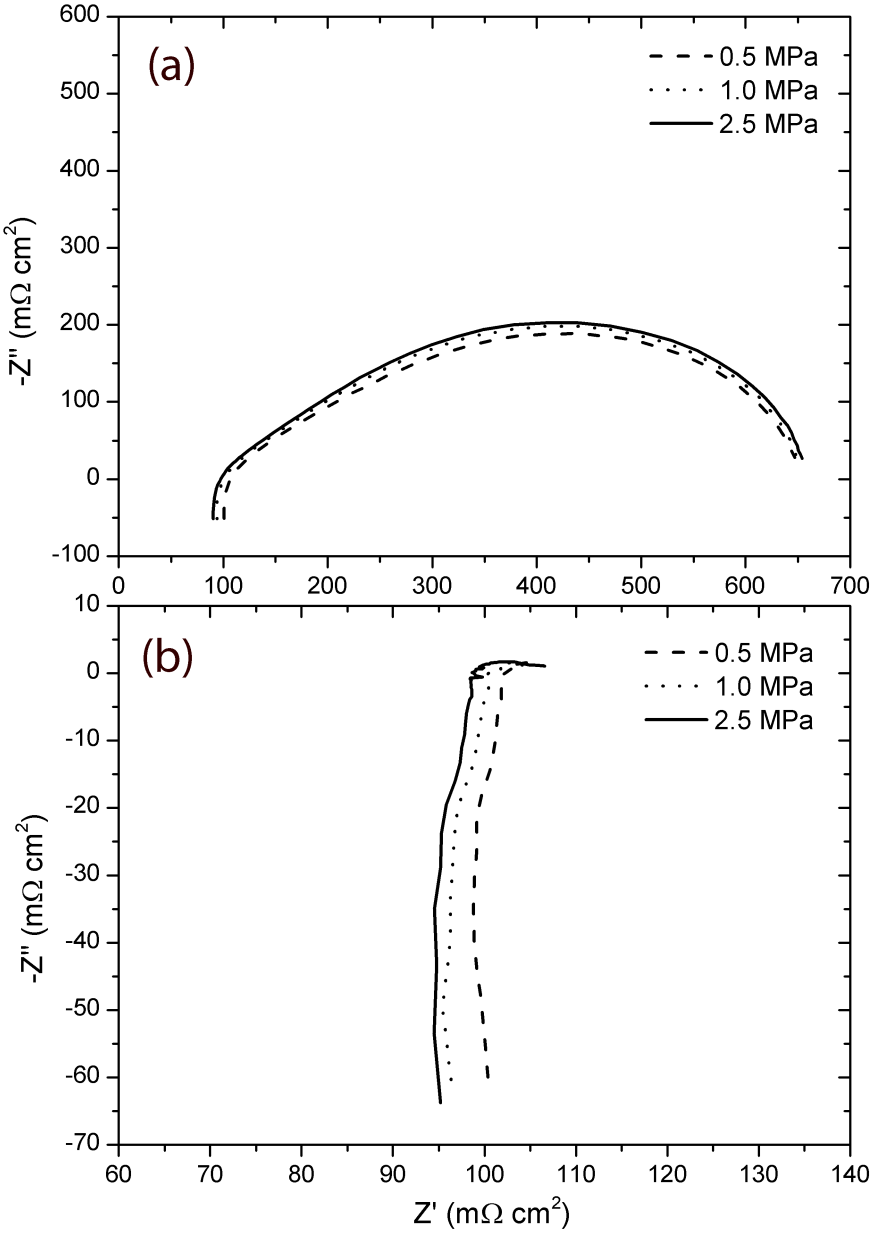

Figure 75: Nyquist plots for symmetrical cells as a function of compression pressure for the cathode (a) and anode (b). The cells were operated at 80 °C with air and hydrogen flow rates of 100 ml min^{-1} and 100% RH for the cathode and anode respectively for all gas streams.

Figure 76 shows the overall EIS response for the cell as a function of compression. With increasing compression, the high frequency intercept with the real axis shifts lower, representing the improved contact resistance from the GDL being crushed into

the flow field plate. The change in contact resistance is attributed exclusively to the change in contact resistance between the FFP and the GDL material, as we assume no change in the ohmic response of the electrolyte. The arc profile is a composite of electro-kinetic and mass transfer losses and can be modelled using the equivalent circuit shown in Figure 77, with a constant phase element (CPE) in place of the ideal capacitor to account for non-ideal electrode surface (i.e. a porous distributed layer of finite thickness rather than a perfectly flat capacitor electrode) and reactant distribution. However, the time constants for the kinetic and mass transport processes are not sufficiently different for the two to be reliably resolved and therefore the total arc width is reported in the knowledge that changes in this feature are exclusively due to mass transport (since all measurements are at the same potential), as shown in Figure 79.

It can be seen that at the same time as the contact resistance reduces with increasing pressure, the impedance arc increases in size showing the increase in the combined charge transfer and mass transport limiting arcs.

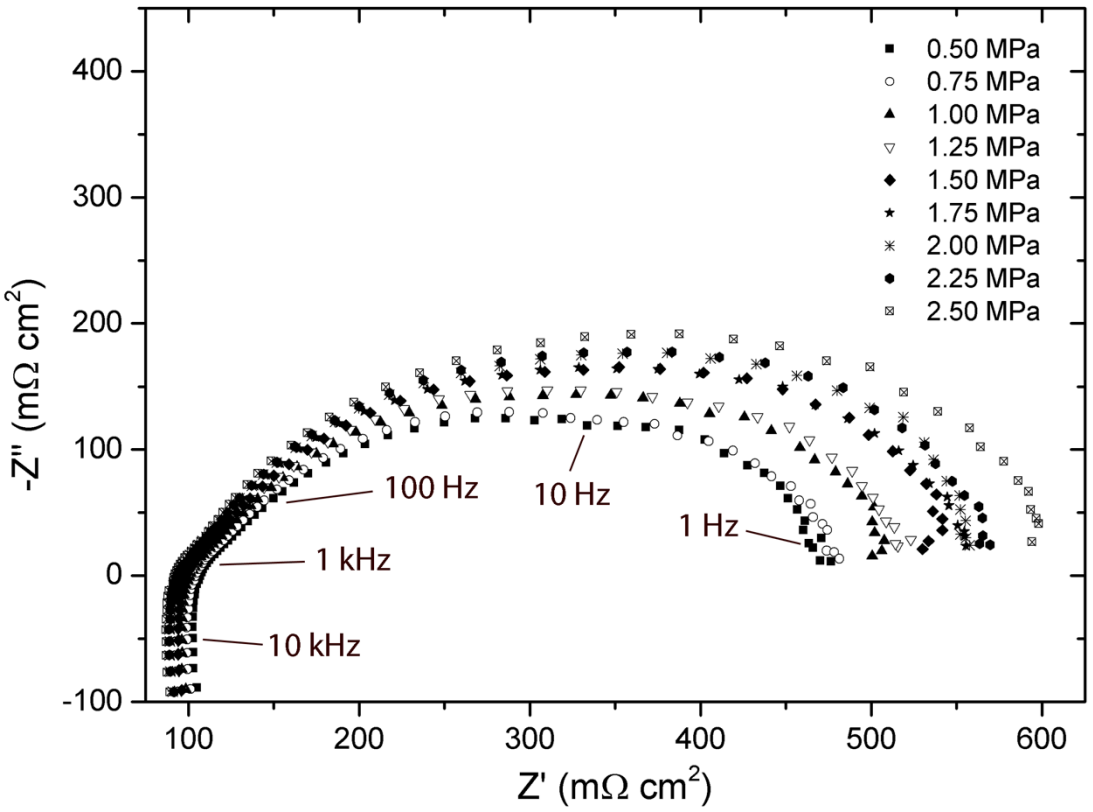

Figure 76: Nyquist plot of fuel cell operating from 0.5 to 2.5 MPa compression at 0.7 V, 80 °C, with constant anode and cathode flow rates of 100 ml min^{-1} at 100% RH. Impedance data taken with an amplitude of 15 mV over a frequency range of 20 kHz to 0.5 Hz.

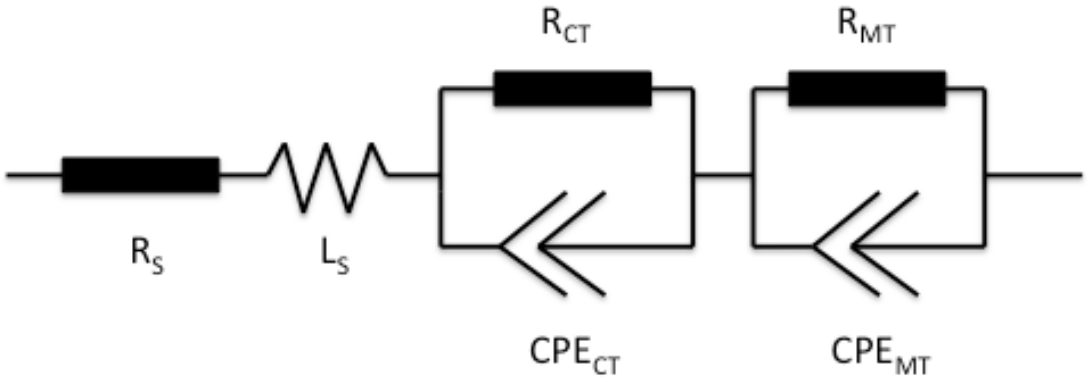

Figure 77: Suggested equivalent circuit for the impedance response exhibited in Figure 76.

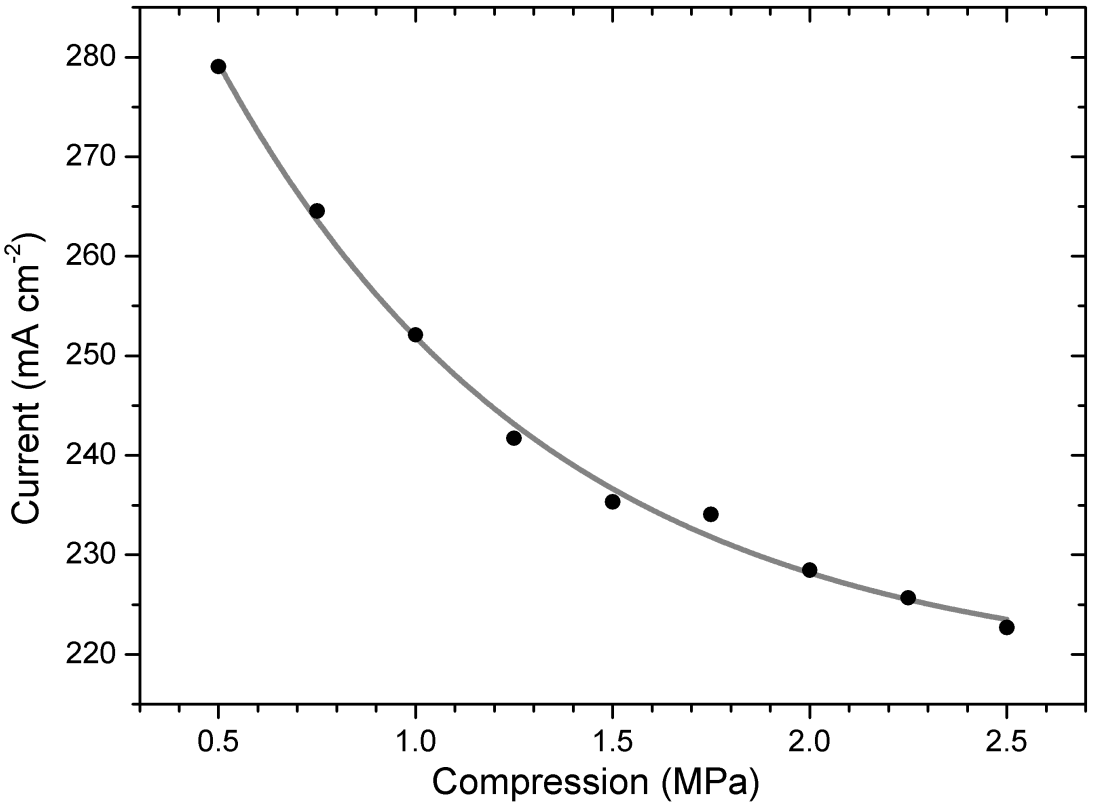

Figure 78: Current response with increasing compression with each set of data corresponding to the impedance data from Figure 76 with a fit as a guide to the eye. Fuel cell operating at 0.7 V, 80 °C, with constant anode and cathode flow rates of 100 ml min^{-1} at 100% RH.

Figure 78 shows the degradation of actual fuel cell current with increasing compression at the operating voltage of 0.7 V. Due to the two zone nature of the active area (under the land and the channel) it is likely that any limitation to the performance caused by the under land compression will have limited affect of the under channel zone. The result of this is a limiting plateau due to the restriction of the active area under the land (but not beneath the channel). The current trend shows that the reduction tends towards a plateau of ~ 220 mA cm^{-2}, a reduction in current density of ~21% over the range. The current density varies from ~280 mA cm^{-2} at 0.5 MPa to ~220 mA cm^{-2} at 2.5 MPa representing a significant decrease in performance.

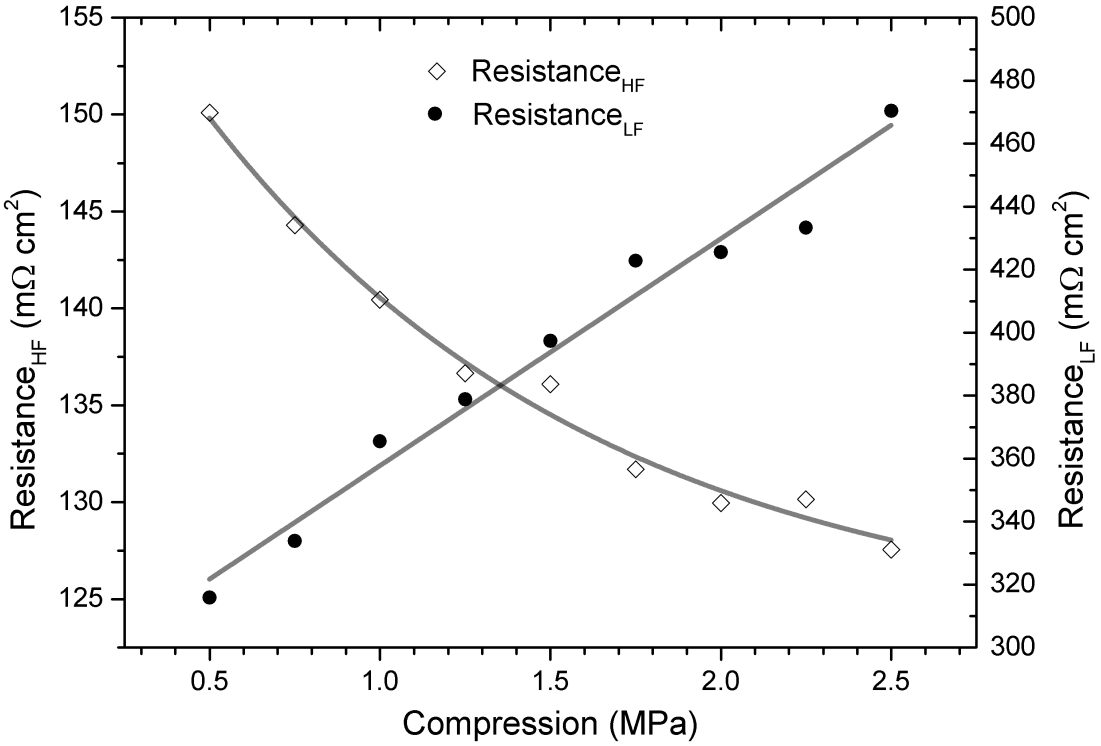

Figure 79: Relationship between the high and low frequency resistance and compression with data taken from Figure 76, with fits as guides to the eye.

Figure 79 represents the competing factors of contact resistance and mass transport resistance as a function of compression. *Resistance$_{HF}$* represents the high frequency intercept with the real axis and *Resistance$_{LF}$* the width of the arc (low frequency intercept minus the high frequency intercept), proxies for contact resistance and mass transport resistance, respectively.

The non-linear change in contact resistance with pressure shows a similar trend to work reported previously from this study [48, 87] and other studies that have looked exclusively at the compression of GDL material between bipolar plates [108]. The high frequency resistance decreases by ~22 mΩ cm^2 over the range, whereas the arc resistance exhibits a much larger (~ 160 mΩ cm^2) linear transition. As shown in

Figure 79, this change can be attributed primarily to mass transport change at the cathode.

Figure 80 shows the high frequency intercept resistance for the symmetrical cell testing shown in Figure 75. A similar non-linear trend is observed as with Figure 79; with close agreement of the ranges of resistances for both anode and cathode systems. The anode resistance varies between 102.2 and 98.8 mΩ cm^2 whereas the cathode response varies between 108.0 and 97.9 mΩ cm^2. The small variation is attributed to changes in the contact interface at the GDL and bipolar plates in between tests. This trend and range agrees well with the *in-situ* GDL work from section 3.

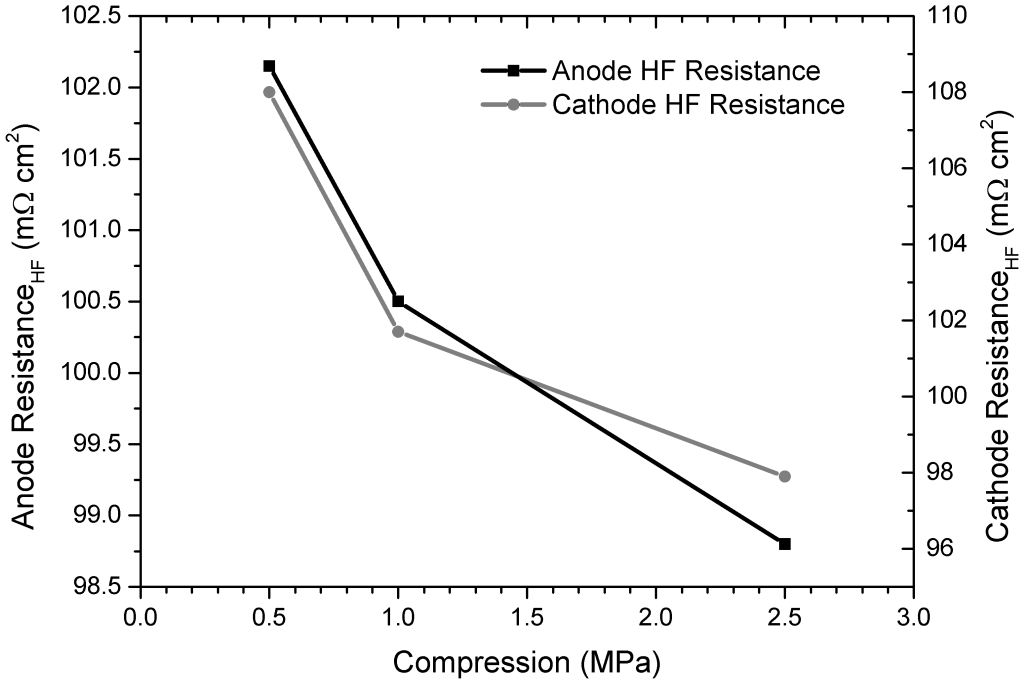

Figure 80: High frequency resistance change with compression for the symmetrical cell testing seen in Figure 75.

The fact that there are two competing factors working in opposition, each with a different sensitivity to compaction force, implies that there is an optimum

compression point that minimises the total resistance. However, because the mass transport resistance is significantly larger than the contact resistance, this is far to the 'left' and effectively equal to 0.5 MPa. This implies that provided the compression is sufficient to ensure adequate sealing and leak free operation, the compression strategy for this cell is to impose the minimum compression to allow maximum performance at the lower voltages.

6.4. Change in porosity and the effect on performance

From the total thickness change observed in the compression range tests of Figure 76 (seen in Figure 71(b)) it is possible to infer a porosity change for the GDL system that is present below the FFP lands. The equation for porosity (see below) equates the volume of the voids within the material (V_{void}) to the total volume (V_{total}) [109]. In this section for porosity calculations the assumption was made of constant solid volume of the sample.

Equation 19

$$\emptyset = \frac{V_{void}}{V_{total}}$$

As the compression increases the porosity under the land is reduced. However, it is difficult to draw conclusions about the nature of GDL porosity across the entirety of the electrode area since two separate regions exist under the land and channel.

From the manufacturer data of the porosity of the GDL material (Toray H060) used in the experimental study, when uncompressed the porosity is 78%, however, from the measurements in this study (section 4) the observed porosity of this material is 63.1% whilst retaining the manufacturer stated initial thickness (190 μm). As such only

values measured during this study will be applied in this section to ensure a more robust result. The reduction in thickness of the MEA observed (~60 μm total) indicates only a ~8% reduction in porosity (to circa 55% porosity) of each GDL beneath the land over the compression range of 0.5 to 2.5 MPa - see Figure 82. The reduction of thickness (by comparison) of 30 in 190 μm represents a ~16% change (total percentage change in value). The disparity between the porosity reduction and thickness change values (8 and 16 respectively) is a result of the relative nature of the values to the initial thickness and porosity of the material.

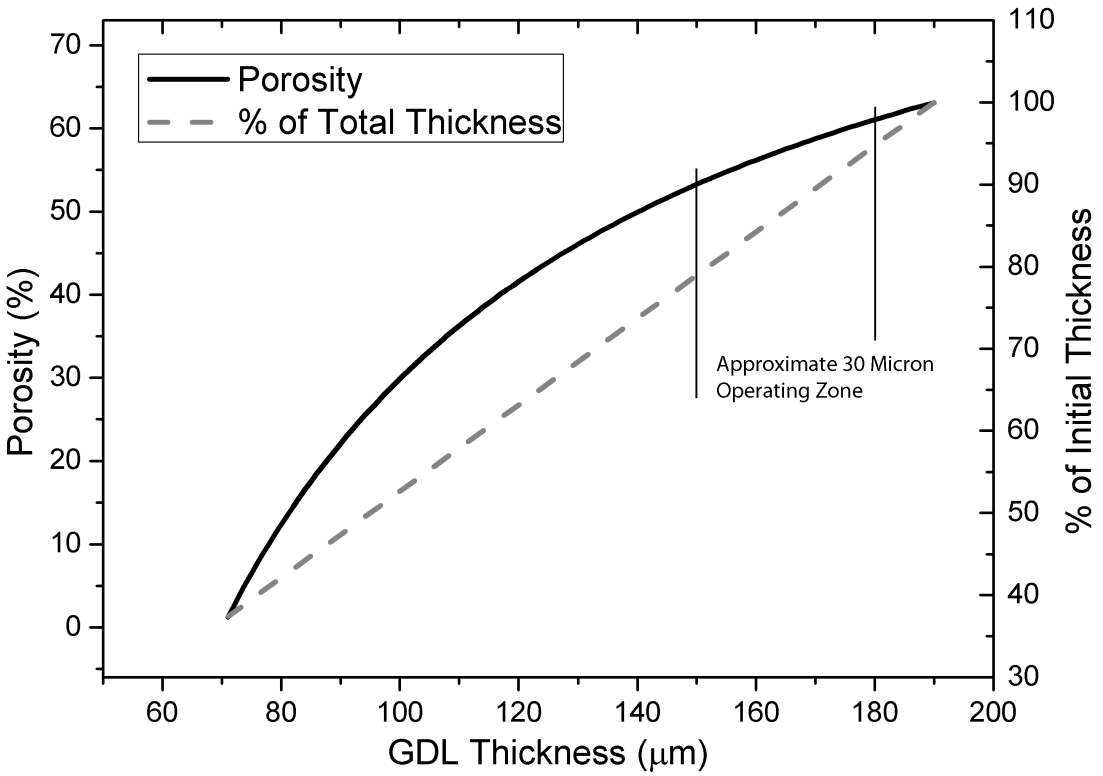

Figure 81: Depiction of the porosity and percentage thickness change with change in GDL thickness showing the non-linear change in porosity. Annotated is the estimated 30 μm operating window of this GDL (Toray H060) over the compression range (0.5 to 2.5 MPa).

The ultimate effect that the under land compression has on performance of the MEA is that the point will be reached where no fuel can reach the catalyst and the only active catalyst will be below the channels, which will be affected less by the change in compression relatively. This will require a significant and unrealistic level of fuel cell compression but the area beneath the land is likely to be inhibited, in terms of water management, with a ~16% reduction in GDL thickness (as observed in Figure 82).

The limiting current density can be calculated by equations such as Equation 14 [102] but is not well defined, when using typical values the current densities are usual higher than is practical. The higher than practical current densities are likely due mainly to the equation not effectively modelling the water management issues. With the GDL system effectively split into two separate regimes (under land and beneath channel) and no direct data available for the under channel system it is difficult to carry out robust analysis using the available data for the system as a whole. It is, however, possible to assume that the effect had on the under channel system is relatively small compared to that under the land and as such analysis can be carried out comparing the 2 zone system to the beneath land zone.

Table 14: Parameters and values used to model the limiting current in Figure 82

Parameter	Value
n	4
F (C mol^{-1})	96486
D (Oxygen in Nitrogen, cm^2 s^{-1})	0.27
y_i	0.2
P (Pa)	101000
R (J mol^{-1} K^{-1})	8.314
T (K)	353

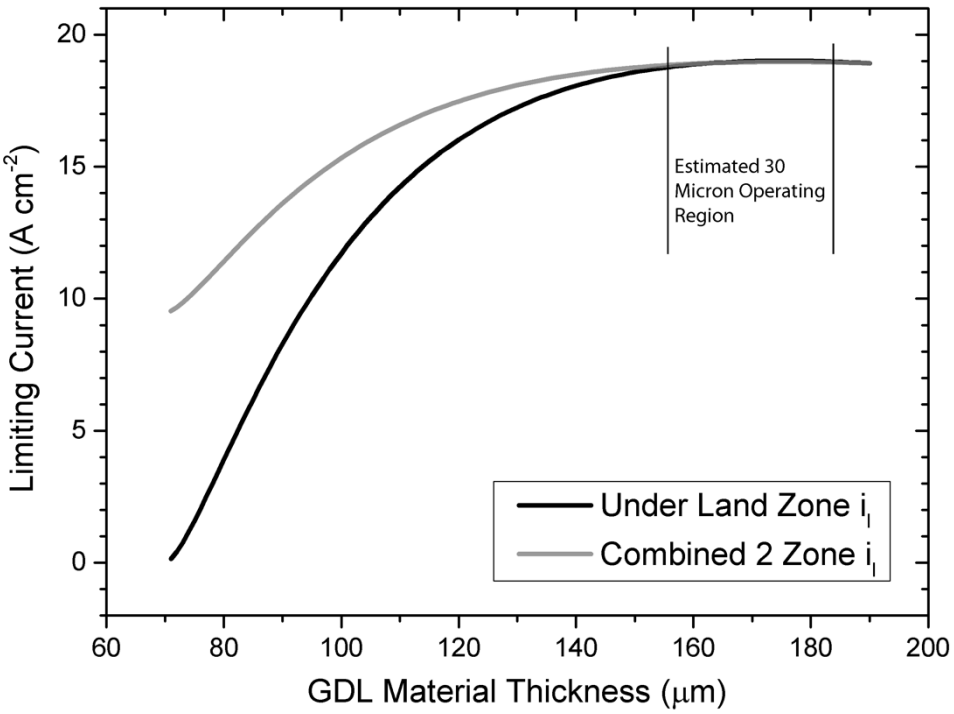

Figure 82: Calculated limiting current density (i_l) using Equation 14 with the parameters from Table 14, using the measured initial porosity of 63.1% and for O_2 in N_2. Two limiting current cases are depicted that of the area under the land and the combination of the land and channel assuming no change in thickness and porosity under the channel. The approximate operating region of the Toray H060 GDL material over the 0.5 to 2.5 MPa compression range is annotated for reference.

Figure 82 shows that calculated limiting current using Equation 14 for the under land zone showing the reduction in limiting current to zero as the porosity of this area is reduced to zero, alongside the combined two zone system assuming that there is no reduction in limiting current for the under channel zone. For the approximate 30 μm operating zone of the GDL material there is expected to be very little change in limiting current from a reactant diffusion perspective. This trend is not what is experienced in practice however, as was shown in Section 6.2. This result highlights

the difference between the theoretical calculation of limiting current and the practical limitations of operating the fuel cell. The potential cause of this is the presence of water in the real system having a large effect on diffusion, particularly at higher current densities. Also the reduction in porosity and thickness will have a greater effect when water is taken into account as its removal may be inhibited by the porosity reduction.

6.5. Effect of varying potential on EIS response

In order to establish an insight into the processes observed in the impedance spectra, impedance scans were carried out over a range of voltages to show the change from charge transfer to mass transfer dominated performance (arc width). The resulting spectra can be seen in Figure 83, the arc in the 0.7 V test increases in size from the 0.75 V test indicating the switch from charge transfer to mass transfer dominance between 0.75 V and 0.7 V (at 1 MPa compression).

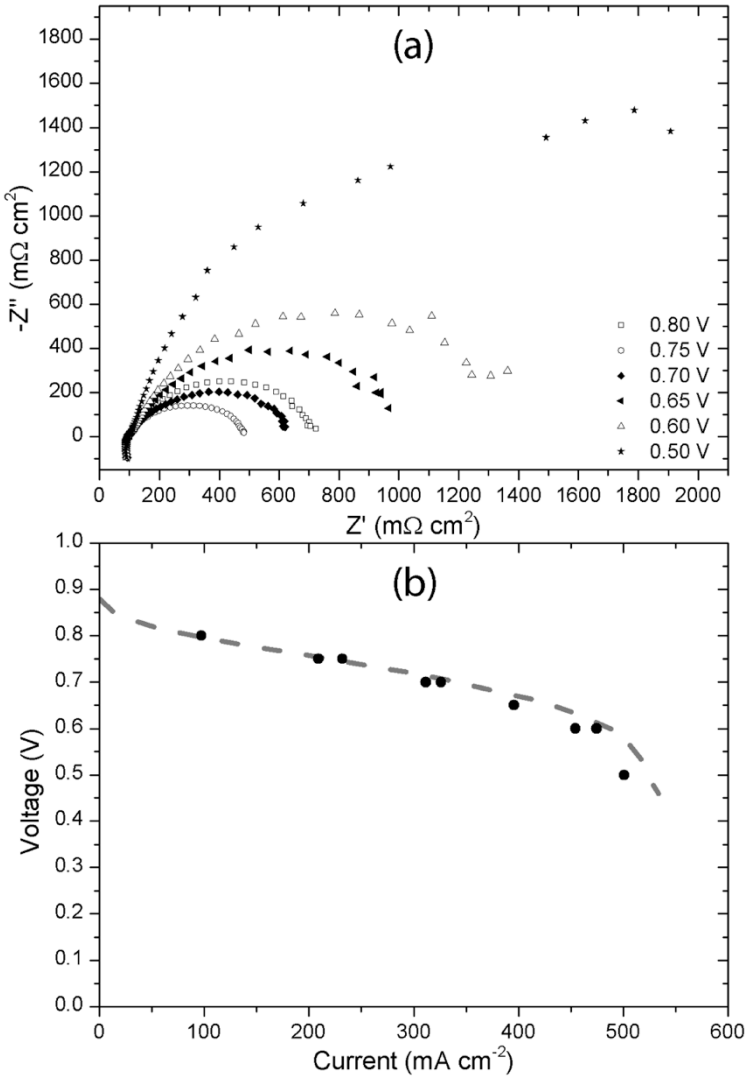

Figure 83: (a) Effect of varying potential at a constant compression of 1 MPa. (b) Current associated with the impedance arcs in (a) with an overlay of a VI curve from Figure 73 showing the correlation between the current stabilisation period prior to impedance measurement with a VI curve under the same conditions. The fuel cell was operating at 80 °C with constant anode and cathode flow rates of 100 ml min^{-1} at 100% RH. Tests carried out at a constant fuel cell compression of 1 MPa.

Prior to each impedance measurement in Figure 83(a), the current was stabilised at each voltage, when plotting these currents and some repeat runs against voltage we

get Figure 83(b). Figure 83(b) shows that despite the impedance response suggesting that mass transport limitations have commenced between 0.75 and 0.7 V the VI curve would suggest that this voltage is still within the ohmic region.

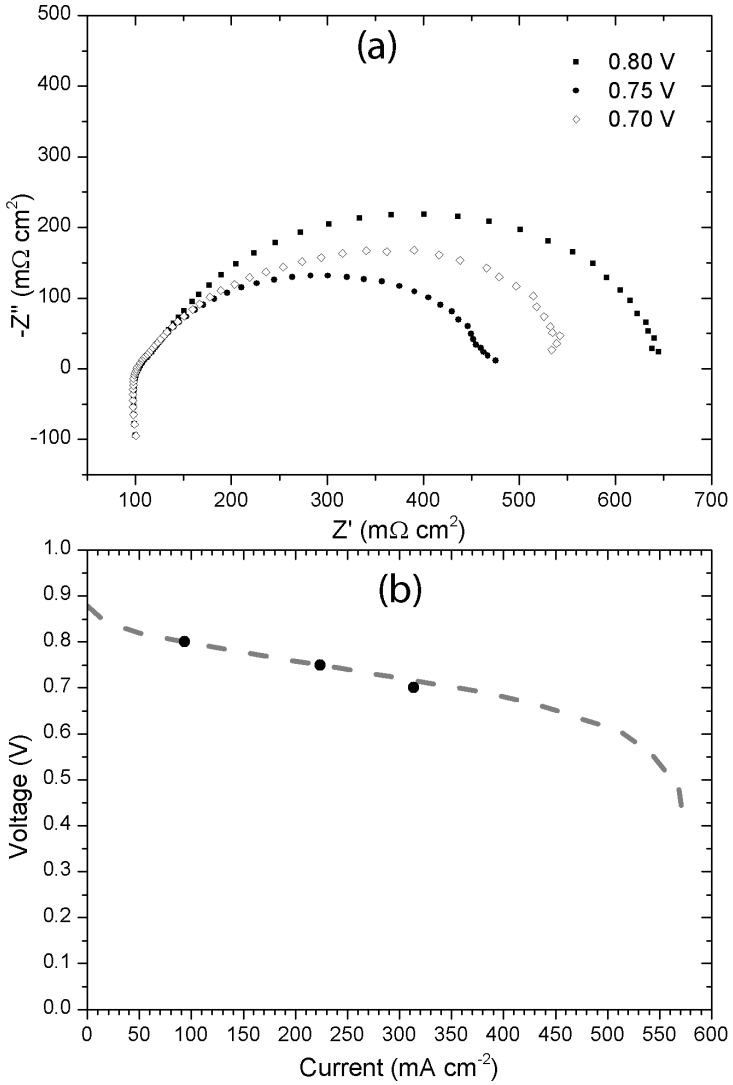

Figure 84: (a) Variation in impedance response at 0.5 MPa. (b) Currents associated with the impedance response of (a) with an overlay of a VI curve from Figure 73 showing the correlation between the current stabilisation period prior to impedance measurement with a VI curve under the same operating conditions. The fuel cell was operating at 80 °C with constant anode and cathode flow rates of 100 ml min^{-1} at 100% RH. Tests at a constant fuel cell compression of 0.5 MPa

Figure 84 (a) shows that the mass transport arc is also presents between 0.75 and 0.7 V at the lower compression of 0.5 MPa. This is despite Figure 84 (b) suggesting, as Figure 83 (b) suggested, that it is operating in the ohmic region.

Using Figure 83 as an example, it is apparent that a certain voltage exists where the low-frequency arc changes from charge transfer to mass transfer. At this point there is a so-called low frequency minimum resistance. From fitting to the low-frequency arcs of Figure 83 the low frequency resistance can be obtained and plotted versus the voltage of the fuel cell the result of which can be seen in Figure 85. It can be clearly noted from the response of the system that the minimum resistance point is visible, representing the point at which the low-frequency arc increases in size. The inset graph from Figure 85 shows a similar data plot but uses the 0.5 MPa data in Figure 84, this response shows the same trend as observed with the higher compression performance test.

The minimum resistance point (MRP) represents the system operating at its smallest total resistance as calculated from the impedance response. The MRP is highly system specific and will likely be significantly altered based on the operating parameters of the fuel cell. As the width of the arc represents both charge and mass transfer losses, factors affecting both these mechanisms will affect the MRP. The stoichiometric ratio is likely to be of particular importance, in theory this is likely to significantly affect the point at which mass transfer limitations occur.

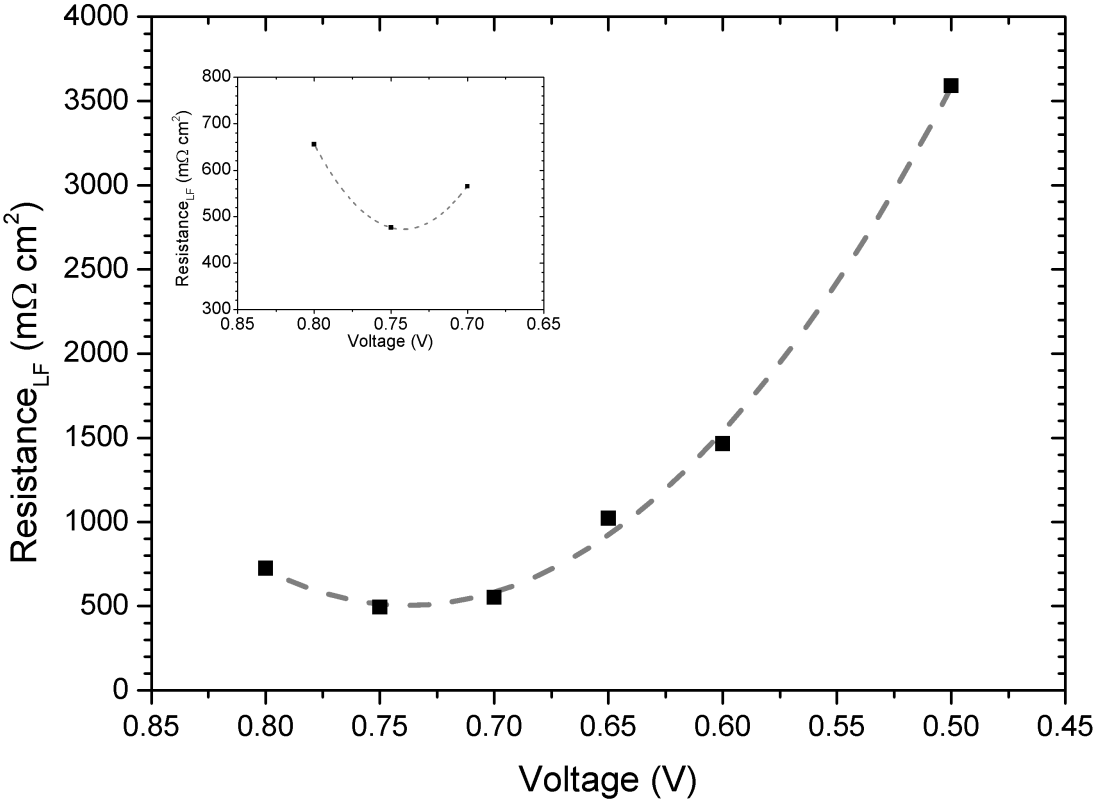

Figure 85: Plot of the low frequency resistance from fitted EIS data against voltage showing the minimum resistance point at 1.0 MPa using the data from Figure 83. The figure inset shows analogous data for a 0.5 MPa compression (Figure 84)

6.6. Conclusions

A significant change in the thickness of the fuel cell is observed with increasing compression, it is shown that this change is due to the GDL material compressing between the lands. Virtually all of the compression of the MEA is associated with the GDL material. An engineering stress strain / curve, suggests a degree of plasticity in the MEA / GDL.

Compression of the fuel cell results in decreased performance. Significant losses in performance occur in the mass transport region of the polarisation curves. Improvement in the high-frequency resistance is observed during the changing compression, this is associated with the reduction in contact resistance between the GDL and bipolar plate material. Simultaneously the low-frequency resistance increases with increasing compression, this is associated with the change in porosity of the GDL materials beneath the lands resulting in larger mass transport losses. The thickness change of the GDL can be used to estimate the change in porosity of the material.

The theoretical effect on performance has been analysed using the limiting current equation to determine the effect of the decrease in thickness and associated change in porosity with compression. When compared to experimental data the region of operation aught not to exhibit a large change in limiting current when using the model and this only serves to highlight the inadequacy of the limiting current equation. In practice it is much more likely to be limited by local water build up in the reduced porosity regions beneath the FFP.

Using low frequency EIS measurements it is clear that an operating point exists were a minimum resistance is observed. It is likely that this feature will be affected by the operating conditions of the cell including the stoichiometric ratio, cell temperature, humidification, compression, etc. As such, this operating point for the cell could represent the ideal operating regime as a trade-off point between power generation and efficiency.

7. Conclusions & Future Work

This study has focused on the effect of compression on MEA components and overall fuel cell performance as well as looking at factors that cause the dimension of MEA components to change with a stress-induced consequence.

A commercially available instrument capable of controlling the compaction pressure while measuring the displacement (with 1 μm resolution) of PEFC MEAs or components in conjunction with a bespoke humidification system and robust testing station was used to perform these studies. Here, the compaction properties of commercial GDL materials in contact with practical BPP flow plate designs is investigated at the same time as the effect on the internal resistance of the GDL and GDL / BPP contact resistance. Derived parameters such as the displacement factor facilitate selection of different GDL materials based on mechanical criteria. Several operating modes of PEFCs have been studied, including start-up and flooding regimes, to observe the effects on the physical and electrochemical characteristics of the fuel cell. The controlled compression operating mode is also used to study the effects on resistance, dimensional change and performance of operating PEFCs.

The work presented in this study has achieved the project goal to add insight into the effect of compression and water management on operating fuel cells and their individual components. A purpose built test rig provided reliable *in-situ* measurements. Starting with a component-level analysis, this provided the ability to deconvolute the MEA response into GDL and membrane specific phenomena.

Despite significant goals being achieved in this project there are a number of areas that remain under studied.

In terms of the *ex-situ* GDL studies presented in this report a key area not currently followed up is the effect that derived GDL parameters have upon current fuel cell modelling equations, this was in part due to the complex nature of the compression in the *in-situ* environment with the impression of the flowfield effectively creating two different zones of compression. As a result of this parameters derived from *ex-situ* measurements are difficult to relate to the *in-situ* environment. As such, building a GDL compression device that can be used with a tomography technique such as X-ray nano-CT (computed tomography) would enable the correct modelling parameters to be obtained (tortuosity and porosity) and thus would enhance modelling accuracy of parameters such as the limiting current, which can be validated using the experimental trends demonstrated in this work.

An area of this report that particularly warrants further investigation is the low frequency minimum resistance work presented in section 6.5. The minimum point of low frequency resistance potentially represents the most efficient operating point (in terms of minimum total resistance) for a fuel cell and as such may provide an answer and technique to where a fuel cell should be operating on its VI curve. To look into this further, a study needs to be conducted where a number of parameters are varied such as reactant stoichiometries, cell temperature and cell compression, then the analysis of low frequency resistance needs to be carried out with a more sensitive change in operating voltage to see the effects on the overall operating parameters.

The in-house developed single cell testing rig has a much improved displacement resolution, down to 0.1 μm, compared to the commercially available CCU used in this project, which has a resolution of 1 μm. In practice this means that a relatively thick membrane has to be used for appreciable changes in thickness to be measureable. Use of the in-house developed rig will enable current commercially available electrolytes to be tested, meaning much more technologically relevant data can be obtained.

The largest section of development from this project is the move towards stack testing from single cells, as presented in the rig designs shown in section 2.6.2. Not only is it important to move from single cells to stacks in terms of the displacement measurement, seeing how operation changes affect the compression and dimensional characteristics of a stack, but also the newly designed rig enables other parameters to be measured including current and compression mapping rather than single compression values. The key difference between the CCU used in this study and the designed rig is the ability to investigate spatial variation of compression alongside dimensional change, which will enable such phenomena as localised flooding (by looking at local pressure changes) and optimisation of operating procedures to minimise changes in compression that may lead to degradation of MEA components.

An area of particular interest is an idea coined as ‘electromechanical impedance’; this technique uses a dynamic mechanical analyser (DMA) to perform mechanical compression oscillation upon mini cells while simultaneously performing EIS. Then by varying the frequency of the compression oscillation the effect this has can be studied electrochemically.

8. Nomenclature

A	Area (cm^2)
BOP	Balance of Plant
BPP	Bi-Polar Plate
$C\infty$	Bulk Concentration (mol m^{-3})
CAD	Computer Aided Design
CCL	Cathode Catalyst Layer
CCU	Cell Compression Unit
CPE	Constant Phase Element
CT	Computer Tomography
D_{eff}	Effective Diffusion Coefficient
DMA	Dynamic Mechanical Analyser
E_0	Maximum Expected Voltage (Nernst Equation, V)
EIS	Electrochemical Impedance Spectroscopy
E_{rev}	Reversible Cell Potential (V)
F	Faraday's Constant (C mol^{-1})
FFP	Flow Field Plate
GDL	Gas Diffusion Layer
H	Enthalpy (J)
HOR	Hydrogen Oxidation Reaction
i	Current Density (A cm^{-2})
i_0	Exchange Current Density
l	Length (m)
M	Mass (kg)
MEA	Membrane Electrode Assembly
MPL	Micro-Porous Layer
n	Number of Moles
OCV	Open Circuit Voltage (V)
ORR	Oxygen Reduction Reaction
P	Total Pressure (Pa)

P&ID (diagram)	Process and Instrumentation Diagram
PEFC	Polymer Electrolyte Fuel Cell
PEMFC	Proton Exchange Membrane Fuel Cell
P_{gas}	Partial Pressure (Pa)
PID (controller)	Proportional Integral Derivative controller
PTFE	Polytetrafluoroethylene
R	Resistance (Ω)
R	Universal Gas Constant (J mol^{-1} K^{-1})
r_{comp}	Component Resistance (Ω)
RH	Relative Humidity (%)
R_{HF}	High Frequency Impedance Resistance (Ω)
R_{LF}	Low Frequency Impedance Resistance (Ω)
S	Entropy (J mol^{-1} K^{-1})
SEM	Scanning Electron Microscopy
T	Temperature (°C)
TPB	Three Phase Boundary
V	Voltage (V)
VI curve	Polarisation curve
V_{solid}	Volume (cm^3)
Z' or Z_{RE}	Real Impedance Component (Ω cm^2)
Z'' or Z_{IM}	Imaginary Impedance Component (Ω cm^2)
α	Charge Transfer Coefficient
δ	Thickness (μm)
η_{act}	Activation Overpotential (V)
η_{conc}	Concentration Overpotential (V)
η_{ohmic}	Ohmic Overpotential (V)
λ	Water Content (mol H_20 / mol SO_3^-)
ρ	Resistivity (Ω m)
ρ	Density (g cm^{-3})
σ	Conductivity (S cm^{-1})
τ	Tortuosity
ϕ	Porosity

9. References

[1] EG&G Technical Services I. Fuel Cell Handbook. 7th ed. USA: U.S Department of Commerce; 2004.

[2] Mauritz KA, Moore RB. State of understanding of Nafion. Chemical Reviews. 2004;104:4535-85.

[3] Berg P, Promislow K, St Pierre J, Stumper J, Wetton B. Water management in PEM fuel cells. J Electrochem Soc. 2004;151:A341-A53.

[4] Mehta V, Cooper JS. Review and analysis of PEM fuel cell design and manufacturing. Journal of Power Sources. 2003;114:32-53.

[5] Litster S, McLean G. PEM fuel cell electrodes. Journal of Power Sources. 2004;130:61-76.

[6] Lim C, Wang CY. Effects of hydrophobic polymer content in GDL on power performance of a PEM fuel cell. Electrochimica Acta. 2004;49:4149-56.

[7] El-kharouf A, Pollet BG. Chapter 4 - Gas Diffusion Media and their Degradation. Polymer Electrolyte Fuel Cell Degradation. Boston: Academic Press; 2012. p. 215-47.

[8] Cindrella L, Kannan AM, Lin JF, Saminathan K, Ho Y, Lin CW, Wertz J. Gas diffusion layer for proton exchange membrane fuel cells--A review. Journal of Power Sources. 2009;194:146-60.

[9] Lee W-k, Ho C-H, Van Zee JW, Murthy M. The effects of compression and gas diffusion layers on the performance of a PEM fuel cell. Journal of Power Sources. 1999;84:45-51.

[10] Wieser C, Helmbold A, Gulzow E. A new technique for two-dimensional current distribution measurements in electrochemical cells. J Appl Electrochem. 2000;30:803-7.

[11] Wang L, Zhang L, Jiang J. Experimental Study of Assembly Clamping Pressure on Performance of PEM Fuel Cells. Applied Mechanics and Materials. 2011;44-47:2399-403.

[12] Malzbender J, Steinbrech RW. Advanced measurement techniques to characterize thermo-mechanical aspects of solid oxide fuel cells. Journal of Power Sources. 2007;173:60-7.

[13] Chang WR, Hwang JJ, Weng FB, Chan SH. Effect of clamping pressure on the performance of a PEM fuel cell. Journal of Power Sources. 2007;166:149-54.
[14] Montanini R, Squadrito G, Giacoppo G. Measurement of the clamping pressure distribution in polymer electrolyte fuel cells using piezoresistive sensor arrays and digital image correlation techniques. Journal of Power Sources. 2011;196:8484-93.
[15] Ihonen J, Jaouen F, Lindbergh G, Sundholm G. A novel polymer electrolyte fuel cell for laboratory investigations and in-situ contact resistance measurements. Electrochim Acta. 2001;46:2899-911.
[16] Slade S, Campbell SA, Ralph TR, Walsh FC. Ionic conductivity of an extruded Nafion 1100 EW series of membranes. J Electrochem Soc. 2002;149:A1556-A64.
[17] Satterfield MB, Majsztrik PW, Ota H, Benziger JB, Bocarsly AB. Mechanical properties of Nafion and titania/Nafion composite membranes for polymer electrolyte membrane fuel cells. Journal of Polymer Science Part B: Polymer Physics. 2006;44:2327-45.
[18] Radhakrishnan V, Haridoss P. Effect of cyclic compression on structure and properties of a Gas Diffusion Layer used in PEM fuel cells. International Journal of Hydrogen Energy. 2010;35:11107-18.
[19] Su ZY, Liu CT, Chang HP, Li CH, Huang KJ, Sui PC. A numerical investigation of the effects of compression force on PEM fuel cell performance. Journal of Power Sources. 2008;183:182-92.
[20] Brett DJL, Kucernak AR, Aguiar P, Atkins SC, Brandon NP, Clague R, Cohen LF, Hinds G, Kalyvas C, Offer GJ, Ladewig B, Maher R, Marquis A, Shearing P, Vasileiadis N, Vesovic V. What Happens Inside a Fuel Cell? Developing an Experimental Functional Map of Fuel Cell Performance. Chemphyschem. 2010;11:2714-31.
[21] Brett DJL, Brandon NP. Review of Materials and Characterization Methods for Polymer Electrolyte Fuel Cell Flow-Field Plates. Journal of Fuel Cell Science and Technology. 2007;4:29-44.
[22] Bazylak A, Sinton D, Liu ZS, Djilali N. Effect of compression on liquid water transport and microstructure of PEMFC gas diffusion layers. Journal of Power Sources. 2007;163:784-92.
[23] Xing XQ, Lum KW, Poh HJ, Wu YL. Optimization of assembly clamping pressure on performance of proton-exchange membrane fuel cells. Journal of Power Sources. 2010;195:62-8.

[24] Makkus RC, Janssen AHH, de Bruijn FA, Mallant RKAM. Use of stainless steel for cost competitive bipolar plates in the SPFC. Journal of Power Sources. 2000;86:274-82.
[25] Davies DP, Adcock PL, Turpin M, Rowen SJ. Bipolar plate materials for solid polymer fuel cells. J Appl Electrochem. 2000;30:101-5.
[26] Li H, Tang Y, Wang Z, Shi Z, Wu S, Song D, Zhang J, Fatih K, Zhang J, Wang H, Liu Z, Abouatallah R, Mazza A. A review of water flooding issues in the proton exchange membrane fuel cell. J Power Sources. 2008;178:103-17.
[27] Yousfi-Steiner N, Mocoteguy P, Candusso D, Hissel D, Hernandez A, Aslanides A. A review on PEM voltage degradation associated with water management: Impacts, influent factors and characterization. J Power Sources. 2008;183:260-74.
[28] Dai W, Wang H, Yuan X-Z, Martin JJ, Yang D, Qiao J, Ma J. A review on water balance in the membrane electrode assembly of proton exchange membrane fuel cells. Int J Hydrogen Energ. 2009;34:9461-78.
[29] Eikerling M, Kornyshev AA, Kucernak AR. Water in Polymer Electrolyte Fuel Cells: Friend or Foe? Phys Today. 2006;59:38-44.
[30] Zawodzinski TA, Davey J, Valerio J, Gottesfeld S. The water content dependence of electro-osmotic drag in proton-conducting polymer electrolytes. Electrochim Acta. 1995;40:297-302.
[31] Zawodzinski TA, Derouin C, Radzinski S, Sherman RJ, Smith VT, Springer TE, Gottesfeld S. Water Uptake by and Transport Through Nafion[R] 117 Membranes. J Electrochem Soc. 1993;140:1041-7.
[32] Springer TE, Zawodzinski TA, Gottesfeld S. Polymer Electrolyte Fuel Cell Model. J Electrochem Soc. 1991;138:2334-42.
[33] Passalacqua E, Squadrito G, Lufrano F, Patti A, Giorgi L. Effects of the Diffusion Layer Characteristics on the Performance of Polymer Electrolyte Fuel Cell Electrodes. J Appl Electrochem. 2001;31:449-54.
[34] Jordan LR, Shukla AK, Behrsing T, Avery NR, Muddle BC, Forsyth M. Effect of diffusion-layer morphology on the performance of polymer electrolyte fuel cells operating at atmospheric pressure. J Appl Electrochem. 2000;30:641-6.
[35] Shimpalee S, Beuscher U, Van Zee JW. Analysis of GDL flooding effects on PEMFC performance. Electrochim Acta. 2007;52:6748-54.
[36] Lim C, Wang CY. Effects of hydrophobic polymer content in GDL on power performance of a PEM fuel cell. Electrochim Acta. 2004;49:4149-56.

[37] Atiyeh HK, Karan K, Peppley B, Phoenix A, Halliop E, Pharoah J. Experimental investigation of the role of a microporous layer on the water transport and performance of a PEM fuel cell. J Power Sources. 2007;170:111-21.
[38] Park S, Lee J-W, Popov BN. Effect of carbon loading in microporous layer on PEM fuel cell performance. J Power Sources. 2006;163:357-63.
[39] Park S, Popov BN. Effect of hydrophobicity and pore geometry in cathode GDL on PEM fuel cell performance. Electrochim Acta. 2009;54:3473-9.
[40] Chu H-S, Yeh C, Chen F. Effects of porosity change of gas diffuser on performance of proton exchange membrane fuel cell. J Power Sources. 2003;123:1-9.
[41] Li X, Sabir I, Park J. A flow channel design procedure for PEM fuel cells with effective water removal. J Power Sources. 2007;163:933-42.
[42] Li X, Sabir I. Review of bipolar plates in PEM fuel cells: Flow-field designs. Int J Hydrogen Energ. 2005;30:359-71.
[43] Stumper J, Lohr M, Hamada S. Diagnostic tools for liquid water in PEM fuel cells. J Power Sources. 2005;143:150-7.
[44] Eikerling M, Kornyshev AA. Electrochemical impedance of the cathode catalyst layer in polymer electrolyte fuel cells. J Electroanal Chem. 1999;475:107-23.
[45] Ge S, Wang C-Y. Liquid Water Formation and Transport in the PEFC Anode. J Electrochem Soc. 2007;154:B998-B1005.
[46] Holmström N, Ihonen J, Lundblad A, Lindbergh G. The Influence of the Gas Diffusion Layer on Water Management in Polymer Electrolyte Fuel Cells. Fuel Cells. 2007;7:306-13.
[47] Spernjak D, Prasad AK, Advani SG. Experimental investigation of liquid water formation and transport in a transparent single-serpentine PEM fuel cell. J Power Sources. 2007;170:334-44.
[48] El-kharouf A, Mason TJ, Brett DJL, Pollet BG. Ex-situ characterisation of gas diffusion layers for proton exchange membrane fuel cells. J Power Sources. 2012;218:393-404.
[49] Le Canut J-M, Abouatallah RM, Harrington DA. Detection of Membrane Drying, Fuel Cell Flooding, and Anode Catalyst Poisoning on PEMFC Stacks by Electrochemical Impedance Spectroscopy. J Electrochem Soc. 2006;153:A857-A64.
[50] Barbir F, Gorgun H, Wang X. Relationship between pressure drop and cell resistance as a diagnostic tool for PEM fuel cells. J Power Sources. 2005;141:96-101.

[51] Brett DJL, Atkins S, Brandon NP, Vasileiadis N, Vesovic V, Kucernak AR. Membrane resistance and current distribution measurements under various operating conditions in a polymer electrolyte fuel cell. J Power Sources. 2007;172:2-13.
[52] Hakenjos A, Muenter H, Wittstadt U, Hebling C. A PEM fuel cell for combined measurement of current and temperature distribution, and flow field flooding. J Power Sources. 2004;131:213-6.
[53] Tuber K, Pocza D, Hebling C. Visualization of water buildup in the cathode of a transparent PEM fuel cell. J Power Sources. 2003;124:403-14.
[54] Zhang FY, Yang XG, Wang CY. Liquid Water Removal from a Polymer Electrolyte Fuel Cell. J Electrochem Soc. 2006;153:A225-A32.
[55] Yang XG, Zhang FY, Lubawy AL, Wang CY. Visualization of Liquid Water Transport in a PEFC. Electrochem Solid St. 2004;7:A408-A11.
[56] Sinha PK, Halleck P, Wang C-Y. Quantification of Liquid Water Saturation in a PEM Fuel Cell Diffusion Medium Using X-ray Microtomography. Electrochem Solid St. 2006;9:A344-A8.
[57] Manke I, Hartnig C, Grunerbel M, Lehnert W, Kardjilov N, Haibel A, Hilger A, Banhart J, Riesemeier H. Investigation of water evolution and transport in fuel cells with high resolution synchrotron x-ray radiography. Appl Phys Lett. 2007;90:174105--3.
[58] Satija R, Jacobson DL, Arif M, Werner SA. In situ neutron imaging technique for evaluation of water management systems in operating PEM fuel cells. J Power Sources. 2004;129:238-45.
[59] Pekula N, Heller K, Chuang PA, Turhan A, Mench MM, Brenizer JS, Ünlü K. Study of water distribution and transport in a polymer electrolyte fuel cell using neutron imaging. Nucl Instrum Meth A. 2005;542:134-41.
[60] Trabold TA, Owejan JP, Jacobson DL, Arif M, Huffman PR. In situ investigation of water transport in an operating PEM fuel cell using neutron radiography: Part 1 ,Äì Experimental method and serpentine flow field results. Int J Heat Mass Tran. 2006;49:4712-20.
[61] Tsushima S, Teranishi K, Hirai S. Magnetic Resonance Imaging of the Water Distribution within a Polymer Electrolyte Membrane in Fuel Cells. Electrochem Solid St. 2004;7:A269-A72.

[62] Feindel KW, LaRocque LPA, Starke D, Bergens SH, Wasylishen RE. In Situ Observations of Water Production and Distribution in an Operating H2/O2 PEM Fuel Cell Assembly Using 1H NMR Microscopy. J Am Chem Soc. 2004;126:11436-7.
[63] Gebel G, Aldebert P, Pineri M. Swelling study of perfluorosulphonated ionomer membranes. Polymer. 1993;34:333-9.
[64] Hinatsu JT, Mizuhata M, Takenaka H. Water-Uptake of Perfluorosulfonic Acid Membranes from Liquid Water and Water-Vapor. J Electrochem Soc. 1994;141:1493-8.
[65] Slade SM, Ralph TR, de Leon CP, Campbell SA, Walsh FC. The Ionic Conductivity of a Nafion (R) 1100 Series of Proton-exchange Membranes Re-cast from Butan-1-ol and Propan-2-ol. Fuel Cells. 2010;10:567-74.
[66] Sone Y, Ekdunge P, Simonsson D. Proton conductivity of Nafion 117 as measured by a four-electrode AC impedance method. J Electrochem Soc. 1996;143:1254-9.
[67] Edmondson CA, Stallworth PE, Wintersgill MC, Fontanella JJ, Dai Y, Greenbaum SG. Electrical conductivity and NMR studies of methanol/water mixtures in Nafion membranes. Electrochim Acta. 1998;43:1295-9.
[68] Rieke PC, Vanderborgh NE. Temperature dependence of water content and proton conductivity in polyperfluorosulfonic acid membranes. Journal of Membrane Science. 1987;32:313-28.
[69] Verbrugge MW, Hill RF. Analysis of Promising Perfluorosulfonic Acid Membranes for Fuel-Cell Electrolytes. J Electrochem Soc. 1990;137:3770-7.
[70] Verbrugge MW, Schneider EW, Conell RS, Hill RF. The Effect of Temperature on the Equilibrium and Transport-Properties of Saturated Poly(Perfluorosulfonic Acid) Membranes. J Electrochem Soc. 1992;139:3421-8.
[71] Zawodzinski TA, Derouin C, Radzinski S, Sherman RJ, Smith VT, Springer TE, Gottesfeld S. Water-Uptake by and Transport through Nafion(R) 117 Membranes. J Electrochem Soc. 1993;140:1041-7.
[72] Zawodzinski TA, Springer TE, Davey J, Jestel R, Lopez C, Valerio J, Gottesfeld S. A Comparative-Study of Water-Uptake by and Transport through Ionomeric Fuel-Cell Membranes. J Electrochem Soc. 1993;140:1981-5.
[73] Zawodzinski TA, Springer TE, Uribe F, Gottesfeld S. Characterization of Polymer Electrolytes for Fuel-Cell Applications. Solid State Ionics. 1993;60:199-211.

[74] Wilson MS, Zawodzinski TA, Gottesfeld S, Kolde JA, Bahar B. Advanced composite polymer electrolyte fuel cell membranes1995.
[75] Halim J, Buchi FN, Haas O, Stamm M, Scherer GG. Characterization of Perfluorosulfonic Acid Membranes by Conductivity Measurements and Small-Angle X-Ray-Scattering. Electrochim Acta. 1994;39:1303-7.
[76] Nouel KM, Fedkiw PS. Nafion (R)-based composite polymer electrolyte membranes. Electrochim Acta. 1998;43:2381-7.
[77] Yoshida N, Ishisaki T, Watakabe A, Yoshitake M. Characterization of Flemion (R) membranes for PEFC. Electrochim Acta. 1998;43:3749-54.
[78] Anantaraman AV, Gardner CL. Studies on ion-exchange membranes .1. Effect of humidity on the conductivity of Nafion(R). J Electroanal Chem. 1996;414:115-20.
[79] Sumner JJ, Creager SE, Ma JJ, DesMarteau DD. Proton conductivity in Nafion (R) 117 and in a novel bis[(perfluoroalkyl)sulfonyl]imide ionomer membrane. J Electrochem Soc. 1998;145:107-10.
[80] Wakizoe M, Velev OA, Srinivasan S. Analysis of Proton-Exchange Membrane Fuel-Cell Performance with Alternate Membranes. Electrochim Acta. 1995;40:335-44.
[81] Buchi FN, Scherer GG. In-situ resistance measurements of Nafion(R) 117 membranes in polymer electrolyte fuel cells. J Electroanal Chem. 1996;404:37-43.
[82] Alberti G, Casciola M, Massinelli L, Bauer B. Polymeric proton conducting membranes for medium temperature fuel cells (110-160 degrees C). Journal of Membrane Science. 2001;185:73-81.
[83] Yang C, Srinivasan S, Bocarsly AB, Tulyani S, Benziger JB. A comparison of physical properties and fuel cell performance of Nafion and zirconium phosphate/Nafion composite membranes. Journal of Membrane Science. 2004;237:145-61.
[84] Xie Z, Song CJ, Andreaus B, Navessin T, Shi ZQ, Zhang JJ, Holdcroft S. Discrepancies in the measurement of ionic conductivity of PEMs using two- and four-probe AC impedance Spectroscopy. J Electrochem Soc. 2006;153:E173-E8.
[85] Eikerling MH, Malek K. Physical Modeling of Materials for PEFCs: A Balancing Act of Water and Complex Morphologies. In: David P. Wilkinson, Jiujun Zhang, Rob Hui, Jeffrey Fergus, Li X, editors. Proton Exchange Membrane Fuel Cells: Materials Properties and Performance: CRC Press; 2010. p. 343-435.

[86] Dohle H, Jung R, Kimiaie N, Mergel J, Müller M. Interaction between the diffusion layer and the flow field of polymer electrolyte fuel cells—experiments and simulation studies. J Power Sources. 2003;124:371-84.
[87] Mason TJ, Millichamp J, Neville TP, El-kharouf A, Pollet BG, Brett DJL. Effect of clamping pressure on ohmic resistance and compression of gas diffusion layers for polymer electrolyte fuel cells. J Power Sources. 2012;219:52-9.
[88] Das PK, Li X, Xie Z, Liu ZS. Effects of catalyst layer structure and wettability on liquid water transport in polymer electrolyte membrane fuel cell. International Journal of Energy Research. 2011;35:1325-39.
[89] Lee W, Ho C, Van Zee JW, Murthy M. The effects of compression and gas diffusion layers on the performance of a PEM fuel cell. J Power Sources. 1999;84:45-51.
[90] Ous T, Arcoumanis C. Effect of compressive force on the performance of a proton exchange membrane fuel cell. J Mech Eng Sci. 2007;221:1067-74.
[91] Ge J, Higier A, Liu H. Effect of gas diffusion layer compression on PEM fuel cell performance. Journal of Power Sources. 2006;159:922-7.
[92] Zhou P, Wu CW, Ma GJ. Influence of clamping force on the performance of PEMFCs. J Power Sources. 2007;163:874-81.
[93] Ismail MS, Hassanpour A, Ingham DB, Ma L, Pourkashanian M. On the Compressibility of Gas Diffusion Layers in Proton Exchange Membrane Fuel Cells. Fuel Cells. 2012;12:391-7.
[94] Yuan X, Sone Y, Wang H, Zhang J. Electrochemical Impedance Spectroscopy in PEM Fuel Cells. London: Springer; 2010.
[95] Bard AJ, Faulkner LR. Techniques based on concepts of impedance. Electrochemical Methods: Fundamentals and Applications. 2 ed: John Wiley & Sons Inc.; 2001. p. 370-3.
[96] Mench MM. Performance Characterization of Fuel Cell Systems. Fuel Cell Engines. New Jersey: John Wley & Sons; 2008. p. 121.
[97] Zamel N, Astrath NGC, Li X, Shen J, Zhou J, Astrath FBG, Wang H, Liu Z-S. Experimental measurements of effective diffusion coefficient of oxygen–nitrogen mixture in PEM fuel cell diffusion media. Chemical Engineering Science. 2010;65:931-7.

[98] Washburn EW. Note on a method of determining the distribution of pore sizes in a porous material. Proceedings of the National Academy of Sciences of the United States of America. 1921;7:115.
[99] Katz A, Thompson A. Prediction of rock electrical conductivity from mercury injection measurements. Journal of Geophysical Research. 1987;92:599-607.
[100] Katz A, Thompson A. Quantitative prediction of permeability in porous rock. Physical review B, Condensed matter. 1986;34:8179-81.
[101] Webb PA. An introduction to the physical characterization of materials by mercury intrusion porosimetry with emphasis on reduction and presentation of experimental data. Micromeritics Instrument Corp, Norcross, Georgia. 2001.
[102] Mench MM. Transport in Fuel Cell Systems. Fuel Cell Engines. New Jersey: John Wiley & Sons; 2008. p. 220.
[103] Fishman Z, Bazylak A. Heterogeneous Through-Plane Distributions of Tortuosity, Effective Diffusivity, and Permeability for PEMFC GDLs. J Electrochem Soc. 2011;158:B247-B52.
[104] Peron J, Mani A, Zhao X, Edwards D, Adachi M, Soboleva T, Shi Z, Xie Z, Navessin T, Holdcroft S. Properties of Nafion® NR-211 membranes for PEMFCs. Journal of Membrane Science. 2010;356:44-51.
[105] Brett DJ, Atkins S, Brandon NP, Vesovic V, Vasileiadis N, Kucernak A. Localized impedance measurements along a single channel of a solid polymer fuel cell. Electrochemical and solid-state letters. 2003;6:A63-A6.
[106] Meriam JL, Kraige LG. Vibration and time response. Engineering Mechanics: Dynamics. 6 ed: John Wiley & Sons; 2008. p. 601-8.
[107] Mason TJ, Millichamp J, Neville TP, Simons SR, Shearing P, Brett DJL. A Study of the Effect of Water Management and Electrode Flooding on the Dimensional Change of Polymer Electrolyte Fuel Cells. J Power Sources. 2012 (Submitted).
[108] Nitta I, Hottinen T, Himanen O, Mikkola M. Inhomogeneous compression of PEMFC gas diffusion layer: Part I. Experimental. J Power Sources. 2007;171:26-36.
[109] Mench MM. Transport in Fuel Cell Systems. Fuel Cell Engines. New Jersey: John Wiley & Sons; 2008. p. 245.

10. Appendix A

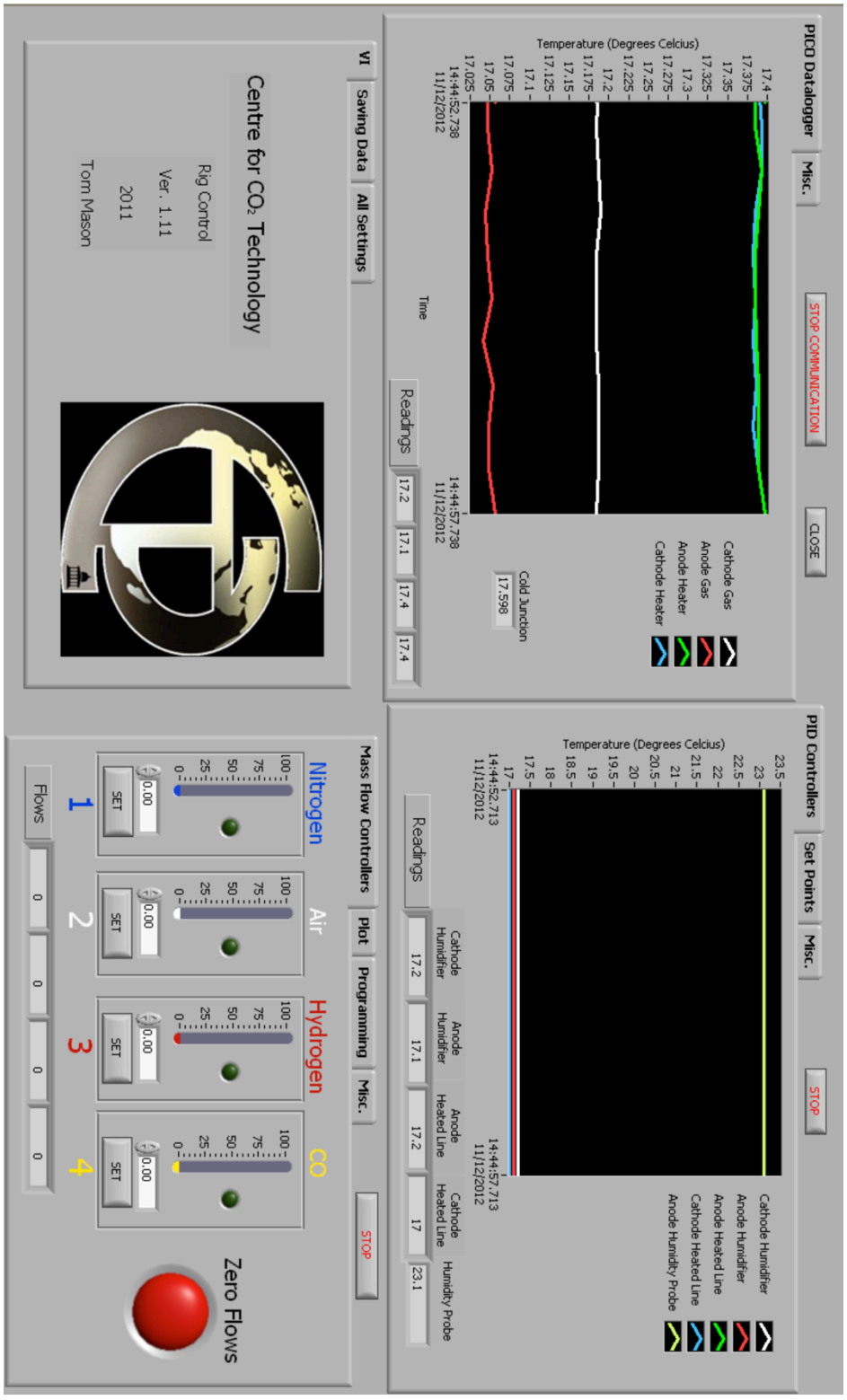

Figure 86: Developed LabVIEW VI for control of the testing rig.

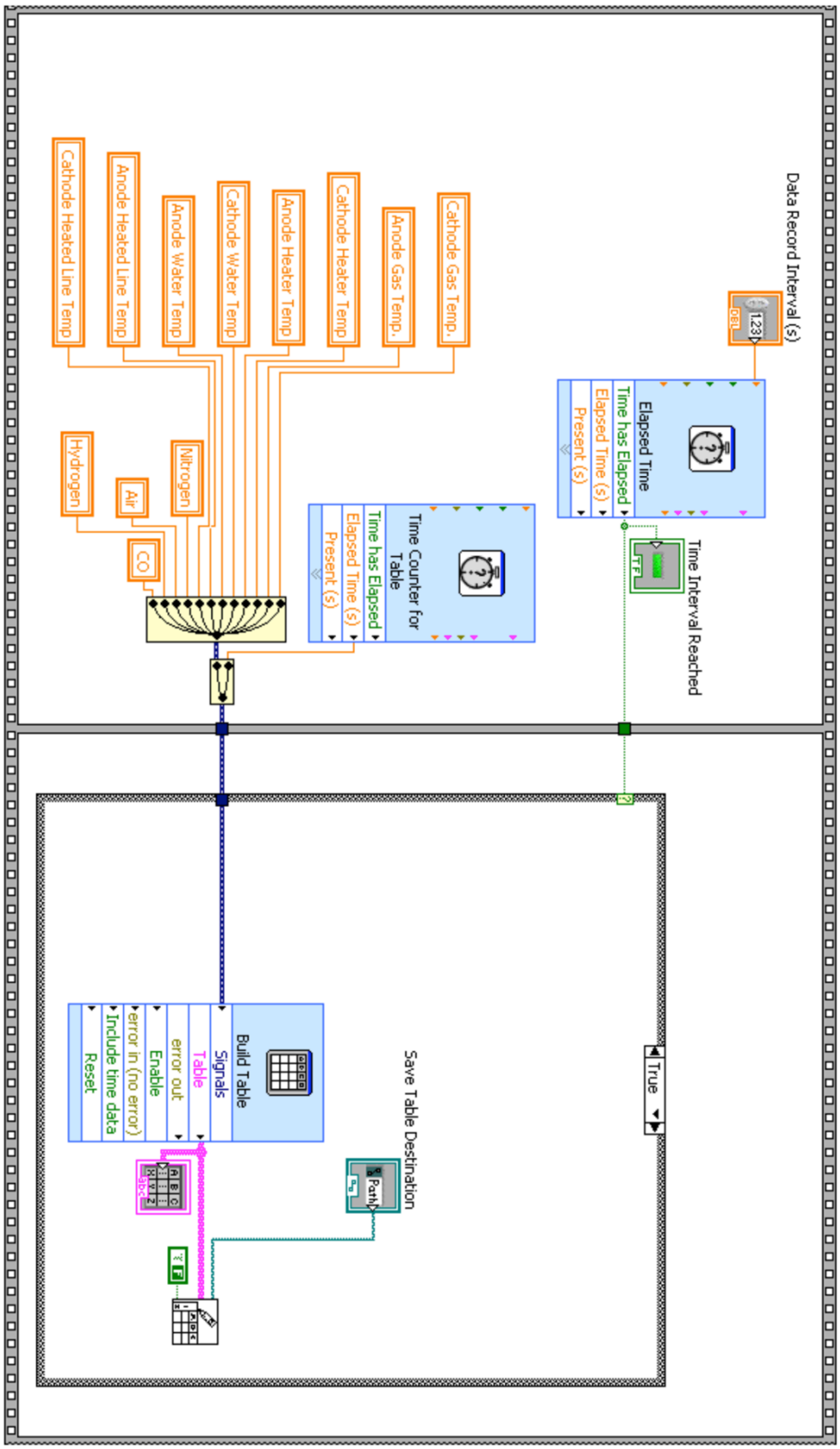

Figure 87: Section of the LabVIEW block diagram showing the collection and saving of data

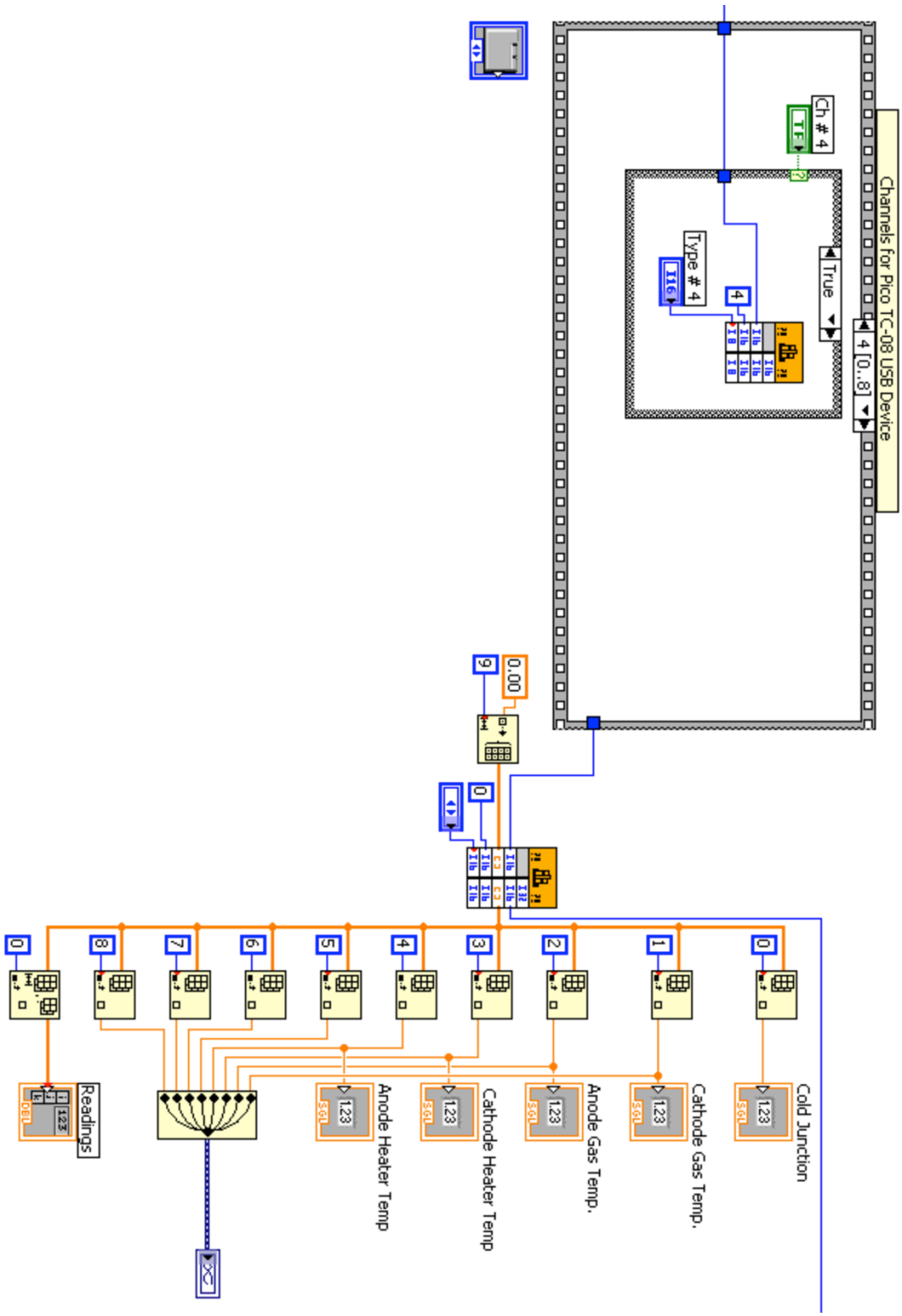

Figure 88: LabVIEW block diagram section showing collection of temperature measurements and display on the front panel.

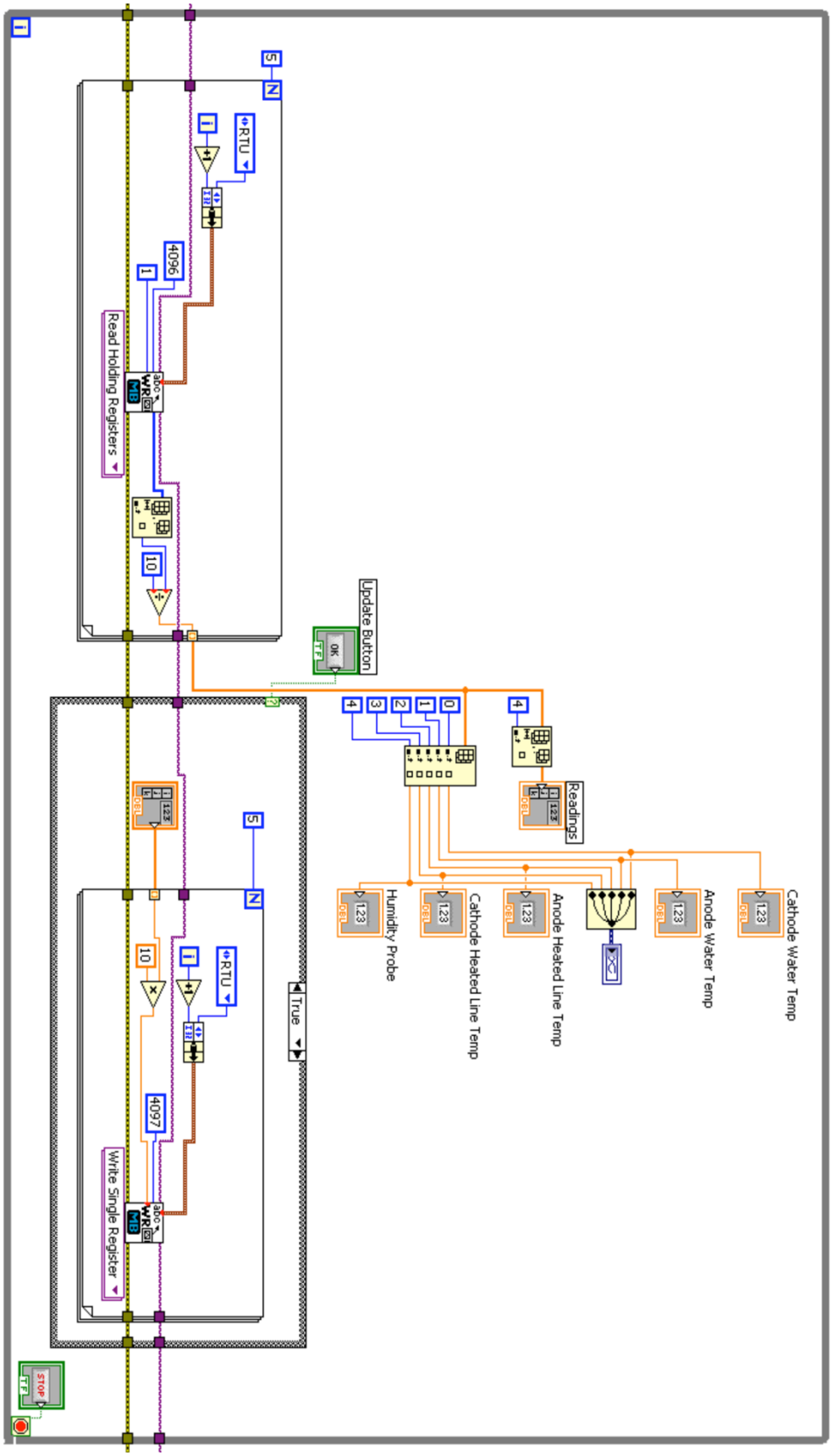

Figure 89: Block diagram section of the LabVIEW VI showing the control and display of data from the PID controllers